ADVANCING PARTIALLY-AVERAGED NAVIER-STOKES METHOD IN WALL-BOUNDED AND SPATIALLY-EVOLVING TURBULENCE

A Dissertation

by

PEDRAM TAZRAEI

Submitted to the Office of Graduate and Professional Studies of
Texas A&M University
in partial fulfillment of the requirements for the degree of

DOCTOR OF PHILOSOPHY

Chair of Committee,	Sharath S. Girimaji
Co-Chair of Committee,	Luis San Andres
Committee Members,	Nagamangala Anand
	Prabir Daripa
	Diego Donzis
Head of Department,	Andreas A. Polycarpou

May 2020

Major Subject: Mechanical Engineering

ABSTRACT

Scale-resolving simulations (SRS) of turbulence offer a computationally viable alternative to direct numerical simulations (DNS) and large eddy simulations (LES) for many flows of engineering interest. SRS seeks to achieve significant computational cost reduction over LES (large eddy simulations) by selective resolution of key coherent structures and modeling the remainder of the flow field using higher fidelity closures. SRS aims to provide significant improvements over Reynolds-averaged Navier-Stokes (RANS) method with only a reasonable increase in computational effort. The objective of this thesis is to advance bridging scale-resolving simulations to a state-of-the-art computational tool for the analysis, comprehension and prediction of turbulent flows of engineering interest. Toward this end, this thesis addresses key challenges facing SRS in near-wall subgrid closures, spatially-evolving flows and transition to turbulence. Scale-resolving simulations can be broadly classified into zonal (Z-SRS) and bridging (B-SRS) approaches. In Z-SRS different subgrid closure methods (e.g., RANS and LES) are used in different parts of the computational domain. One the other hand, B-SRS uses the same closure approach over the entire computational domain. The physical resolution (cut-off scale) of the subgrid model is controlled by changing the closure coefficients in a manner that is consistent with turbulence physics. The partially-averaged Navier-Stokes (PANS) method is a B-SRS approach that employs RANS-type two-equation (or better) closures that are suitably adapted to represent the required degree of spectral resolution. Three studies are undertaken in the thesis to advance PANS in wall-bounded flows with spatially-evolving turbulence and laminar-to-turbulence transition. Although all of the development is in the context of PANS, the findings of the thesis are generally applicable to other SRS methods. In the first study, equilibrium boundary layer (EBL) analysis is performed on the filtered turbulence to drive key closure models for scale resolving simulations (SRS) of turbulence. The objective is to convey the advantages of RANS near-wall closure modeling to SRS methodology. In the context of two-equation SRS turbulence closure, the EBL analysis of filtered-flow

fields leads to closure models for turbulent transport of unresolved kinetic energy and dissipation as a function of degree of resolution. The resulting model is then employed to perform SRS-PANS computations of a fully developed turbulent channel flow. It is demonstrated that PANS computations yield flow-field statistics that are consistent with filtered-field closure modeling assumptions. (This work has appeared in (1)). The second study aims to enhance the applicability and accuracy of SRS-PANS in fully-developed wall-bounded spatially-evolving turbulent flows. Scale resolving simulations of turbulence that employ two-equation subgrid closures require physically consistent boundary conditions for unresolved kinetic energy and dissipation (or frequency). Hence, the second work aims to develop accurate inflow turbulent boundary layer description by (i) adapting recycling/rescaling technique and (ii) extending equilibrium boundary layer scaling to partially resolved inflow fields. The proposed scheme is employed to compute a spatially-evolving zero pressure gradient flat plate boundary layer (ZPGFPBL) over a continuous range of Reynolds numbers based on the momentum thickness ($650 \leq Re_\theta \leq 1434$). The SRS results are then evaluated in the following categories: wall coefficients; mean-flow profiles; second-moment profiles; high-order statistics; and multi-point correlations. The third study is a preliminary investigation of adapting SRS in general, and PANS in particular, for simulating the laminar-turbulent natural K-type transition. The goal is to simulate key aspects of transition behavior in boundary layers at an affordable computational cost, which is significantly lower than that of LES. The development ensures that the appropriate physics, Tollmien-Schlichting (TS) waves and transport of momentum through the ejection and sweep mechanisms, are reasonably simulated in the near-wall region. The departure of the skin friction coefficient from the laminar curve, along with its overshoot in the post-transition regime are well-captured. The development of statistics into the fully-developed equilibrium state are confirmed.

DEDICATION

I am dedicating this work to my mother, my father, and my sisters who have always motivated me to pursue my ambitious goals.

ACKNOWLEDGMENTS

I would like to wholeheartedly thank Professor Sharath Girimaji for endless support, continuous patience and encouragement while guiding me through the course of my research. Thank you for being a true mentor for me.

Special thanks to my PhD committee members, Professor Luis San Andres, Professor Nagamangala Anand, Professor Prabir Daripa, and Professor Diego Donzis, whose constructive feedback certainly enhanced this dissertation. I would also like to thank Dr. Pooyan Razi for introducing me to OpenFOAM. My appreciation goes to Dr. Sasan Salkhordeh and Dr. Ardalan Javadi for their assistance. I am also grateful to my colleagues and friends at Texas A&M University: Mona, Divya, Ankita, Vishnu, Filipe, Steven, Massey, Salar, Bajrang, Rishita and Chetna.

My deepest gratitude goes to my parents, Fariba and Mohammad, and my sisters, Paniz and Parisa, whose support and encouragement have always driven me to my goals. I am also thankful of everyone who has encouraged me on my PhD journey.

Lastly, I want to thank the Texas A&M High Performance Research Computing center and the Texas Advanced Computing Center (TACC) at the University of Texas at Austin for their supports.

CONTRIBUTORS AND FUNDING SOURCES

Contributors

This work was supported by a dissertation committee consisting of Professor Sharath Girimaji [advisor], Professor Nagamangala Anand and Professor Luis San Andres of the Department of Mechanical Engineering, Professor Diego Donzis of the Department of Aerospace Engineering, and Professor Prabir Daripa of the Department of Mathematics at Texas A&M University.

All the work conducted for the dissertation was completed by the student independently.

Funding Sources

Graduate study was supported by the Research assistantship in the Turbulence Research Laboratory of Professor Sharath Girimaji and Teaching assistantship from the Department of Mechanical Engineering at Texas A&M University.

TABLE OF CONTENTS

Page

LIST OF FIGURES

FIGURE Page

LIST OF TABLES

TABLE Page

1. INTRODUCTION

Turbulence is found almost everywhere in our daily life. It is inherently complex and profoundly affects a broad range of engineering applications. Design and optimization of facilities in different sectors, e.g., weather and climate, power and energy, and global ocean circulation, rely on the accurate prediction of transitional and turbulent flow features. Depending on the type of application, its presence can be either beneficial or detrimental. Turbulence, for example, helps air and fuel mix more efficiently in combustion chambers. It energizes the boundary layer over moving bodies and boost tsubhe resistance against the separation. On the other hand, compared to laminar flow fields, turbulence increases the friction drag acting on the streamlined bodies.

One of the key features that renders computation and comprehension of turbulence complex is the wide range of scales of motion- length and time scales. Non-linearity, non-locality and chaotic character of turbulence make it one of the most challenging problems not only in fluid dynamics, but also in the whole classical physics.

There are three approaches established for analyzing turbulent flows: (i) Reynolds averaged Navier-Stokes (RANS) (11), (ii) large eddy simulation (LES) (12), and (iii) direct numerical simulation (DNS) (13). As shown in Figure 1.1, RANS and DNS represent the two extremes of a typical turbulent energy spectrum. In RANS, only the mean flow field is resolved, and all the turbulent motion is modeled. This justifies the affordability of RANS simulations for engineering problems. However, resolving no unsteadiness in the flow field can affect the level of accuracy. DNS, on the other hand, resolves all the temporal and spatial scales of turbulence for a specific level of accuracy. Clearly, the high accuracy of DNS solution comes with an excessive computational cost. For the sake of computational saving, LES explicitly resolves large energy containing turbulent eddies and model the subgrid scales. In LES, the effects of small subgrid scales on the resolved scale is modeled using subgrid closures. The reason for modeling only small scales emanates from the fact that they contain low energy level and show somehow universal dynamics. Besides, they require a very fine resolution to be resolved.

RANS is computationally straightforward, but its accuracy is not adequate for many industrial applications. DNS and LES, on the other hand, provide accurate solutions but are only computationally feasible for a small subset of canonical flows.

1.1 Scale-resolving simulations

For industrial applications, the need for fast turn-around while maintaining maximum accuracy motivates the need for innovative and robust scale-resolving turbulence models. In recent years, scale-resolving simulations (SRS) have attracted much attention. SRS is an accuracy-on-demand type of turbulence computations. In order to achieve adequate results at a reasonable computational cost, SRS selectively resolves high energy containing turbulence structures and models the remainder time and length scales. In SRS, the physical completeness of Navier-Stokes equations is merged with the computational affordability of turbulence modeling. Hence, the goal of SRS is to judicially resolve the key coherent, non-universal features of the given flow and to model residual 'canonical' turbulence fields with a reasonable closure to achieve optimal cost-accuracy balance. Exclusive dependence on the closure model in coherent structure region can lead to large errors, and excessive resolution in regions of background turbulence will increase computational cost without commensurate increase in accuracy. High fidelity closures can decrease the need for resolution and yield more accurate predictions at lower levels of resolution.

SRS techniques can be classified into zonal and bridging methods. Zonal-SRS (Z-SRS) approaches (14; 15; 16) combine RANS and LES in different parts of the computational domain. Bridging SRS (B-SRS) (17; 18; 19; 20), on the other hand, employs the same closure model – with scale-dependent coefficients – throughout the entire domain. The focus of this thesis is partially averaged Navier-Stokes (PANS), which is a bridging SRS (B-SRS) approach.

PANS seeks to achieve computational advantage over conventional LES by employing higher-order closure which, in turn, allows resolving narrower range of coherent large scales (Figure 1.1). PANS adapts two-equation RANS or Second Moment Closure (SMC) models to account for the subfilter scales residing in the flow field. Hence, the modifications made over the years for the RANS two-equation closures can be transferred to the PANS subfilter modeling. In PANS, the

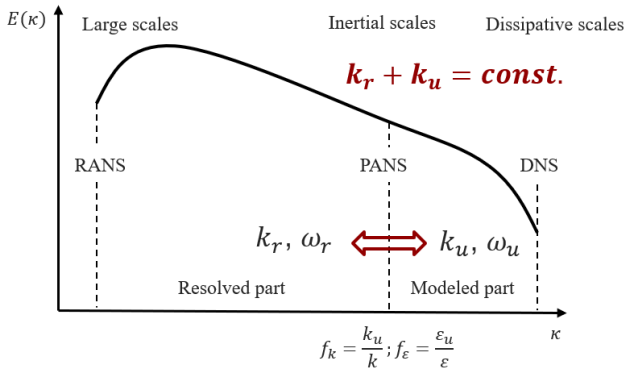

Figure 1.1: A typical PANS energy spectrum.

subfilter length and velocity scales are obtained from the two-equation closure. The various PANS features and the corresponding physical/mathematical principles are discussed below.

- In PANS, the partition between resolved and unresolved scales of motion is characterized in terms of the fractions of unresolved kinetic energy and (specific) dissipation (Figure 1.1). PANS solves evolution equations for subgrid kinetic energy and dissipation (or frequency) to obtain length and velocity scales of the subfilter field. Hence, the fidelity of subfilter modeling is associated with a complete description of the unresolved field. While this completeness is missed in most other SRS approaches, leading to important deficiencies.

- All of the closure modeling theories (e.g., rapid distortion theory, representation theory), physical classification (e.g., pressure-strain correlation physics) and mathematical constraints (e.g., realizability) developed over the decades for RANS and Reynolds stress closure model (RSCM) principles can be carried over to PANS (21; 22).

- Spectral scaling laws can be invoked to specify closure model coefficients as a function of degree of scale resolution or cut-off length scale (18).

- The PANS unsteady flow features and multi-point statistics have been demonstrated to be consistent with Kolmogorov scaling laws (23).

- RANS to LES transition in the boundary layer is accomplished by scaling down equilibrium boundary layer analysis to cut-off scale energy dynamics. PANS inherently does not have a log-layer mismatch (24).

So far, the PANS model has been used to compute many canonical, benchmark and complex aerodynamic flows with good success. This approach has already been well-documented for the turbulent channel flow (1), flows over periodic hills (25), flows past square and circular cylinders (26; 27), smooth flow separation (28; 29; 24), flow past bluff bodies (30), flow around a landing gear configuration (31; 32), flow around a bulk carrier (33), and flow past a vehicle model (34; 35; 36). Although PANS has been founded on a solid background, it still faces some challenges.

1.2 Challenges

The near-wall modeling of turbulent flow fields is one of the main challenges involved in the scale-resolving simulations. PANS offers the mathematical framework and analytical techniques to rigorously convey the physics incumbent in advanced RANS/RSCM methods to SRS subgrid closures. The near-wall flow physics is amenable to one-point closure as has been demonstrated by the success of RANS closures. LES and SRS subgrid closure models are yet to fully exploit this advantage. Inadequate near-wall strategy leads to log-layer mismatch in LES and gray (RANS to LES transition) area issues in Z-SRS methods.

It is well-accepted that the DNS study of coherent structures in turbulence takes an excessive computational effort. The main question that has yet to be answered is *Can wall-resolved PANS capture the flow physics and structures adequately with much less computational effort compared to DNS? If so, what is the required level of resolution?* Toward this end, features of turbulence in the subfilter scales have to be characterized by physics-based equations.

Prescription of perturbed inflow condition for spatially evolving turbulent flows is another important controlling measure which has not yet been addressed. In PANS, evolution of length and velocity scales of unresolved turbulence is defined by two-equation closure. The prescription of

modeled kinetic energy and modeled dissipation rate (or turbulence frequency) at the perturbed inflow must be consistent with the resolved field to ensure the functionality of the model.

Although the concepts, developed in this research, are in the context of PANS method, the fundamental findings will also benefit other SRS approaches.

1.3 Dissertation outline

This thesis is organized as follows. Chapter II provides a literature survey of previous works relevant to the current studies. Chapter III presents the PANS methodology and identifies challenges which are addressed in this thesis. The development of PANS near-wall closure modeling and application to turbulent channel flow at $Re_\tau = 180, 550, 950$ is presented in Chapter IV. Chapter V discusses the development of consistent perturbed inflow for PANS and its application to spatially evolving turbulent boundary layers in the range of $650 \leq Re_\theta \leq 1434$. Chapter VI presents the PANS simulation of laminar-to-turbulent K-type transition over a flat plate. The thesis concludes with a summary of all important findings in chapter VII.

2. LITERATURE SURVEY

2.1 Near-wall subgrid modeling

In chapter 4, we will develop a near-wall model for SRS computations. One of the main differences between PANS and LES is the nature of filtering. In LES, the filter size is commensurate with the grid spacing, while in PANS the filter width is proportional to the resolution control parameters. When it comes to real-world engineering applications, the high grid resolution requirements in the near-wall region impose strenuous computational demands. Near-wall turbulence modeling is a technique towards alleviating the strict resolution requirements of the viscous layer in SRS (37). The 'wall-modeled' LES (WM-LES) is motivated using the equilibrium arguments of RANS (38). There have been many attempts to reduce the LES computational cost at the wall by incorporating features of EBL into subgrid stress models (39; 40; 41; 42). Yang and Bose (38) argue that the equilibrium wall model in turbulent channel flow results in reasonable agreement with DNS. While the resulting WM-LES approaches have achieved success, there is opportunity for further improvement of SRS models in the near-wall region.

The turbulent channel flow has already been extensively analyzed with Direct Numerical Simulations in (43; 44; 45). Theodorsen (46) is amongst the first who argue that structures similar to 'horseshoe vortex' exist in the wall-bounded turbulence. As to the dynamics of flow, there is a rich body of literature on the arrangement of turbulence structures within the channel flow over a wide range of Reynolds numbers (47; 48; 49; 50; 51) and for differnet types of applications (52; 53; 54; 55; 56; 57; 58). The existence of vortex packets is considered a universal feature of wall-bounded turbulence (48; 49). The visualization of coherent structures have been accomplished either using highly accurate DNS experimentations or highly accurate experimental observations. Adrian and Liu (49) report that visualization of even a single hairpin in a fully turbulent flow needs a careful examination and is regarded as a tricky study. In the first study, the benchmark channel flow problem has been chosen in order to demonstrate that PANS has the capability of capturing

the flow physics in wall-bounded flows. Also, the visualization of hairpin packets using PANS is sought.

2.2 Physical inflow boundary condition for spatially-evolving flows

In chapter 5 chapter, we will propose a physics-based perturbed inflow condition for the simulation of spatially-evolving turbulent flows. Flow dynamics of zero-pressure-gradient flat-plate boundary layer heavily relies on the inflow characteristics (4; 59; 5; 60; 61; 62; 63). Regarding the spatial analysis of turbulent boundary layers, there have been numerous techniques in literature in order to drive the flow to fully-developed equilibrium state. Streamwise inhomogeneity in spatially evolving flows have been treated using different techniques: (i) employing a precursor homogeneous channel flow simulation (64); (ii) using spatio-temporal cyclic condition in the streamwise direction (4; 65) and (iii) implementing concurrent internally-mapped inflow condition (66).

Regarding the first approach, inflow is extracted from a precursor channel flow simulation and introduced at the inlet of the main domain. Due to the one-way coupling, there is no information transfer from the main to the precursor computation. Besides, the storage of a large amount of information from the precursor simulation can be challenging (64). Also, the precursor computation might be as expensive as the main simulation which would not be reasonable for practical applications.

In the second category, two workflows have been proposed in literature based on employing: (a) coordinate transformation (4), (b) fringe zone (65; 8). Much of the theoretical advancements on ZPGFPBL started from the DNS of Spalart (4), where the author employs the cyclic condition in the stream parallel direction by accounting for the streamwise inhomogeneity through additional source terms in the Navier-Stokes equations. Using a spatio-temporal approach, statistics are reported at four streamwise stations: $Re_\theta \approx 225, 300, 670$ and 1410, with Re_θ being a measure of the streamwise position. Schlatter *et al.* (65) present a DNS of ZPGFPBL at $Re_\theta = 2500$. They employ the cyclic condition in the streamwise direction by recasting the outflow within a 'fringe zone' to the inlet momentum thickness. Schlatter and Orlu (67) report a DNS study of boundary layer flow and report how the tripping effects using localized random disturbances change the dy-

namics of the flow at low Reynolds numbers. Schlatter *et al.* (8) also study large eddy simulation (LES) of boundary layer over a flat plate with zero-pressure-gradient. Their computation covers $Re_\theta = 189 - 4300$ with 605 million grid points. Similar to their DNS setup, accounting for the streamwise inhomogeneity is reflected by adding a 'fringe region' at the end of the domain.

In the case of superimposing disturbances over a laminar profile, either random or deterministic, the transition to fully-developed turbulence and emergence of coherent structures occur after a long development section. Within the development section, numerical noises and spurious structures are damped out. Another downside to this method is that a priori estimation of integral quantities, e.g. momentum thickness, after the development section is not possible. In 2009, Wu and Moin (5) document a direct solution of Navier-Stokes equations for a zero-pressure gradient incompressible boundary layer for which the transition is triggered by feeding intermittent isotropic turbulence patches at the inlet. Their computation covers the range of $80 \leq Re_\theta \leq 940$ with 210 million grid points. Due to the nature of the excitation employed, it is foreseeable that the equilibrium state is not reached before $Re_\theta \approx 750$ (5). This substantiates the importance of the last class of inflow conditions (synthetic perturbed inflows), which are the basis of the second study in this thesis. In this category, attempts have been made to prescribe the inflow properties according to physics based scaling laws such that spurious structures fed at the inlet are minimized. As a subcategory, Lund *et al.* (66) propose the perturbed inflow velocity field, rescaled/recycled from a downstream recycling station, for LES computations. Siemens *et al.* (63) report a high-order accurate DNS of ZPGFPBL for the range of $620 \leq Re_\theta \leq 2140$ using Lund's recycling/rescaling inflow. All of these efforts have been made for DNS and LES computations. However, PANS-SRS requires not only prescription of the perturbed velocity field, but also consistent scaling of turbulence quantities (e.g. k, ϵ, ω) at the inlet.

2.3 SRS of laminar-turbulent transition

In chapter 6, we will have a discussion on the PANS study of natural K-type laminar-to-turbulent transition. There is a rich body of articles on the transition from laminar-to-turbulent over flat plates. Schubauer and Skramstad (68) were the first who argued that the 'temporal' sim-

ulation analysis cannot account for the 'non-parallel effects' in the non-linear stage of instability development. Therefore, convective instabilities oblige scientists to follow spatially-evolving flow simulations and analyses. Experiments of Kachanov and Levchenko (69) serves as the benchmark work for Klebanov-type ('K-type') and Herbertand-type ('H-type') transitions. In the same setup, the K-type transition occurs earlier than H-type transition, meaning the post-transition and turbulent regimes will be reached faster. Hence, the computational study of K-type transition requires a more strenuous grid resolution compared to the H-type transition. Rist and Fasel (70) reproduce the results of Kachanov and Levchenko for the K-type natural transition by mimicking their experimental setup. Due to the high computational demand of the DNS of K-type transition, they only reproduce the non-linear interaction and breakdown of the laminar flow. DNS of Sayadi *et al.* (10), however, reach to the fully-developed turbulence by a huge number of grid points.

Nearly all the available scale-resolving computations in literature report on the H-type transition. Huai *et al.* (71) present LES of H-type laminar-to-turbulent transition over a flat plate. They show how the localized dynamic model of eddy viscosity in LES can predict the development of disturbances from linear growth to fully-developed turbulence. Although the overshoot of skin friction coefficient in the post transition is not captured in their results. Sayadi and Moin (72) carry out a grid resolution study of controlled transition over a flat plate using LES with different subgrid scale models. In their work, with the level of resolutions studied, K-type transition is not reconstructed. Lozano-Duran *et al.* (73) study the evolution of H-type transition using both wall-modeled and wall-resolved LES, coupled with the parabolized stability equations (PSE), representing the linear growth of modes. Since the wall-modeled LES relies on the developed log-layer profile, wall-modeling cannot be successful in the post-transition region. They argue that the wall-resolved LES is required to capture the evolution of non-linear instabilities in the post-transition region. Kim *et al.*(74), and Jee *et al.* (75) report on the H-type transition using wall-resolved LES coupled with PSE. Yin and Durbin (76) also study H-type transition of laminar boundary layer over a flat-plate using the adaptive detached eddy simulation. The third study of this thesis tries to reproduce the laminar-to-turbulent natural K-type transition using an affordable

PANS simulation.

3. PANS METHODOLOGY AND OBJECTIVES OF THE PRESENT STUDY

The continuity equation together with the Navier-Stokes equations form a coupled and non-linear system of partial differential equations (PDEs) which fully describe the velocity and pressure evolution of incompressible flow fields:

$$\frac{\partial V_i}{\partial x_i} = 0, \tag{3.1}$$

$$\frac{\partial V_i}{\partial t} + V_j \frac{\partial V_i}{\partial x_j} = -\frac{\partial p}{\partial x_i} + \nu \frac{\partial^2 V_i}{\partial x_j \partial x_j}, \tag{3.2}$$

where V and p represent the instantaneous velocity and pressure fields, respectively. Here, density is absorbed into the pressure term. Using PANS implicit filtering, the velocity and pressure fields can be decomposed into filtered and fluctuating parts:

$$V_i = U_i + u_i', \quad U_i = \langle V_i \rangle, \quad \langle u_i' \rangle \neq 0, \tag{3.3}$$

$$p = P + p', \quad P = \langle p \rangle, \quad \langle p' \rangle \neq 0. \tag{3.4}$$

In the equations above, angle bracket and prime symbols denote the filtered and fluctuating quantities, respectively. Substituting the decomposed flow properties in equation (3.2) and considering the commutation of applied filter with respect to temporal and spatial derivatives, the filtered momentum equation reads as:

$$\frac{\partial U_i}{\partial t} + U_j \frac{\partial U_i}{\partial x_j} = -\frac{\partial \tau(V_i, V_j)}{\partial x_j} - \frac{\partial \langle p \rangle}{\partial x_i} + \nu \frac{\partial^2 U_i}{\partial x_j \partial x_j}. \tag{3.5}$$

Taking the divergence of the momentum equation (equation 3.5), and recalling that the velocity field is divergence free (equation 3.1), we obtain the following filtered Poisson equation describing

the ellipticity of the pressure field in incompressible flows:

$$-\frac{\partial^2\langle p\rangle}{\partial x_i\partial x_i} = \frac{\partial U_i}{\partial x_j}\frac{\partial U_j}{\partial x_i} + \frac{\partial^2\tau(V_i,V_j)}{\partial x_i\partial x_j}. \tag{3.6}$$

In equations (3.5) and (3.6), $\tau(V_i, V_j)$ represents the generalized 'subfilter stress' (SFS) which is the communicator between the resolved and unresolved fields. The influence of the unresolved field on resolved velocity-field evolution is manifested *via* the generalized subfilter stress $\tau(V_i, V_j)$ (77). The goal of any bridging SRS model is to develop a suitable closure for the subfilter stress (SFS). The general form of the subfilter stress, $\tau(V_i, V_j)$ is represented as (77):

$$\tau(V_i, V_j) \;\; = \;\; \langle V_iV_j\rangle - \langle V_i\rangle\langle V_j\rangle. \tag{3.7}$$

The PANS bridging SRS approach is based on the premise that RANS-type turbulence closure are well suited for SFS closure as they were originally developed to represent the physics of the entire spectrum of scales on the mean flow. Accordingly the original PANS works (21; 22) develop the physical foundation and mathematical framework to adapt RANS models for filtered flow fields.

In principle, any RANS closure including full Reynolds Stress Closure Model (RSCM) that solves transport equations for all Reynolds stress components can be adapted to the PANS framework. However, the more sophisticated RANS models will increase the stiffness of the equations and the complexity of the computations. It is therefore important to consider the overall benefits of using higher-level closures. There are two main reasons for employing more complex closure models in RANS context: (i) anisotropy and non-linearity of the constitutive relation; and (ii) non-local effects of turbulence due to history effects and the elliptic nature of pressure. Both these effects are strong functions of wave number. With increasing wave numbers, these effects become less and less significant. In a SRS computation, when the cut-off wave-number is high enough to capture any resident coherent structures (i) much of anisotropy and non-locality effects are captured in the resolved scales; and (ii) any of these effects residing in the unresolved scales do not significantly

affect the main statistics of the flow field. For these reasons, in this work, we utilize the simple and robust Boussinessq approximation (21) for the subgrid stress:

$$\tau(V_i, V_j) = \frac{2}{3} k_u \delta_{ij} - 2\nu_u \bar{S}_{ij}; \quad \nu_u = \frac{k_u}{\omega_u}; \quad \omega_u = \frac{\epsilon_u}{\beta^* k_u}, \tag{3.8}$$

in which ν_u, $S_{ij} = \frac{1}{2}(\frac{\partial U_i}{\partial x_j} + \frac{\partial U_j}{\partial x_i})$, k_u, ϵ_u, ω_u and β^* are the unresolved eddy viscosity, strain rate tensor of the resolved field, unresolved kinetic energy, unresolved dissipation rate, unresolved specific dissipation rate, and closure coefficient, respectively. The overbar identifies the time-averaged quantities. The goal of PANS closure is to derive suitable evolution equations for the kinetic energy and (specific) dissipation of the unresolved field as a function of the desired resolution. The motivation for a two-equation closure stems from the fact that, at a minimum, unresolved-field length and velocity scales are required to specify SFS with some degree of generality. As the magnitude of SFS increases, the influence of unresolved field on the resolved part rises, and the filtered field cannot retain unsteady fluctuating motions (78). In other words, more scales of motion are suppressed as a result of an increase of the eddy viscosity (large P/ϵ).

The near-wall modeling of turbulent flow fields is one of the main challenges involved in the scale-resolving simulations. It's been known that $k-\omega$ closure demonstrates superior performance for wall-bounded and low-Reynolds-number near-wall turbulence. In PANS this argument holds at the expense of a high grid resolution at the near-wall region. The derivation of the PANS subfilter scale modeling starts from the standard $k-\omega$ two-equations closure. For which, the unresolved length-scales are computed from k and ω equations. This two-transport-equation modeling solves one equation for the turbulent kinetic energy (k) and one equation for the specific turbulent dissipation rate (or turbulent frequency) (w).

In terms of the distribution of the resolution control parameters, the PANS method can be used in two different modes: constant-f_k (uniform filter) or variable-f_k (non-uniform filter) simulations. Constant-f_k formulation, which is the subject of this research, is extremely useful from an analytical view-point. This formulation permits rigorous theoretical analysis using the paradigm that

PANS is equivalent to DNS of a non-Newtonian fluid with variable viscosity. Indeed, Kolmogorov hypotheses can be formally adapted to a PANS flow field (Reyes, Cooper and Girimaji, 2014). Variable-f_k formulation – which we call WM-PANS – is more useful for simulation of near-wall and complex geometry flows, wherein large changes in resolution are needed (24). The commutation residue arising from changing filter size is formally modeled using total energy conservation principle in Girimaji and Wallin (2013).

PANS is a scale resolving simulation wherein the subgrid model is derived from RANS closure using the scale invariance property of Navier-Stokes equations. It can be shown that two parameters - unresolved velocity scale and unresolved length scale - are needed to completely describe the unresolved flow field. Hence, the PANS subfilter closure is at a minimum a two-equation model. As discussed, this research is based on the two-equation k-ω RANS model. In PANS the sensitivity of the closure model to the cut-off length scale is achieved via two *resolution control parameters:* unresolved-to-total ratios of kinetic energy and dissipation rate (21):

$$f_k = \frac{k_u}{k}; \quad f_\epsilon = \frac{\epsilon_u}{\epsilon}; \quad f_\omega = \frac{\omega_u}{\omega} = \frac{f_\epsilon}{f_k}. \tag{3.9}$$

Only two of the above three ratios are independent. The two independent parameters determine the effective cut-off length scale of the simulation as a function of the Reynolds number and are called the resolution control parameters. These control parameters prescribe the effective viscosity due to the unresolved scales. Smaller the effective viscosity, more and more scales of the resolved field will be liberated.

In this thesis, the filtering is carried out by imposing a fixed level of scale resolution and creating a cut-off in the energy spectrum. The cut-off, in turn, is specified by defining the ratios of the unresolved-to-total kinetic energy ($f_k = k_u/k$) and unresolved-to-total specific dissipation rate ($f_\omega = \omega_u/\omega$) (21; 79). Hence, a proper filtering operation by partial-averaging of the flow statistics is defined. Non-universal large-scale structures are calculated from the Partially-Averaged Navier-Stokes equations, and isotropic small scales are modeled by the modified transport equations. In

spite of the existence of a great body of literature on turbulence modeling, the literature lacks enough discussion on the transport closure models of scale-resolving simulations.

In high Reynolds number flows, it can be reasonably assumed that all of the dissipation is contained in modeled scales, leading to $f_\epsilon = 1.0$. Thus at high Reynolds numbers, only one parameter (f_k) needs to be specified. For simulating low Reynolds number flows, both independent parameters need to be specified. The quantitative criteria for determining optimal f_k value is discussed in Pereira *et al.* (80).

In SRS the smallest resolved scale (η_r) is referred to as the computational Kolmogorov scale which is approximated by:

$$\eta_r = (\frac{\nu_u^3}{\epsilon_u})^{1/4}, \tag{3.10}$$

where, ϵ_u is the subfilter (unresolved) dissipation rate. The modeled eddy viscosity (ν_u) is expressed as:

$$\nu_u = c_\mu \frac{k_u^2}{\epsilon_u}. \tag{3.11}$$

By substituting scaling relations into the modeled turbulent kinetic energy ($k_u = f_k k$), and assuming that the total dissipation rate lies within the subfilter range ($f_\epsilon = 1$), η_r can be rewritten in the form:

$$\eta_r = c_\mu^{3/4} (\frac{f_k^{3/2} k^{3/2}}{\epsilon}). \tag{3.12}$$

On the other hand, the length-scale of large energy containing eddies (integral length scales) is given by:

$$\Lambda = \frac{k^{3/2}}{\epsilon}. \tag{3.13}$$

After substituting equation (3.13) into equation (3.12), the relation between the computational Kolmogorov and integral length scales takes the form:

$$\eta_r = c_\mu^{3/4} f_k^{3/2} \Lambda. \tag{3.14}$$

Based on the definition, the computational Kolmogorov length scale has to be greater than the

numerical grid size ($\eta_r \geqslant \Delta$). Subsequently, the following relation defines the lower bound of the resolution control parameter for a specific grid size (Δ):

$$f_k \geqslant \frac{1}{c_\mu^{1/2}}(\frac{\Delta}{\Lambda})^{2/3}. \tag{3.15}$$

Model equations for the unresolved turbulent kinetic energy (k_u) and specific dissipation rate (ω_u) as functions of resolution control parameters are derived from parent RANS equations using averaging invariance principle (77) and fixed point analysis in homogeneous turbulence flows in Girimaji *et al.* (22). These equations are given by:

$$\frac{\partial k_u}{\partial t} + U_j\frac{\partial k_u}{\partial x_j} = P_u - \beta^* k_u\omega_u + \frac{\partial}{\partial x_j}((\nu + \frac{\nu_u}{\sigma_{ku}})\frac{\partial k_u}{\partial x_j}), \tag{3.16}$$

$$\frac{\partial \omega_u}{\partial t} + U_j\frac{\partial \omega_u}{\partial x_j} = \alpha\frac{P_u\omega_u}{k_u} - \alpha\beta^*\omega_u^2 + \alpha\beta^*\frac{\omega_u^2}{f_\omega} - \beta\frac{\omega_u^2}{f_\omega} + \frac{\partial}{\partial x_j}((\nu + \frac{\nu_u}{\sigma_{\omega_u}})\frac{\partial \omega_u}{\partial x_j}), \tag{3.17}$$

where the closure coefficients are: $\beta^* = 0.09$, $\alpha = 5/9$, and $\beta = 0.075$. The last term on the right hand side of the above evolution equations represents the transport effects. The turbulent transport closure is not a part of the homogeneous flow fixed point analysis. In the original works (21; 22), simple scale-interaction arguments are used to suggest a range of physically permissible unresolved kinetic energy and dissipation Prandtl numbers.

Over the last decade, the PANS methodology has experienced several important developments:

1. The paradigm that PANS is a DNS of a variable viscosity medium is developed in Reyes *et al.* (23) to adapt Kolmogorov hypotheses to characterize the unsteady features of the simulated flow field. It is shown that PANS unsteady field captures important high-order and multi-point statistics of turbulence in accordance with Kolmogorov theory.

2. Closure model for commutation residual terms is derived in Girimaji and Wallin (81) from conservation of total energy principle.

3. The DNS of variable viscosity paradigm is used to derive important criteria for optimal PANS resolution in flows with spatially evolving coherent structures (80).

4. PANS has been bench-marked against DNS, LES and experimental data in several canonical flows (82; 25; 83; 84; 27; 26).

5. A near-wall low Reynolds number version of PANS is developed in (84) but it does not address turbulent transport closure.

As mentioned in the introduction, the objective of the present study is to formally derive and validate the PANS turbulent transport model using the EBL analysis.

3.1 Thesis objectives

The premise of this thesis is that a successful predictive SRS computation requires an accurate subgrid or subfilter closure model with a broad range of applicability, along with deterministic boundary conditions for the unresolved turbulence profiles. For the near-wall modeling, the theoretical development of a turbulent transport closure in the equilibrium boundary layer is addressed through modifying the turbulent Prandtl coefficients. The modification is based on the equilibrium boundary layer (EBL) analysis. It is also tried to show how this analysis is consistent with the physics of transport in wall-bounded turbulence for three different benchmark cases. One of the main explanations to this consistency is that the transport of subgrid scale turbulence can be treated well using the EBL assumption. In this way, the following tasks are undertaken:

(i) To advance the SRS approaches for wall-bounded flows using the equilibrium boundary layer analysis.

(ii) To carry out temporal PANS simulation of turbulent boundary layers.

(iii) To develop a physics-based perturbed inflow field for spatial analysis of fully-developed turbulent flows.

(iv) To carry out spatial PANS simulation of transitional and turbulent boundary layers.

3.1.1 Near-wall model development

In the first study, we develop bridging SRS (B-SRS) partially-averaged Navier-Stokes (PANS) near-wall closures that overcome the log-layer mismatch. In PANS the filtered flow equations are supplemented with model equations for unresolved kinetic energy and (specific) dissipation. The filtered kinetic energy and (specific) dissipation equations are subject to equilibrium boundary layer scaling, leading to closure expressions for SRS turbulent transport models. The degree of filtering is characterized in terms of the ratio of resolved-to-total kinetic energy (k) and dissipation. For the proof of concept, an investigation of the equilibrium-boundary-layer (EBL) model is carried out by a detailed comparison with the DNS data of Hoyas and Jimenez (2) for turbulent channel flows. Turbulent channel flow PANS simulations are performed at various Reynolds numbers and degrees of resolutions to confirm the scaling relationships and to validate the transport closure models. It is established that the resolution criteria is objective oriented in that achieving convergence in terms of higher order statistics requires not only a high numerical (grid) resolution but also a high physical resolution (small f_k). We employ the planar analysis to manifest the sweep and ejection mechanisms dictating the physics of momentum transport. In terms of the multi-point physics, this PANS study not only evaluates single hairpin structures, but it also studies the organization of structures in tandem. The resolved coherent structures with PANS are compared with those reported by Adrian (50) and Jimenez and Lozano-Duran (51). This work investigates the hairpin packet paradigm, and also the capability of the equilibrium boundary layer analysis in capturing the so-called 'hairpin vortex packet' in the complex fully turbulent environment.

The following tasks are undertaken in the first study:

(i) To present equilibrium boundary layer analysis performed for bridging scale-resolving simulations: Analysis leads to closure model (σ_{ku},$\sigma_{\epsilon u}$) as a function of partition(f_k,f_ϵ)

(ii) To examine the validity of the EBL model in terms of the one-point first and second order statistics of the velocity field, along with the multi-point physics and vortex dynamics as to the topology of coherent structures.

3.1.2 Inflow condition for unresolved turbulence profiles

In the second study, we develop a physics-based perturbed inflow condition for bridging scale-resolving simulations (B-SRS) of spatially evolving problems. The SRS approach of choice is the partially-averaged Navier-Stokes (PANS) model. PANS adapts two-equation RANS approaches to model different degrees of scale resolution based on the objective function defined a priori. For the proof of concept, a systematic study of zero-pressure-gradient flat-plate boundary layer (ZPGFPBL) with a continuous range of Reynolds number based on the momentum thickness ($650 \leq Re_\theta \leq 1434$) is presented. When it comes to 'spatial' simulations, implementing proper inflow and outflow boundary conditions are of critical importance. In order to circumvent the need for a lengthy development section for the development of organized turbulent motions and to have control over the skin friction and integral thicknesses at the end of the development section, we adapt the recycling/rescaling method of Lund *et al*. (66) to B-SRS. According to this method, the velocity field at a downstream station is rescaled and reintroduced at the inlet, and the turbulence profiles are scaled using the equilibrium nature of logarithmic layer.

The accuracy of the results in terms of higher order statistics and multi-point physics is examined. The integral quantities, mean velocity, Reynolds stresses, skewness and flatness, two-point correlation and near-wall coherent structures are meticulously studied. The organization of near wall structures are also examined through study of two-point correlation of different components of the fluctuating velocity. The hairpin forest, which is considered the signature of boundary layer flow in moderate Reynolds number flows (5), is meticulously studied. In order to obtain realistic turbulent structures and the 'forest of hairpins' in a spatially-evolving PANS simulation, different properties as to the grid resolution, numerical scheme, initial state, and the accurate prescription of the inflow turbulent eddies as a function of time have to be properly dealt with.

The main question that arises is how expensive it would be to run the spatially evolving flow using the PANS model as opposed to DNS. One of the important features of this study is that the underlying physics is recovered with a less computational cost compared to LES (8) and far less compared to DNS (5). It is worth noting that when it comes to higher ranges of Re_θ, specification

of an optimum spatial distribution of physical and computational resolutions can save significant computational resources.

For this study, the following tasks are performed:

(i) To develop a fully-deterministic perturbed inflow field for the resolved velocity and unresolved turbulence quantities for a spatially growing boundary layer.

(ii) To assess all the underlying physics of a turbulent boundary layer as to single and multi-point statistics and coherent structures.

3.1.3 Lamniar-to-turbulent transition

For the last study, we address the laminar-to-turbulent transition using PANS methodology. We focus on the evolution of unstable Tollmien-Schilchting waves fed using an unsteady zero net mass flux blowing/suction strip. This method of excitation was first introduced by Rist and Fasel (70). Frequencies of the two-dimensional Tollmien-Schlichting (TS) and oblique waves are chosen based on experiments of Kachanov and Levchenko (69). There has already been a number of DNS works on the transition phenomenon over a flat-plate. According to the physics of the problem, spatial evolution of the turbulence structures imposes a critical requirement on the computational resolution. Hence, providing such level of resolution can be unfeasible in capturing unstable modes of flow in real-life applications. The main impetus of the third study is to employ PANS method to resolve only the dynamically prominent scales, dictating the physics. It's been tried to show how systematic modeling of the effect of unresolved on resolved scales using the PANS approach leads to vast saving in terms of the CPU time. It should be noted that the initial growth of the perturbations is highly dependent on the level of subfilter eddy viscosity. The proper transfer of energy from the resolved to unresolved scales plays a key role in the non-linear dynamics. In other words, in the non-linear stage of transition, energy exchange between the modeled and resolved part has to be recovered so that the growth of perturbations is predicted. Hence, a key objective of this study is to assess the performance of PANS in terms of prediction of transition point and skin friction overshoot by scrutinizing the evolution of skin friction coefficient in the streamwise

direction.

In terms of the level of eddy viscosity within the computational domain, the computational discretization methods have to be aslo chosen such that the least amount of numerical diffusion is imposed. The demonstration of autogeneration mechanism occurring after the post-transition region is also sought in this work. It's been well-known that the autogeneration mechanism is responsible for formation of forests of hairpins. This mechanism is manifested in terms of obtaining the lag-law behavior of the velocity, as well as settling asymptotically to the fully-developed state of turbulence in the skin friction coefficient plot. The main goals of this study are as follows:

(i) To excite the flow by three-dimensional interaction between TS and oblique waves through applying an unsteady zero net mass flux blowing/suction strip.

(ii) To examine the evolution of flow dynamics while transitioning from laminar-to-turbulent at different downstream locations.

4. SCALE RESOLVING SIMULATION OF TURBULENCE: EQUILIBRIUM BOUNDARY LAYER ANALYSIS LEADING TO NEAR-WALL CLOSURE MODELING[1]

4.1 Introduction

In recent years scale-resolving simulations (SRS) have emerged as an attractive option for computing complex turbulent flows of engineering interest. In order to achieve reasonable results at an affordable computational cost, SRS is envisioned to selectively resolve only vital large-scale turbulence structures on a 'accuracy-on-demand' basis. The SRS methods can be broadly classified into two categories: zonal and bridging approaches. In zonal approaches the partitioning of the flow field into high and low fidelity parts occurs in physical space. In the regions of the flow with complex coherent structures, the flow field is computed with high-fidelity large-eddy simulations (LES). Other regions of canonical turbulence are computed with Reynolds-averaged Navier-Stokes (RANS) models. Thus, zonal models achieve computational savings due to the use of inexpensive RANS in flow regions of simple turbulence features. The main challenge in the SRS zonal approach is the treatment of the 'hand-shake' or 'grey' region at the interface of the RANS and LES domains. On the other hand, much like LES, the bridging SRS approach uses the same filtered Navier-Stokes equations throughout the flow domain. The key differences between LES and bridging SRS methods are: (i) the bridging SRS methods are intended for resolving a much narrower range of scales than LES; (ii) the SRS filter is implicit and the cut-off length scale is determined by the effective eddy viscosity; and (iii) the SRS closure models solve additional equations for computing the eddy viscosity of the unresolved scales of motion. The SRS effective cut-off can be varied by suitably modifying the coefficients in the eddy-viscosity model equations in a manner consistent with turbulence physics. The main challenge of bridging SRS approach is to develop subgrid stress model equations that are suitably sensitive to the implied cut-off length. In principle, bridging SRS computation reduces to RANS in the low-resolution limit and asymptotes

[1]Reprinted with permission from P. Tazraei and S. S. Girimaji, "Scale-resolving simulations of turbulence: Equilibrium boundary layer analysis leading to near-wall closure modeling," *Physical Review Fluids*, vol. 4, no. 10, p. 104607, 2019. Copyright 2019 American Physical Society.

to DNS in the high-resolution limit. In order to accommodate cut-off in larger scales of motion, the bridging SRS subgrid closure model must account for more complex turbulence physics than its LES counterpart.

For computing important statistical features of turbulent boundary layers, RANS method offers useful advantages over SRS or LES. The SRS and LES approaches are inherently more accurate away from the wall as they resolve important flow features, but they can be prohibitively expensive for resolving the small scales of motion encountered at the walls. The RANS advantage at the wall is due to the fact that the closure models are derived from scaling laws established within the equilibrium boundary layer (EBL). There have been many attempts to reduce the LES computational cost at the wall by incorporating features of EBL into subgrid stress models (39; 40; 41; 42). While the resulting 'wall-modeled' LES approaches have achieved success, there is opportunity for further improvement of SRS models in the near-wall region.

The focus of this work is on the near-wall modeling for SRS approaches. The bridging SRS approach of choice in this work is the Partially-Averaged Navier-Stokes (PANS) model of Girimaji (21), which has many features in common with the single-point Partially-Integrated transport Model (PITM) (85; 18; 86). Multi-scale closure of PITM is also discussed in (87). PANS adapts and extends proven two-equation RANS or Second Moment Closure (SMC) models for representing the effects of subgrid scales on the resolved flow field. The physical rationale and mathematical framework for modifying the RANS model to represent the subgrid physics as a function of scale resolution have been developed in (22; 21; 18; 85). The motivation for using a two-equation closure is that individual evolution equations must be solved for the subgrid velocity and length scales to determine subgrid stress. This approach has already been well-documented for a variety of canonical flows (26; 27; 25). The partition between resolved and unresolved fields is effected by specifying the ratios of the unresolved-to-total kinetic energy ($f_k = k_u/k$) and unresolved-to-total specific dissipation rate ($f_\omega = \omega_u/\omega$) (21; 79). The PANS framework for adapting RANS model developed in (21; 22) does not comprehensively address the turbulent transport closure or near wall behavior. Those works propose a model based solely on scale-interaction arguments. There is a

clear and imminent need for advancing the physical fidelity of the SRS transport models.

As mentioned earlier, the RANS turbulent transport models for kinetic energy and dissipation are derived from EBL analysis. This raises the question whether a similar EBL analysis can be developed for filtered flow fields leading to SRS transport models. The RANS turbulent transport models are expected to reproduce physically consistent one-point statistics only. On the other hand, the SRS approaches are required to yield not only the correct one-point statistical behavior, but also emulate important non-local and unsteady flow features. Therefore, it is important to ensure that any SRS turbulent transport model produces one-point statistics and key coherent-structure features consistent with flow physics.

The three key objectives of the current work are:

1. Adapt and extend equilibrium boundary layer (EBL) analysis to filtered turbulent fields leading to turbulent transport models for unresolved kinetic energy and unresolved (specific) dissipation.

2. Perform SRS-PANS simulations of benchmark channel flow and evaluate the PANS behavior in equilibrium log-layer by comparison against DNS statistics of Hoyas and Jimenez (2).

3. Examine the ability of PANS to capture key qualitative and quantitative aspects of coherent structures in channel flows.

Although much of the closure model development in this work is in the context of PANS, the analytical framework and closure expressions are applicable to other bridging SRS methods.

The chapter is organized as follows. First, section 4.2 describes the equilibrium boundary layer analysis. Section 4.3 discusses the simulated test cases. In section 4.4, the results of the proposed transport model are assessed by comparing PANS results with DNS data and known features of coherent structures.

4.2 Near-wall modeling

4.2.1 Equilibrium boundary-layer analysis for RANS

We first present the RANS-EBL formulation before developing a similar analysis for filtered fields. In RANS approach, the functional form of the turbulent transport model is presumed from gradient transport hypothesis and the closure coefficient (Prandtl number) is derived using equilibrium boundary layer (EBL) analysis.

The equilibrium boundary layer is amenable to the following simplifications:

$$\frac{dk}{dt} = \frac{d\omega}{dt} = 0; \quad and \quad P = \epsilon. \tag{4.1}$$

Further, the following scaling is proposed (88):

$$k = \frac{u_\tau^2}{\sqrt{c_\mu}}; \quad \tau_{xy} = -u_\tau^2 \quad and \quad \frac{dU}{dy} = \frac{u_\tau}{\kappa y}, \tag{4.2}$$

where u_τ and κ are the friction velocity and von-Karman constant, respectively. From the above, the following expressions for production can be derived:

$$P = -\tau_{xy}\frac{\partial U}{\partial y} = \frac{u_\tau^3}{\kappa y}, \tag{4.3}$$

$$P = \nu_t(\frac{\partial U}{\partial y})^2 = \frac{k}{\omega}\frac{u_\tau^2}{\kappa^2 y^2} = \epsilon. \tag{4.4}$$

The eddy viscosity can be identified as:

$$\nu_t = \frac{k}{\omega} = \kappa u_\tau y. \tag{4.5}$$

These scalings are employed to determine σ_ω for RANS transport models (88):

$$\sigma_\omega = \frac{\kappa^2}{\sqrt{\beta^*}} \left(\frac{\beta}{\beta^*} - \alpha \right)^{-1}. \tag{4.6}$$

There is a wide range of values from 0.384 to 0.41 suggested for the von Karman coefficient in literature (89). In the current study, we use $\kappa = 0.41$ which is the standard value employed in open source and commercial codes. After substituting the values of the closure coefficients along with $\kappa = 0.41$ into the expression above, we obtain $\sigma_\omega = 2.0$. This value yields the correct slope of the log-layer in an equilibrium boundary layer. The kinetic energy Prandtl number is set to be equal to σ_ω (88):

$$\sigma_k = \sigma_\omega. \tag{4.7}$$

4.2.2 Equilibrium boundary-layer analysis for partially filtered fields

We now seek to develop a similar analysis for PANS equations of filtered fields. For practical applications, variable resolution (VR-PANS)- going from RANS at the wall to desired resolution in the wake- is desirable. For VR-PANS, additional modeling of the commutation error residue is needed (81), which will be examined in a future study. Throughout this analysis, we will assume that f_k, f_ϵ and f_ω are uniform in space for ease of EBL model derivation. For any decomposition of resolved and unresolved fields, one can write the following equations for corresponding kinetic energies:

$$\frac{dk_R}{dt} = P_r^m - \epsilon_r - \gamma_{ru} + T_r, \tag{4.8}$$

$$\frac{dk_u}{dt} = P_u^m - \epsilon_u + \gamma_{ru} + T_u, \tag{4.9}$$

here P_r^m and P_u^m are production of resolved and unresolved kinetic energy due to mean flow; ϵ_r and ϵ_u are dissipation occurring in resolved and unresolved fields; γ_{ru} is the spectral transfer of energy from resolved to unresolved fields; and, T_r and T_u are turbulent transport of respective energies.

In order for the boundary layer to be in equilibrium state, the entire energy spectrum should be

in equilibrium. Thus we propose (in a statistical average sense):

$$\frac{dk_R}{dt} \approx \frac{dk_u}{dt} \approx 0; \quad and \quad T_r = T_u \approx 0. \tag{4.10}$$

Then it follows that:

$$P_r^m - \epsilon_r - \gamma_{ru} = 0, \tag{4.11}$$

$$P_u^m - \epsilon_u + \gamma_{ru} = 0. \tag{4.12}$$

Further the overall unresolved kinetic energy production is given by:

$$P_u = \gamma_{ru} + P_u^m. \tag{4.13}$$

That is, the unresolved kinetic energy is generated directly from mean flows as well as for spectral energy transfer from larger scales. These arguments lead to the following:

$$P_u - \epsilon_u \approx 0. \tag{4.14}$$

This relationship forms the basis of the filtered EBL analysis. In EBL, we thus suggest the following simplifications to hold true on an average:

$$\frac{dk_u}{dt} = \frac{d\omega_u}{dt} = 0; \quad and \quad P_u = \epsilon_u. \tag{4.15}$$

Let us first consider the unresolved kinetic energy equation. Following the RANS analysis (88), we assume that the molecular viscosity is negligible compared to the eddy viscosity in the EBL. The energy equation is trivially satisfied confirming that

$$k_u(y) = constant, \tag{4.16}$$

within the EBL.

Now we consider the unresolved turbulence frequency equation within EBL. Once again, neglecting the effect of molecular transport within EBL leads to:

$$0 \approx \alpha \frac{\omega_u P_u}{k_u} - \beta' \omega_u^2 + \frac{\partial}{\partial y}\left(\frac{\nu_u}{\sigma_{\omega u}} \frac{\partial \omega_u}{\partial y}\right). \tag{4.17}$$

In the equilibrium boundary layer, from the definitions of k_u and ω_u, it follows that:

$$k_u = f_k k = f_k \frac{u_\tau^2}{\sqrt{\beta^*}}, \tag{4.18}$$

$$\omega_u = f_\omega \omega = f_\omega \frac{u_\tau}{\kappa y \sqrt{\beta^*}}, \tag{4.19}$$

$$\nu_u = \frac{f_k}{f_\omega} \nu_t = \frac{f_k}{f_\omega} u_\tau \kappa y. \tag{4.20}$$

After substituting for k_u and ω_u from scalings defined in equations (4.18) to (4.19) into the evolution equation of the modeled specific dissipation rate, equation (4.17), the following relationship between the modified specific dissipation rate, $\sigma_{\omega u}$, and other PANS closure coefficients is obtained:

$$\sigma_{\omega u} = \frac{f_k}{f_\omega} \frac{\kappa^2}{\sqrt{\beta^*}} \left(\frac{\beta}{\beta^*} - \alpha\right)^{-1}. \tag{4.21}$$

Comparison of equation (4.21) with the RANS counterpart (equation 4.6) leads to the following Prandtl number for unresolved turbulence frequency:

$$\sigma_{\omega u} = \frac{f_k}{f_\omega} \sigma_\omega. \tag{4.22}$$

We propose that the kinetic energy Prandtl numbers maintain the same ratio as the RANS counterpart. This leads to

$$\sigma_{ku} = \frac{f_k}{f_\omega} \sigma_k, \tag{4.23}$$

in which, σ_k and σ_ω are the RANS Prandtl numbers.

The Prandtl number for unresolved kinetic energy and dissipation obtained above from the EBL analysis is consistent with the Zero-Transport-Model (ZTM) proposed in (22). The ZTM model is obtained when the transport of unresolved turbulence due to the resolved field is negligible. In the remainder of this section we perform PANS simulations to verify and validate the proposed transport model in the turbulent channel flow.

4.3 Simulation procedure

We perform the benchmark turbulent channel flow PANS simulations using the incompressible finite volume solver in OpenFOAM (90). Table 4.1 summarizes different computational and physical resolutions of the conducted PANS simulations. DNS of Hoyas and Jimenez (2) serves as the reference for the purpose of validation study.

A computational domain of dimensions $4h \times 2h \times 2h$ respectively in the streamwise, wall-normal and spanwise directions has been considered, where h is the channel half-height. Hexahedral meshes with uniform streamwise and spanwise grid resolutions and stretched wall-normal spacing have been generated. All the grid resolutions reported in Table 4.1 are in viscous wall units.

Flow through the channel is sustained by prescribing a constant pressure gradient in the streamwise direction. Cyclic boundary condition is applied in the streamwise and spanwise directions, and no-slip condition is employed at the top and bottom walls. All of the statistics reported here are obtained by temporal averaging over $50h/u_\tau$ time units and spatial averaging in homogeneous directions.

The discretization in space and time is of second order, and the number of sub-iterations is dictated by the requirement that the residuals at each time step should not exceed 10^{-6}. In addition, in order to ensure the stability of the time integration, the maximum local Courant number is set to a conservative value – $CFL < 0.6$.

Table 4.1: Details of the test cases examined for the turbulent channel flow.

Simulation	Δ_x^+	y_1^+	Δ_z^+	Re_τ	N_y	f_k	$\sigma_{k_u}, \sigma_{\omega_u}$
Case1	11.25	0.72	5.6	180	50	0.2	0.08
Case2	34.4	1.7	17.2	550	50	0.1	0.02
Case3	34.4	0.3	17.2	550	150	0.1	0.02
Case4	34.4	0.19	17.2	550	200	0.1	0.02
Case5	34.4	1.7	17.2	550	50	0.15	0.045
Case6	34.4	1.7	17.2	550	50	0.2	0.08
Case7	23	1.7	17.2	550	50	0.1	0.02
Case8	34.4	0.19	17.2	550	200	0.1	2.0 (unmodified)
Case9	59	0.53	19	950	120	0.1	0.02
DNS1	9	-	6.7	186	97	-	-
DNS2	13	-	6.7	547	257	-	-
DNS3	11	-	5.7	934	385	-	-

4.4 Results and Discussion

The results are presented in three parts. In the first part we ensure that the key modeling assumptions are upheld in the computed results. Next, we demonstrate that the PANS single-point statistics in the EBL compare well against DNS data. Finally, the PANS vorticity structures are examined for qualitative and quantitative consistency against established experimental results.

4.4.1 Internal consistency

The principal function of any subgrid model is to simulate the correct level of eddy viscosity and ensure the overall energy level is captured. For the PANS approach to serve as a reasonable SRS scheme, it is very important to ensure that the simulation produces (i) the prescribed degree of viscosity reduction; and (ii) the correct kinetic energy balance. We will first examine if PANS simulations produce the desired behavior. In this subsection, we verify that PANS computed results are consistent with the prescribed parameters and modeling assumptions.

Consider a PANS simulation with prescribed f_k and f_ϵ or f_ω. We define the viscosity reduction factor (f_ν) as the ratio between PANS viscosity value and that of the total fluctuations or RANS

under similar conditions:

$$f_\nu \equiv \frac{\nu_u}{\nu_t}. \tag{4.24}$$

The expected or prescribed value of the ratio is:

$$(f_\nu)_{prescribed} = \frac{f_k^2}{f_\epsilon} = \frac{f_k}{f_\omega}. \tag{4.25}$$

It is reasonable to demand that, on an average, the computed results are consistent with the prescribed eddy-viscosity ratio.

For the case of channel flow, the average subgrid PANS viscosity is a function of the wall-normal distance and can be computed as follows:

$$\nu_u(y) = \overline{(k_u/\omega_u)}(y). \tag{4.26}$$

The viscosity of the total field is estimated from the computations using the total kinetic energy and total dissipation:

$$\nu_t(PANS) = c_\mu \frac{k_t^2}{\epsilon_t} = c_\mu \frac{\left(\overline{k_u} + k_r\right)^2}{\left(\overline{\epsilon_u} + \epsilon_r\right)}, \tag{4.27}$$

where k_r, ϵ_u and ϵ_r are obtained as follows from the PANS computation:

$$k_r(y) = \overline{V_i V_i} - \bar{V}_i \bar{V}_i, \tag{4.28}$$

$$\epsilon_u = \beta^* k_u \omega_u; \quad and \quad \epsilon_r = 2\nu[\overline{S_{ij} S_{ij}} - \bar{S}_{ij} \bar{S}_{ij}]. \tag{4.29}$$

A second approach to estimating the total viscosity is to perform a RANS simulation for the same flow conditions. Based on these two estimates of total viscosity, we define two metrics for computed eddy viscosity ratio:

$$(f_\nu)_{C1} = \frac{\nu_u(PANS)}{\nu_t(PANS)}, \tag{4.30}$$

and

$$(f_\nu)_{C2} = \frac{\nu_u(PANS)}{\nu_t(RANS)}. \tag{4.31}$$

First we verify the consistency between the two estimates of the computed eddy-viscosity ratio and the prescribed ratio for the case of $Re_\tau = 550$. We also include results from PANS calculation (Case 8) in which the turbulent transport is not modified according to the EBL analysis. As shown in Table 4.1, the PANS transport coefficients in Case 8 are retained at the RANS values. Figure 4.1a shows the comparison between prescribed and computed values for Case 2 ($f_k = 0.1$) in which the PANS transport coefficient is modified according to the EBL analysis. Clearly both C1 and C2 computed eddy-viscosity estimates are in good agreement with prescribed value of 0.01. In Figure 4.1b, a similar comparison is made for Case 5 ($f_k = 0.15$) in which the transport coefficients are also modified. Again the agreement between computed and prescribed ratios are in good agreement. Next, we compare Case 8 ($f_k = 0.1$) in which the transport coefficients are unmodified from RANS values (Figure 4.1c). The computed eddy-viscosity ratio is close to unity rather than the prescribed value of $f_\nu = 0.01$. This clearly demonstrates the importance of modifying the transport coefficient in accordance with EBL analysis. Unless, the transport coefficients are modified, the PANS eddy viscosity value approaches that of RANS irrespective of f_k values specified. It will be shown later that the flow structures computed in Case 8 (unmodified coefficients) do not display a large range of resolved scales.

Having established that the PANS simulation (with modified coefficients) does indeed produce the required reduction in eddy viscosity, we next investigate if the correct balance between production and dissipation is attained. Toward this end, we examine two important ratios: production-dissipation ratio of the unresolved field (P_u/ϵ_u) and total field (P_t/ϵ_t). The various production terms are obtained as follows:

$$P_u = 2\nu_u\overline{S_{ij}S_{ij}}; \quad and \quad P_t = -\overline{u_i'u_j'}\frac{\overline{\partial V_i}}{\partial x_j}. \tag{4.32}$$

It is important to note that due to the unsteady nature of P_u and ϵ_u, they have been averaged over

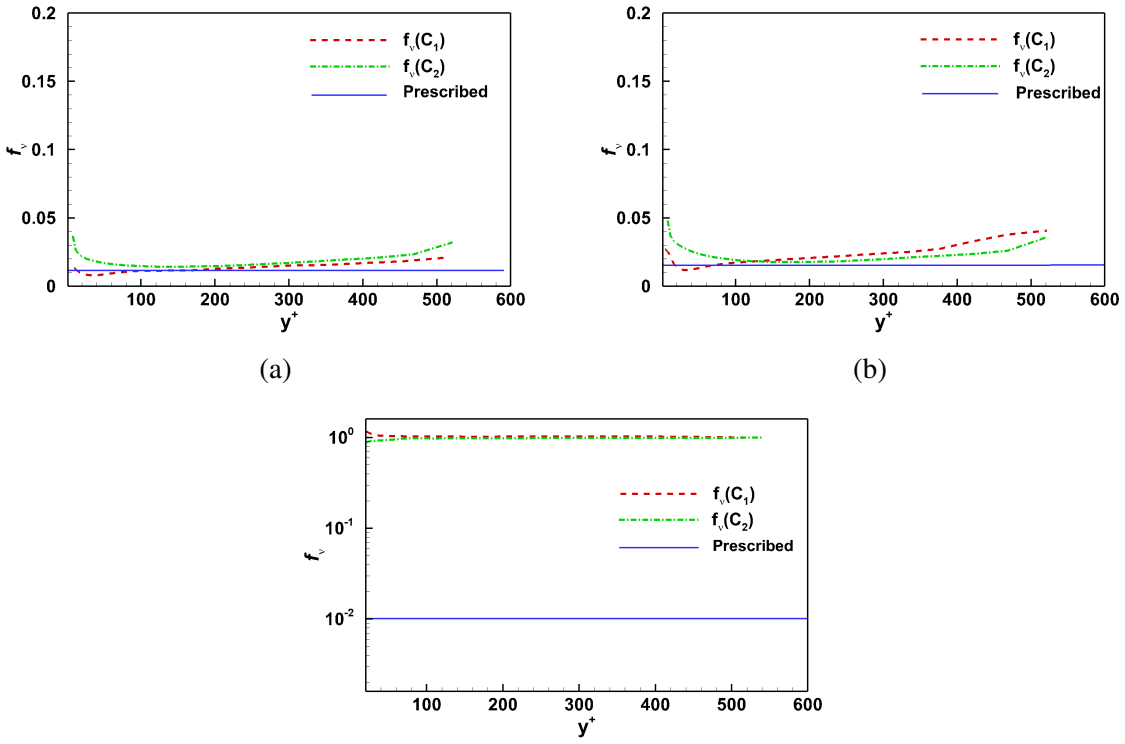

Figure 4.1: Consistency profiles for $Re_\tau = 550$: (a) Case 2, (b) Case 5, (c) Case 8.

homogeneous planes as a function of wall distance. The two important ratios as a function of wall normal distance is shown in Figure 4.2a. There is a clear balance between unresolved production and unresolved dissipation of energy within the logarithmic layer, which effectively decouples the buffer layer and wake flow regions as dictated by physics. Comparison of total production-to-dissipation ratio obtained from the same PANS simulation is now compared against the DNS data of Hoyas and Jimenez (2). Apart from the region very close to the wall, the agreement is quite reasonable.

We have now established that the PANS model produces the prescribed degree of viscosity reduction and reasonable production-dissipation balance. Now we proceed to the validation stage where the PANS statistics and flow structures are compared against established data.

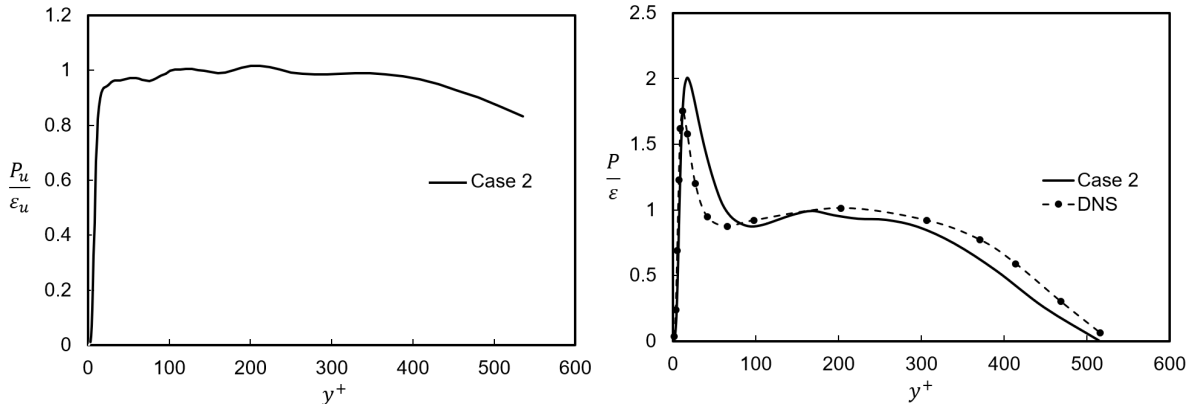

(a) (b)

Figure 4.2: Production-to-dissipation ratio for $Re_\tau = 550$ in terms of budgets of: (a) subgrid kinetic energy, (b) total kinetic energy.

4.4.2 One-point statistics

4.4.2.1 Mean flow field

The grid convergence study in terms of the mean velocity field is shown in Figure 4.3a. Cases 2, 3, and 4 in Table 4.1 examine the grid convergence in the wall normal direction, while Cases 2 and 7 assess the grid convergence in the stream parallel direction. For the cases with modified coefficients, all three grids considered ($N_y = 50, 150, 200$) converge to the DNS data. The case with unmodified coefficient (Case 8) however exhibits a significant deviation, even with the highest resolution studied ($N_y = 200$). This finding once again emphasizes the importance of turbulent-transport coefficients.

Figure 4.3b exhibits the PANS mean velocity profiles at three different Re_τ values: 180, 550 and 950. The results show that the right slope of log-layer is recovered at all Reynolds numbers.

In Figure 4.3c, the mean profiles obtained for three different f_k values are shown for the case of $Re_\tau = 550$. All these simulations are run on the coarsest grid resolution with only 204,000 grid cells. As expected, by decreasing the f_k value, a higher amount of unsteadiness within the flow field is resolved, and PANS result converges to the DNS profile.

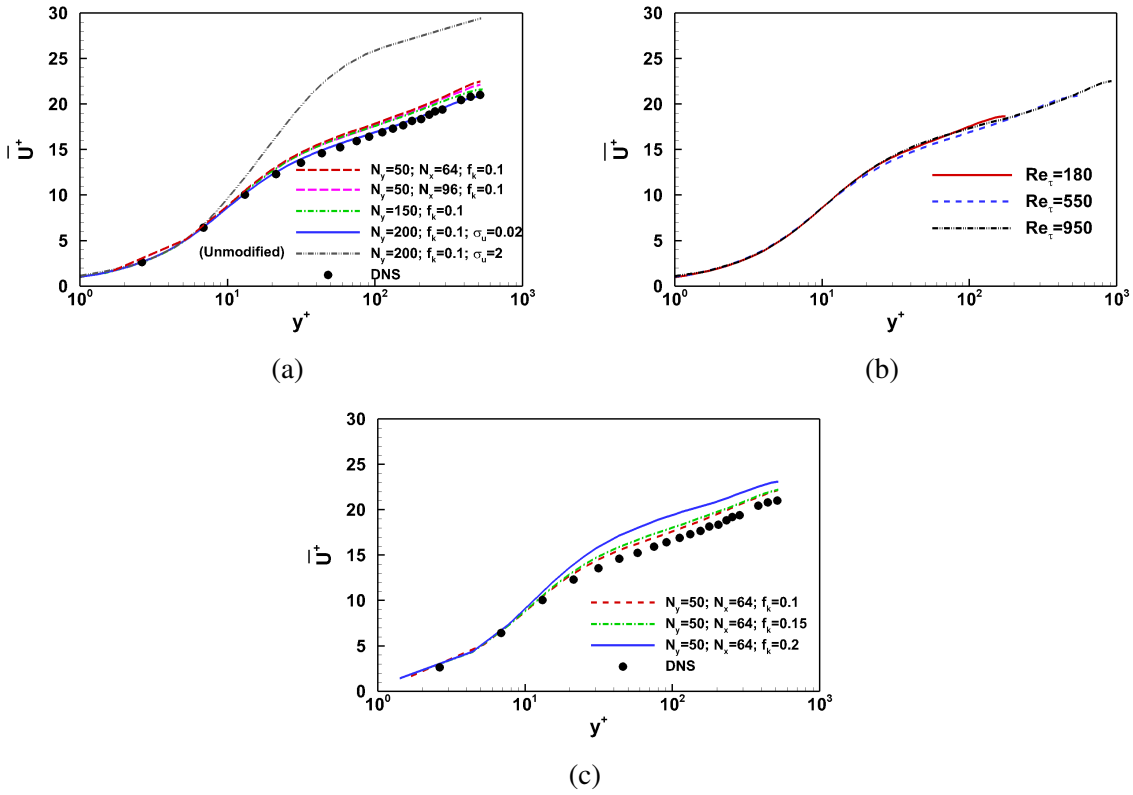

Figure 4.3: Mean velocity profiles for different simulation parameters: (a) Grid size - N_y, (b) Re_τ, (c) f_k values; The DNS data is taken from [2].

4.4.2.2 Reynolds stresses

Figure 4.4 displays the Reynolds shear stress and anisotropy profiles for $f_k = 0.1$ and $R_\tau = 550$ at different grid resolutions. For all resolutions considered, the PANS shear stress is in excellent agreement with the DNS data. The anisotropy of PANS Reynolds stresses is exhibited on the invariant map (91), shown in Figure 4.4b. All cases shown exhibit correct degree of anisotropy as a function of wall distance. The anisotropy starts at the two-component limit near the wall and proceeds toward the one-component state. Finally it evolves along the axisymmetric expansion line, approaching isotropic state near the centerline.

The f_k-dependence of the different Reynolds stress components is shown in Figure 4.5. Once again, the PANS results converge to DNS values with decreasing f_k. For the case of $f_k = 0.1$, the agreement is quite good.

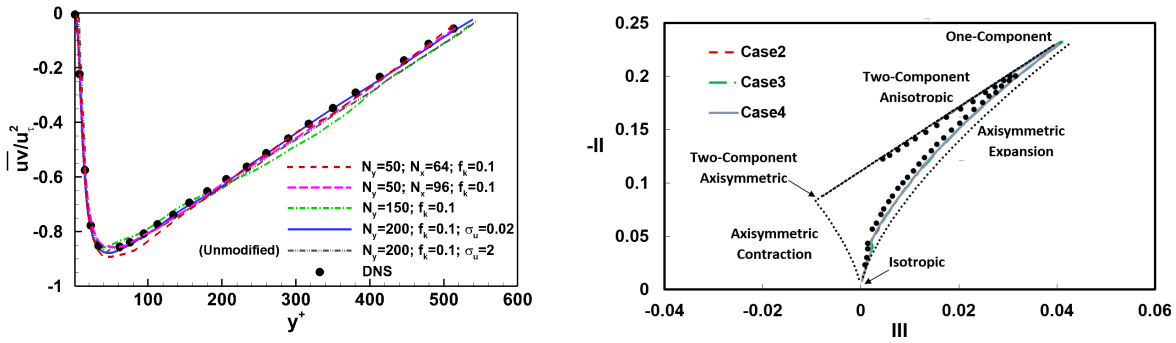

(a) (b)

Figure 4.4: Reynolds stresses at different grid resolutions for $Re_\tau = 550$: (a) shear stress profile, (b) anisotropy profile on invariant map.

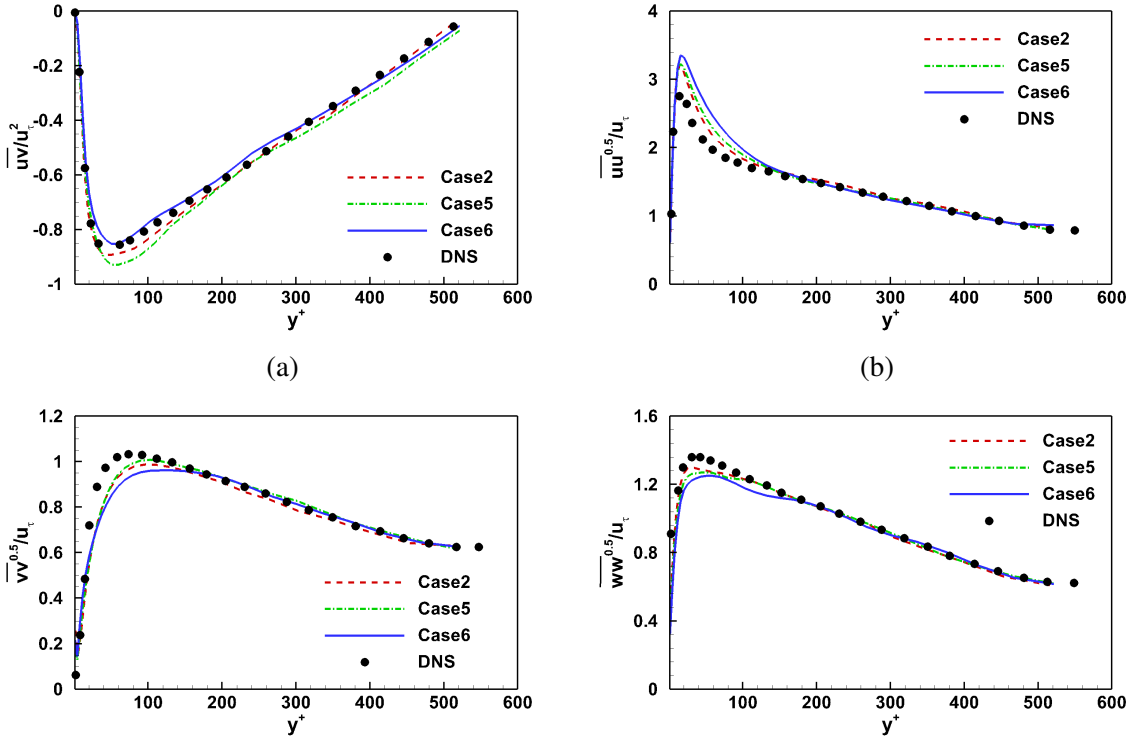

(a) (b)

(c) (d)

Figure 4.5: Reynolds stresses as a function of physical resolution (f_k) for $Re_\tau = 550$: (a) shear stress, (b) normal streamwise stress, (c) wall-normal stress, (d) normal spanwise stress.

4.4.3 Multi-point statistics and structures

4.4.3.1 Energy spectra

To demonstrate the scale-resolving capability of WR-PANS, plots of power spectral density of streamwise velocity fluctuations corresponding to Case 4 in Table 4.1 are shown in Figure 4.6. In order to obtain the temporal energy spectra, a large number of samples are recorded at three different wall-normal locations: $y^+ = 50, 100$ and 150. The spectrum is normalized by the local turbulent kinetic energy, and frequency is scaled by the centerline velocity U_c and channel half-height (h). In addition, to improve the signal clarity, Hanning window (92) has been applied to obtain the spectra. Figure 4.6 illustrates the computed spectra at the three locations. Each spectrum exhibits a -5/3 slope at the large-scale side of the inertial range. Then at smaller inertial scales, the spectrum exhibits a -7 slope. The slopes of spectra agree very well with the spectral behavior of boundary layer shown in Wu and Moin (5). Thus, PANS simulation results yield the correct spectral scaling.

4.4.3.2 Two-point correlation

To further demonstrate the ability of PANS to capture turbulence structures, we now examine the spatial two-point correlations (Figure 4.7). The PANS two-point streamwise velocity correlation function is compared against the DNS data of Sillero *et al.* (3). The agreement is reasonable for small separation distances and excellent for larger separations. The discrepancy at small separation distances is to be expected as PANS uses a closure model for representing small-scale physics. The larger scales are captured more accurately leading to better agreement of the two-point correlations at larger separation distances.

4.4.3.3 Coherent structures

In evaluating SRS methods, it is very important to look beyond low-order statistics and examine unsteady features and flow structures. Our goal here is to establish that PANS computations capture key vorticity features characteristic of boundary layers. For the purpose of vortex visualization, λ_2 iso-surfaces, representing the minimum local pressure has been employed (93).

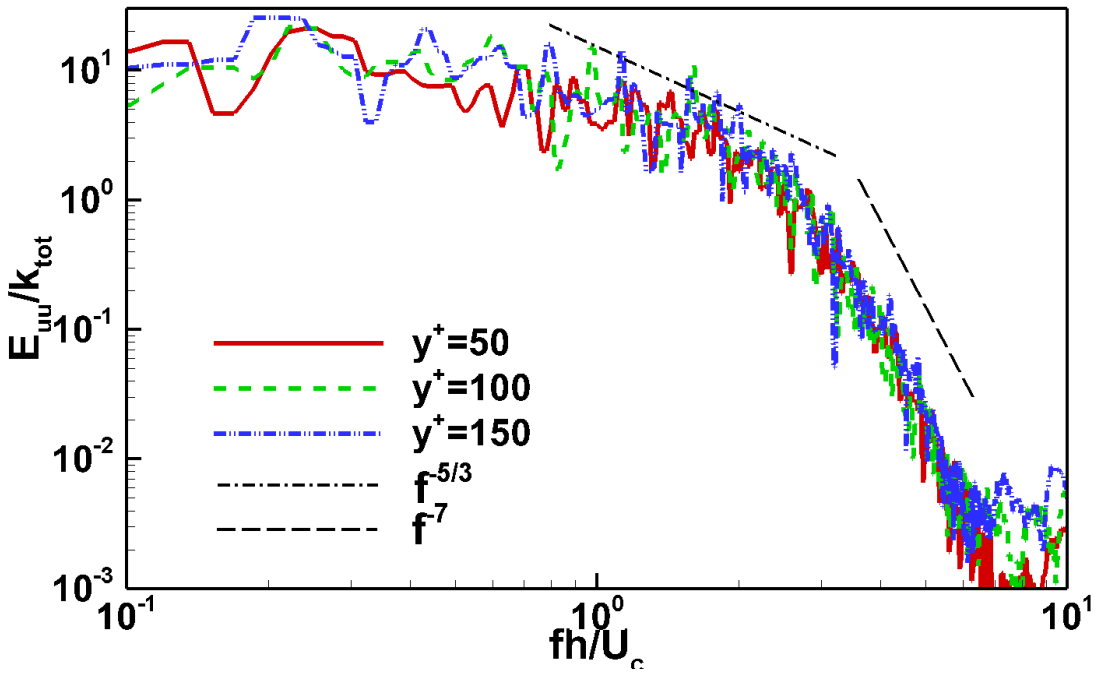

Figure 4.6: One-dimensional frequency spectra of streamwise velocity at three wall distances in Case 4.

Figure 4.8 illustrates λ_2 iso-surfaces, colored by the local streamwise velocity, for Cases 4 and 8. The difference between PANS simulations with modified transport coefficients (Case 4) and unmodified coefficients (Case 8) is immediately evident. The reduced eddy viscosity in the modified case leads to the liberation of broader range of unsteady scale (Case 4). On the other hand, the unmodified case (Case 8) exhibits very few unsteady scales. This finding is consistent with the viscosity ratio exhibited in Figure 4.1. Thus, the modified model leads to prescribed degree of viscosity reduction and captures a wider range of scales. Next, we will establish that the unsteady scales exhibit correct physical behavior.

While Cases 2 to 4 show adequate resolution for capturing one-point statistics, for scrutinizing the details of small-scale vorticity structures we use the highly resolved Case 4 in Figure 4.9. Figure 4.9a provides a three-dimensional illustration of the λ_2 iso-surfaces, colored by the local

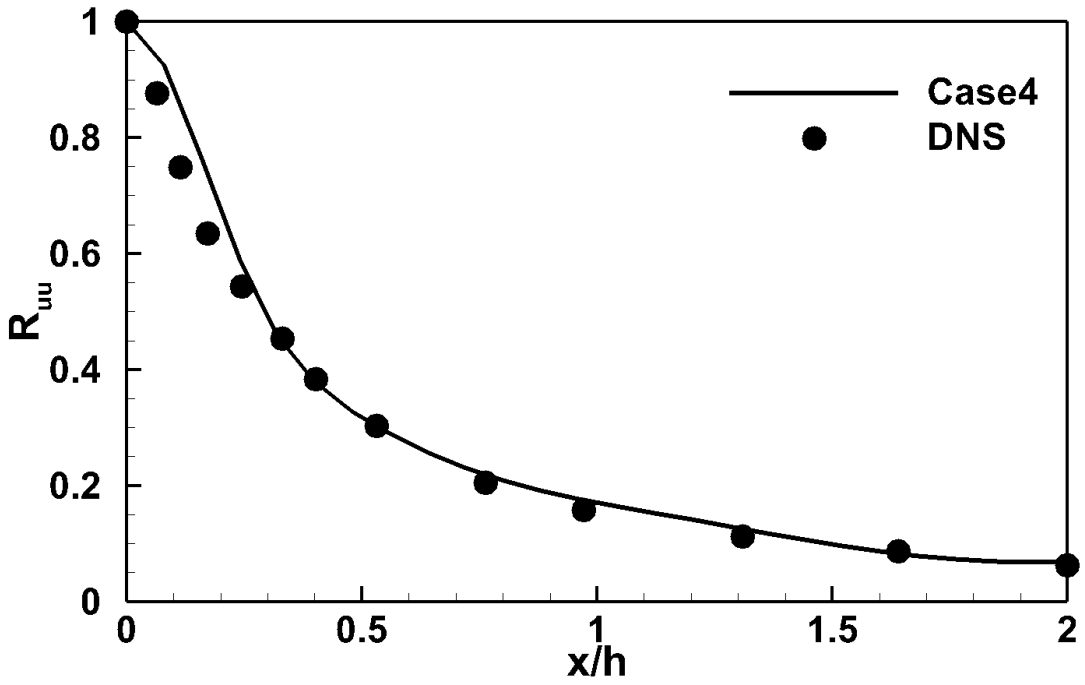

Figure 4.7: Two-point correlations R_{uu} in the streamwise direction at $y^+ = 330$. The DNS data is taken from [3]

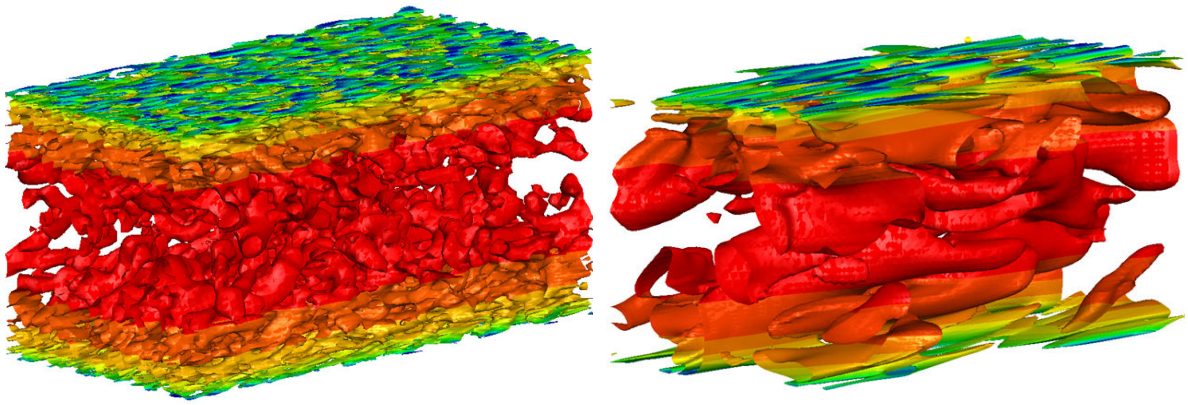

(a) (b)

Figure 4.8: Assessment of the modified transport coefficients in terms of turbulence structures for $Re_\tau = 550$: (a) Case 4, (b) Case8.

streamwise velocity. For a more quantitative examination, we also present the vorticity contours on a streamwise-wall normal plane in Figure 4.9b . From these figures we can identify different sets of organized motions referred to as 'coherent structures'. These structures mostly take the form of hairpin, which is consistent with the observations of Theodorsen (94). Figure 4.9b shows resolved hairpin structures of different forms: symmetric, asymmetric or cane shape. Three distinguishable hairpins, along with some partially formed ones are observed in the figure shown. Since the spanwise component of velocity is non-zero, one-legged hairpins are most prominent. This figure also shows that the grouped hairpins are aligned in a ramp-like shape in the streamwise direction at an angle $\phi = 12.5^{\circ}$. This value of streamwise alignment angle lies in the range of $12^{\circ} < \phi < 20^{\circ}$ established by Christensen and Adrian (48) for fully-developed wall-bounded turbulent flows in this Reynolds number range.

Next we focus on a single packet to examine the flow structure organization using the 'quadrant analysis' (95). Figures 4.9c–4.9e capture ejection and sweep mechanisms on the $x - y$ plane of $z/h = 0.7$, going through the head of hairpins in the packet. By following fluctuation velocity field vectors, this plot depicts how the low-speed near-wall fluid ejects away from the wall and the high-speed outer layer fluid sweeps toward the wall. The shear layer, at which low and high momentum fluids meet is also clearly seen. The head of hairpins, often referred to as the signature of coherent structures, which correspond to strong spanwise vorticity region is also clearly evident. It should be emphasized that Case 7 (with unmodified coefficients) does not capture any of the flow structures at the same degree of computational resolution.

Overall, PANS, with transport equations modified according to EBL analysis, captures the channel flow statistics and flow structures adequately at reasonable computational expense.

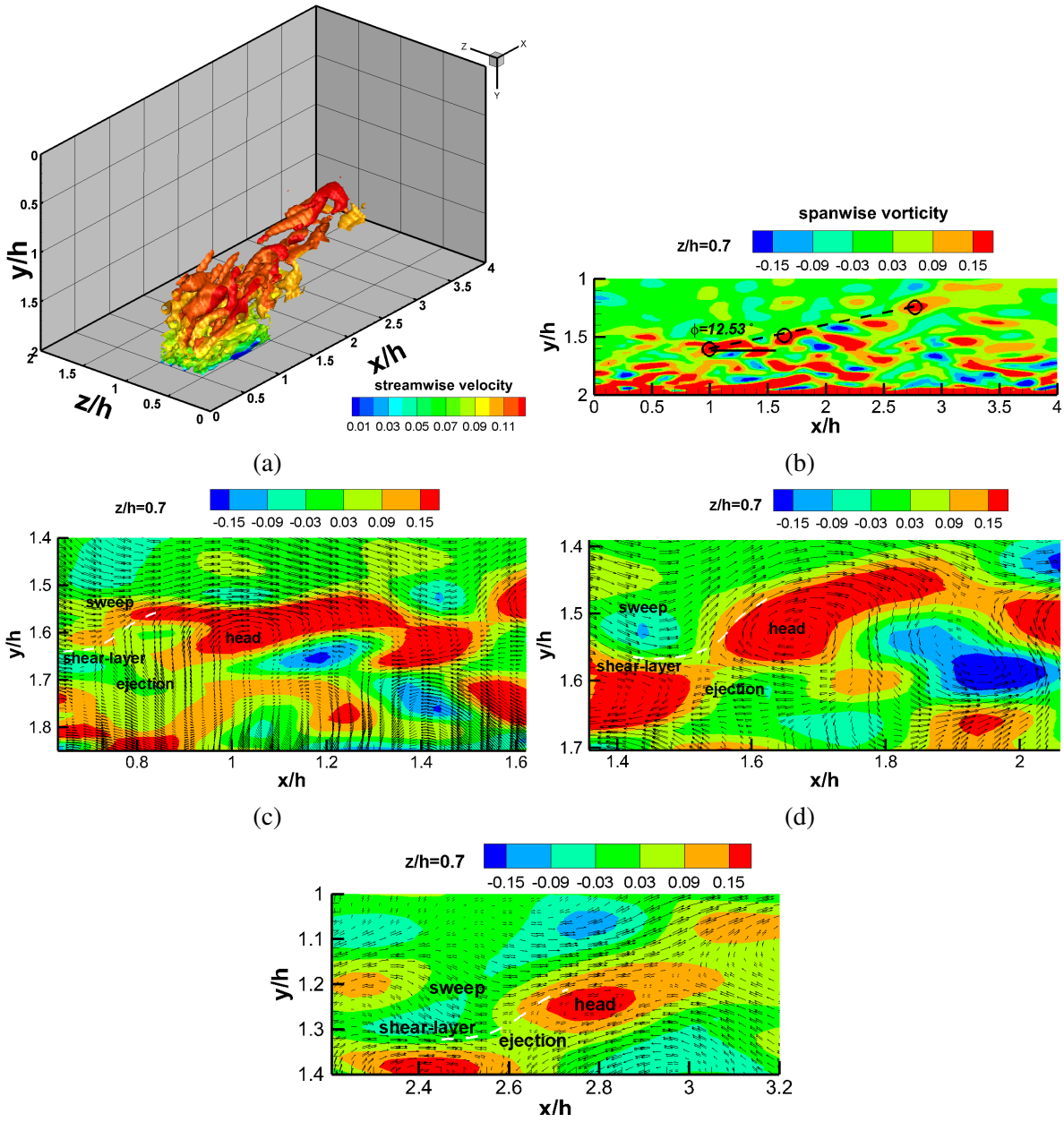

Figure 4.9: Organization of turbulence structures for $Re_\tau = 550$ (a) λ_2 iso-surfaces colored by streamwise velocity, (b) hairpin packet in spanwise vorticity contour, (c) first hairpin, (d) second hairpin, (e) third hairpin.

5. CONSISTENT INFLOW TURBULENCE BOUNDARY CONDITIONS FOR SCALE RESOLVING SIMULATIONS OF SPATIALLY EVOLVING FLOWS

5.1 Introduction

Spatially developing turbulent flows are vital in many engineering applications. These flows are particularly challenging for turbulence closure computations due to the fact that precise prescription of boundary conditions is an absolute necessity. Depending on the nature of turbulence computations, incorrect inflow conditions can lead to a very lengthy development section or, in some cases, a wrong solution. Within the development section, the spurious noises decay and relaxation of error due to poor inflow conditions happens. As the prescription of inflow properties becomes rudimentary, a longer development section is needed to forget the startup transient of convective flows. To reduce the length of development section, further physics have to be incorporated into the perturbed inflow field. Although there have been numerous studies in literature on the specification of perturbed inflow field for LES and DNS (66; 96; 97; 98; 99), there seems to be a lack of attention to inflow field for bridging scale resolving simulation.

One of the differences between partially averaged Navier-Stokes (PANS) model of Girimaji (21) and LES is related to definition of the cut-off wave number. In LES, as the grid resolution increases, the cut-off wave number moves to higher frequencies and eventually coincides with DNS. In PANS, however, the cut-off is dependent on the resolution control parameters. It means that PANS cut-off wave number matches that of DNS if both the computational and physical resolutions approach to DNS. This dictates the necessity of meaningful prescription of unresolved turbulence profiles for the inflow of spatially-evolving PANS simulation.

PANS is a high-fidelity bridging scale-resolving method. The fidelity of PANS model is attributed to its robust and physics based subfilter stress (SFS) modeling. PANS adapts two-equation RANS or Second Moment Closure (SMC) models to account for the subfilter scales residing in the flow field. Hence, the modifications made over the years for the RANS two-equation closures can

be transferred to the PANS subfilter modeling. In PANS, the subfilter length and velocity scales are obtained from the two-equation closure. For generating inflow turbulence, not only scaling of the resolved velocity field is required, but also turbulent kinetic energy and (specific) dissipation must be properly scaled at the inlet. The main objective of the present study is to address how the subfilter turbulence profiles are scaled at the inlet in proportion to the resolved field.

The developed consistent inflow condition for the resolved and unresolved turbulence is examined in a zero-pressure-gradient turbulent boundary layer over a continuous range of momentum thickness Reynolds numbers $650 \leq Re_\theta \leq 1434$. The case is set up in a very cost-effective way in terms of selected boundary conditions and treatment of turbulent flow field. Results show that the synergy between the proposed turbulence generator and partially-averaged Navier-Stokes (PANS) model lead to an efficient spatially developing computation. The cost efficiency of computation is justified through minimizing the length of turbulence development and selectively resolving turbulence structures.

In the results, one-point statistics in terms of the integral quantities, mean flow field, second order moments, skewness and flatness, budgets of kinetic energy along with multi-point physics of structures with respect to two-point correlation and visualization of coherent structures are meticulously studied. Comparing the results with the established experimental, DNS and well-resolved LES data (4; 5; 6; 7; 8), fidelity of PANS in recovering the underlying physics of the turbulent boundary layer flow is assessed.

The structure of this chapter is as follows. First, the derivation of perturbed inflow for PANS is discussed. Then, the computational setup with regard to the domain size, grid resolution, initial field, and boundary conditions is described. Next, the results of turbulent boundary layer, developed from the proposed inflow condition, in terms of one-point and multi-point statistics are reported.

5.2 Perturbed inflow for SRS

5.2.1 Recycling–rescaling of the velocity field

To define the perturbed resolved velocity field at the inlet, recycling/rescaling method (66) is used. In this way, we first average velocity field in time and spanwise direction. Next, the momentum thickness and friction velocity are computed at the recycling station. Friction velocity is iteratively computed at the inlet based on the equilibrium scaling laws to achieve the specified inflow momentum thickness. Then the interpolation of the velocity field in the inner and outer fields, where log-law and defect law hold, is conducted. It is followed by employing a composite formula to yield the rescaled velocity field from the recycling station to the inlet. The Reynolds decomposition of the velocity field reads as:

$$u_i(x, y, z, t) = U_i(x, y) + u_i^{'}(x, y, z, t), \tag{5.1}$$

in which U_i is the averaged velocity in both spanwise direction and time; u_i' is the velocity fluctuations.

For the flow to forget the initial transition to the fully-developed equilibrium state, an efficient approach has been followed (66). The usage of three different time averaging intervals will expedite the transition to fully-developed state. The switch points in time are suggested to be $10\delta/U_\infty$ and $100\delta/U_\infty$. Averaging is respectively conducted during the last $\%1$ and $\%10$ of time segments, and after the second switch, we average velocity in time to the end of simulation:

$$U^{n+1} = \frac{\Delta t}{T} < u_z^{n+1} > +(1 - \frac{\Delta t}{T})U^n, \tag{5.2}$$

the angle bracket denotes spanwise averaging; T is the switching time between time segments; Δt is the averaging interval for each time segment.

Rescaling of the velocity field is conducted through breaking down the field into inner and wake regions. Log-law holds in the inner region, while velocity defect law is valid in the outer

region:

$$\begin{aligned} U^{+^{inner}} &= f(y^+), \\ U^+_\infty - U^{+^{outer}} &= g(\eta), \end{aligned} \tag{5.3}$$

where $U^+ = U/u_\tau$, $u_\tau = (\tau_{wall}/\rho)^{\frac{1}{2}}$, $y^+ = yu_\tau/\nu$, and $\eta = y/\delta$. Functions f and g are respectively based on the log-law and velocity-defect law definitions. τ_{wall} is the wall shear stress; ρ is the fluid density; δ is the boundary layer thickness; y is the wall distance; U_τ is the friction velocity; ν is the kinematic viscosity. After writing these velocity scalings for both recycling and inlet stations, we will have (66):

$$\begin{aligned} U^{inner}_{inlt} &= U_\tau(x_{inlt}) f_1(y^+), \\ U^{inner}_{recy} &= U_\tau(x_{recy}) f_1(y^+), \end{aligned} \tag{5.4}$$

$$\begin{aligned} U^{outer}_{inlt} &= U_\infty - U_\tau(x_{inlt}) g_1(\eta), \\ U^{outer}_{recy} &= U_\infty - U_\tau(x_{recy}) g_1(\eta), \end{aligned} \tag{5.5}$$

The velocity field at the recycling station can be mapped to the inlet by:

$$\begin{aligned} U^{inner}_{inlt} &= \gamma U^{inner}_{recy}(y^+_{inlt}), \\ U^{outer}_{inlt} &= U_\infty(1-\gamma) + \gamma U^{outer}_{recy}(\eta_{inlt}), \end{aligned} \tag{5.6}$$

where $\gamma = U_\tau(x_{inlt})/U_\tau(x_{recy})$. At this step, a linear interpolation of the mean recycling velocity field on the inlet grid spacing is carried out.

The position of reference plane is of critical importance because in case of any correlation with the inlet plane contamination of turbulence statistics will rise (100; 63). The point in choosing the recycling planes is that as the distance between recycling stations increases, the generated inflow will be less realistic and more artificial (γ increases). As such the development section will expand further downstream because of the long lifetimes of the large eddies. Eddy turn-over time provides an estimate on the recovery distance of the inflow (3). Also, care must be taken about the distance to the outlet due to propagation of spurious waves from the outlet plane.

The streamwsie velocity is scaled by the friction velocity, and the wall normal component of velocity is scaled by the free-stream velocity as:

$$\begin{aligned} V_{inlt}^{inner} &= U_\infty f_2(y^+), \\ V_{recy}^{inner} &= U_\infty f_2(y^+), \end{aligned} \tag{5.7}$$

$$\begin{aligned} V_{inlt}^{outer} &= U_\infty g_2(\eta), \\ V_{recy}^{outer} &= U_\infty g_2(\eta), \end{aligned} \tag{5.8}$$

Similar to the streamwise component of velocity, the wall-normal component of velocity at recycling station also has to be interpolated on to the inlet grid spacing. As a result, the mapped vertical velocity field at the inlet would take the form of:

$$\begin{aligned} V_{inlt}^{inner} &= V_{recy}^{inner}(y_{inlt}^+), \\ V_{inlt}^{outer} &= V_{recy}^{outer}(\eta_{inlt}). \end{aligned} \tag{5.9}$$

The mean spanwise velocity is nominally zero in the equilibrium boundary layer. To account for the effect of boundary layer growth in the streamwise direction, Lund *et al.* (66) recommend explicit dependence of fluctuation field on the friction velocity u_τ. The fluctuation field thus takes the following form:

$$\begin{aligned} u_i^{'inner}(x_{inlt}) &= U_\tau(x_{inlt}) f_3(x_{inlt}, y^+, z, t), \\ u_i^{'outer}(x_{inlt}) &= U_\tau(x_{inlt}) g_3(x_{inlt}, \eta, z, t), \end{aligned} \tag{5.10}$$

$$\begin{aligned} u_i^{'inner}(x_{recy}) &= U_\tau(x_{recy}) f_3(x_{recy}, y^+, z, t), \\ u_i^{'outer}(x_{recy}) &= U_\tau(x_{recy}) g_3(x_{recy}, \eta, z, t). \end{aligned} \tag{5.11}$$

Assuming that all the inhomogeneity in the streamwise direction is represented by the friction velocity (66), the scaled perturbed velocity reads as:

$$\begin{aligned} u_i^{'inner}(x_{inlt}) &= \gamma u_i^{'inner}(x_{recy}) f_3(y_{inlt}^+, z, t), \\ u_i^{'outer}(x_{inlt}) &= \gamma u_i^{'outer}(x_{recy}) f_3(\eta_{inlt}, z, t). \end{aligned} \tag{5.12}$$

Now that all the rescaled components are known, the velocity components in the inner and outer regions can be combined together through the weighting function (equation 5.13) to form the inflow velocity field:

$$\begin{aligned} u_i(x_{inlt}) = &[U_i^{inner}(x_{inlt}) + u_i^{'inner}(x_{inlt})][1 - W(\eta_{inlt})] \\ &+[U_i^{outer}(x_{inlt}) + u_i^{'outer}(x_{inlt})]W(\eta_{inlt}), \end{aligned} \tag{5.13}$$

where W is the weighting function defined as (66):

$$W(\eta) = \tfrac{1}{2}[1 + \frac{tanh(\frac{\alpha(\eta-b)}{(1-2b)\eta+b})}{tanh(\alpha)}], \tag{5.14}$$

in which $\alpha = 4$ and $b = 0.2$.

In the process of rescaling velocity field, we need two physical quantities at the inlet and recycling station. In the current work, we chose to specify the momentum thickness at the inlet and to obtain the corresponding friction velocity by (66):

$$u_{\tau,inlt} = u_{\tau,recy}[\frac{\theta_{recy}}{\theta_{inlt}}]^{1/(2(n-1)}; \quad n = 5, \tag{5.15}$$

where θ is the momentum thickness. θ_{recy} and $u_{\tau,recy}$ are directly calculated from the flow field. It is worth noting that the upper bound of momentum thickness integration needs the boundary layer thickness value. Hence, the iterative procedure has to be followed to make sure that the momentum thickness and boundary layer thickness are consistent.

5.2.2 Scaling of turbulence profiles

Numerical treatment of partial differential equations (PDEs) requires specification of meaningful boundary conditions. There are different methods proposed in literature to generate a perturbed inflow velocity field for spatially evolving flows. Lund *et al.* (66), as a case in point, proposed a robust concurrent internally-mapped perturbed inflow velocity field for LES computations. The method is based on recycling/rescaling of velocity field from a proper downstream recycling sta-

tion to the inlet. This study argues that in B-SRS however, not only realistic inflow velocity field is required, but also deterministic prescription of subgrid turbulence quantities, turbulent kinetic energy and (specific) dissipation, for the subfilter closure equations are necessary.

Elucidating the equilibrium states of turbulent flows, fixed-point analysis is known to be a proper way to predict the attracting solutions of turbulence evolution equations (22). In temporal analysis of turbulent flows, e.g. channel flow, the fixed-point of the dynamical system is sensitive to the initial field. While spatial computations need detailed specification of the inflow turbulence properties as they are advected downstream. Hence, for spatially evolving simulations, inflow characteristics dictate the flow dynamics inside the computational domain. In section 5.4, it will be shown that poor inflow condition will lead to the failure of subgrid-scale modeling.

In B-SRS, both the resolved and modeled turbulent kinetic energies contribute toward conserving the total energy of the system. Therefore, it must be ensured that the prescribed level of contribution from each part is maintained throughout the simulation time. Consistency of the physics with the prescribed resolution control parameter f_k is a criterion, revealing the functionality of B-SRS (1).

In an attempt to control the level of unresolved unsteadiness in B-SRS, meaningful prescription of the modeled turbulence (k_u and ω_u) profiles at the inlet of spatially evolving simulations is necessary. Instantaneous modeled turbulence properties at the inlet must be consistent with the prescribed physical resolution, f_k. In order to control the ratio between the resolved and unresolved turbulent kinetic energies at the inlet, the modeled part is expressed as a function of the resolution control parameter f_k:

$$k_u(y) = \frac{f_k}{1 - f_k} k_r(y) \quad ; \quad k_r(y) = \overline{V_i V_i} - \bar{V}_i \bar{V}_i. \tag{5.16}$$

Excessive dissipation of turbulence in the unresolved part would lead to destruction of the modeled turbulent kinetic energy. Hence, the level of modeled (specific) dissipation has to be defined based on the underlying physics within subfilter scales such that the intended level of

modeled kinetic energy survives. According to the 'equilibrium analysis' within the logarithmic layer, the production of unresolved turbulent kinetic energy is balanced with its dissipation:

$$P_u \approx \epsilon_u. \tag{5.17}$$

The unresolved production term is calculated from:

$$P_u = 2\nu_u \overline{S_{ij} S_{ij}}, \tag{5.18}$$

in which

$$\nu_u = c_\mu \frac{k_u^2}{\epsilon_u}. \tag{5.19}$$

Upon substitution of ν_u from equation (5.19) into equation (5.18), the scaled inflow dissipation rate is given by

$$\epsilon_u = \sqrt{2 c_\mu k_u^2 \overline{S_{ij} S_{ij}}}, \tag{5.20}$$

ω_u in turn can be extracted from ϵ_u through:

$$\epsilon_u = \beta^* k_u \omega_u. \tag{5.21}$$

Finally, the scaled specific dissipation rate at the inlet is expressed as:

$$\omega_u = \frac{\sqrt{2 c_\mu \overline{S_{ij} S_{ij}}}}{\beta^*}, \tag{5.22}$$

where $\beta^* = 0.09$; and $c_\mu = 0.09$. In the remainder of this work, we perform PANS simulation of zero- pressure-gradient turbulent boundary layer to verify and validate the proposed consistent inflow properties. Although the scaling development in this study is in the context of PANS, the established framework is applicable to other bridging scale-resolving methods.

5.3 Simulation procedure

5.3.1 Computational setup

In order to investigate the performance of the proposed inflow properties, we conduct PANS simulation of a spatially evolving flat-plate boundary layer with a momentum thickness Reynolds number in the range $650 \leq Re_\theta \leq 1434$. Simulations are conducted over a range of numerical and physical resolutions listed in Table 5.1. The dimensions of the computational domain are $53\delta_0 \times 4\delta_0 \times 4.5\delta_0$ in the streamwise, wall-normal and spanwise directions, with δ_0 being the inflow boundary layer thickness (Figure 5.1). These dimensions are examined in the results section in terms of covering the largest energy containing eddies present in the flow field.

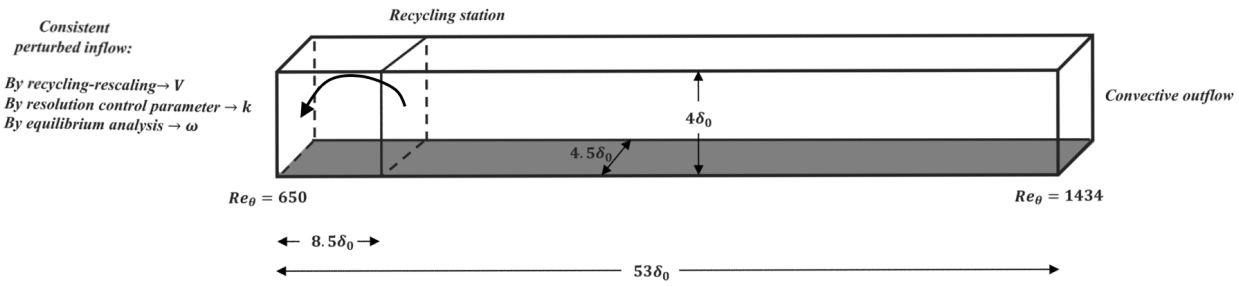

Figure 5.1: Three-dimensional schematic of the computational domain for PANS of ZPGFPBL.

Table 5.1: Details of the test cases examined for the turbulent boundary layer.

Simulation	N_x	N_y	N_z	N	f_k	Δx^+	Δy^+_{min}	Δz^+
CaseA-1	503	55	55	1.5M	0.1	33.6	0.92	17.2
CaseA-2	503	55	64	1.7M	0.1	33.6	0.92	14.5
CaseA-3	503	60	64	1.9M	0.1	33.6	0.84	14.5
CaseA-4	503	64	60	1.9M	0.1	33.6	0.77	15.5
CaseB-1	503	55	55	1.5M	0.2	33.6	0.92	17.2
CaseB-2	503	55	64	1.7M	0.2	33.6	0.92	14.5
CaseB-3	503	60	64	1.9M	0.2	33.6	0.84	14.5
CaseB-4	503	64	60	1.9M	0.2	33.6	0.77	15.5

As shown in Figure 5.1, the recycling plane is located at $x_{rec} = 8.5\delta_0$ downstream of the inlet. This choice is made based on two considerations. In case of any turbulence correlation between the recycling planes, contamination of statistics will arise (100; 63). On the other hand, as the distance between the recycling stations increases, the scaling factor grows and the generated inflow in turn will be less realistic.

The accuracy-on-demand reasoning makes the computational cost of PANS simulations dependent on the objective functions (1). Convergence of statistics using different numerical and physical resolutions is verified in Table 5.1. In this table, the grid spacing is normalized by the viscous wall units at the inflow friction velocity. The free stream velocity and kinematic viscosity are set to $U_\infty = 1(m/s)$ and $\nu = 10^{-5}(m^2/s)$, respectively. The grid spacing is uniform in the streamwise and spanwise directions. The essence of boundary layers dictates grid clustering in the near-wall region. The distribution of grid points in the wall-normal direction is such that there are 8 grid points within $0 < y^+ < 10$ and 22 grid points between $10 < y^+ < 100$. After comparing the computational resolution of PANS in Table 5.1 with the established DNS and LES computations in Table 5.2, one would notice a fair amount of computational cost saving.

Table 5.2: Computational cost of boundary layer simulations compared to the reference works.

Reference	Method	Re_θ	Number of grid points
Spalart (4)	DNS; spectral	1410	11 million
Wu and Moin (5)	DNS; finite difference	$80 \leq Re_\theta \leq 940$	210 million
Schlatter *et al.* (8)	LES; spectral	$180 \leq Re_\theta \leq 4300$	605 million
Simens *et al.* (63)	DNS; finite difference	$600 \leq Re_\theta \leq 950$	128 million

5.3.2 Initial condition

In the recycling/rescaling of the resolved velocity field, the recycling station has to be in an equilibrium condition to be valid for rescaling purposes (66). In the current work, the initial turbulent velocity field is represented by the Spalding law, which is a power-series fit of the laminar,

buffer and logarithmic regions of an equilibrium boundary layer (101):

$$y^+ = u^+ + \frac{1}{E}[e^{\kappa u^+} - 1 - \kappa u^+ - \frac{(\kappa u^+)^2}{2} - \frac{(\kappa u^+)^3}{6}], \tag{5.23}$$

where $\kappa = 0.42$, $E = 9.1$, $y^+ = yu_\tau/\nu$ and $u^+ = \bar{u}/u_\tau$; u_τ denotes the friction velocity. To expedite the development of turbulence from the base flow, the initial velocity field is superimposed with the spanwise sinusoidal waviness (102):

$$u_3'(x^+, y^+) = c_\epsilon sin(a^+ x^+) y^+ exp(-c_\sigma y^{+2}), \tag{5.24}$$

where c_ϵ is the linear perturbation amplitude, a^+ is the wavenumber of perturbation in the x-direction and c_σ is the transverse decay.

5.3.3 Boundary conditions

In order to mimic the viscous flow over a flat plate, the no-slip condition is applied on the wall. The free-slip condition for the velocity field, along with constant zero pressure condition represent the free-stream condition:

$$\frac{\partial v}{\partial y} = 0; \quad \frac{\partial u}{\partial y} = 0; \quad p_\infty(x) = constant. \tag{5.25}$$

Assuming the flow is homogeneous in the spanwise direction, the cyclic condition holds in the statistical sense. We employ the Dirichlet boundary conditions for the subgrid turbulence properties (k and ω) on the wall. The inflow turbulence properties are defined using the proposed inflow condition described in Section 5.2.2. A constant zero pressure is defined at the outlet plane. Disturbances generated at the outlet can potentially change the flow behavior throughout the flow domain. Therefore, in order to minimize the reflection of waves from the outlet boundary into the interior domain, a smooth convection of flow structures through the outlet plane has to be established. Over the outflow boundary, a relatively undistorted traveling vortex is fulfilled by the

convective boundary condition (103; 104):

$$\frac{\partial u}{\partial t} + U_{conv}\frac{\partial u}{\partial x} = 0, \tag{5.26}$$

where U_{conv} is the mean convective velocity. At each time step, U_{conv} is updated so that the conservation of mass flux throughout the whole domain is satisfied (105).

5.3.4 Accuracy of solver

Our in-house OpenFOAM-based simulator is used to integrate the evolution equations using the finite volume approach. The proposed inflow condition has been implemented as a new library in OpenFOAM. The employed transient solver is the so-called *pimpleFOAM*. Spatial and temporal derivatives are respectively approximated by the second-order accurate central differencing and Crank-Nicolson schemes (Δ_x^2 and Δ_t^2). The level of numerical stability is controlled by prescribing a tight criteria on the maximum CFL number value at each time-step ($CFL < 0.8$).

5.4 Results and discussion

In the results, first we ensure the functionality of the scale-resolving computations. Next, the single-point statistics are compared against the established DNS data. Finally, we discuss the analysis of two-point correlation properties and visualization of turbulence structures.

5.4.1 Internal consistency

The physics of the turbulence bridging models is described by three evolution equations; momentum equation (U), subfilter turbulent kinetic energy (k_u), and subfilter specific dissipation rate (ω_u). Herein it is ensured that the equations are solved in the right way via implementation of a meaningful inflow for the ZPGFPBL. The prescribed reduction of eddy viscosity, especially in the near-wall region, defines the functionality of the bridging subfilter closure modeling. In this subsection, we attempt to establish that the scaling of turbulent quantities at the inlet is prerequisite for consistency of the PANS results with the prescribed resolution control parameter (f_k). In PANS, to ensure that the correct level of unsteadiness based on the prescribed control parameter

is captured in the simulation, the internal consistency study is critical (1). According to the definition, the DNS solution will be recovered as f_k asymptotes to zero. PANS results of ZPGFPBL reveal that the trivial fixed-point, corresponding to $k_u \approx 0$, will be permitted for a system with ill-defined boundaries. From Figure 5.2, either small values of turbulent kinetic energy or excessive amount of dissipation rate at the inlet could make a B-SRS computation asymptote to the trivial DNS solution.

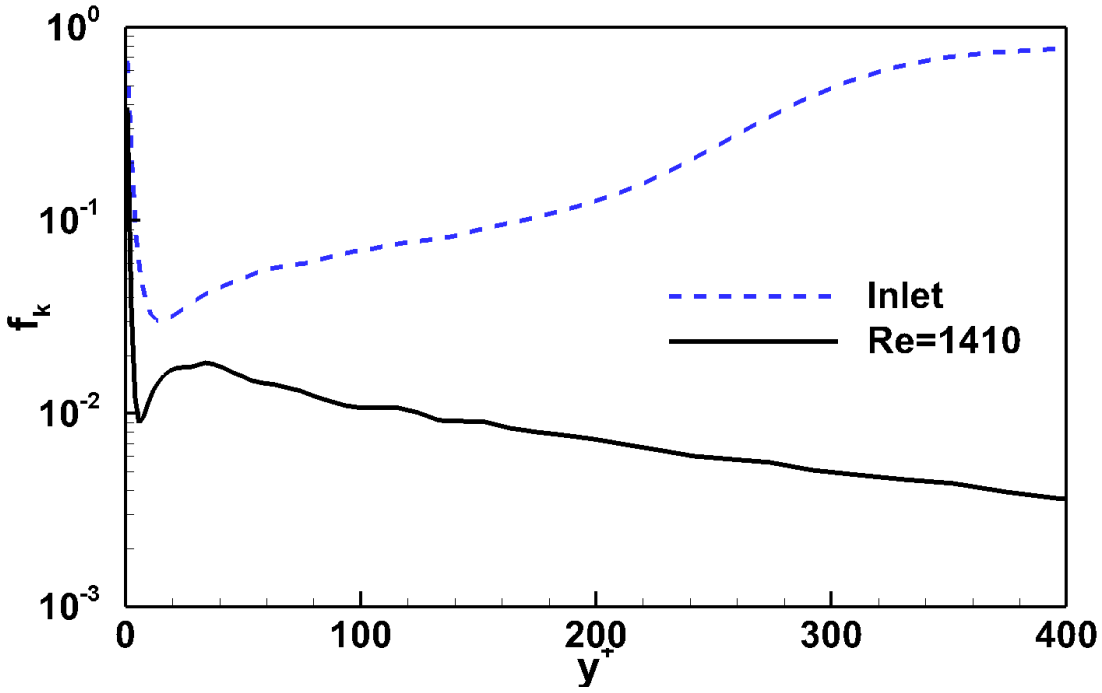

Figure 5.2: Posteriori f_k calculation associated with unscaled quantities for CaseA-3.

Figure 5.3 shows that the consistency of the eddy viscosity reduction with the prescribed value is contingent upon the right scaling of k_u and ω_u at the inlet. In spatially evolving simulations, first the recovery of correct physical resolution (f_k) is ensured at the inlet (Figures 5.3a-b), then for the rest of flow field, the system evolves such that the flow dynamics converge to the correct PANS solution (Figures 5.3c-d).

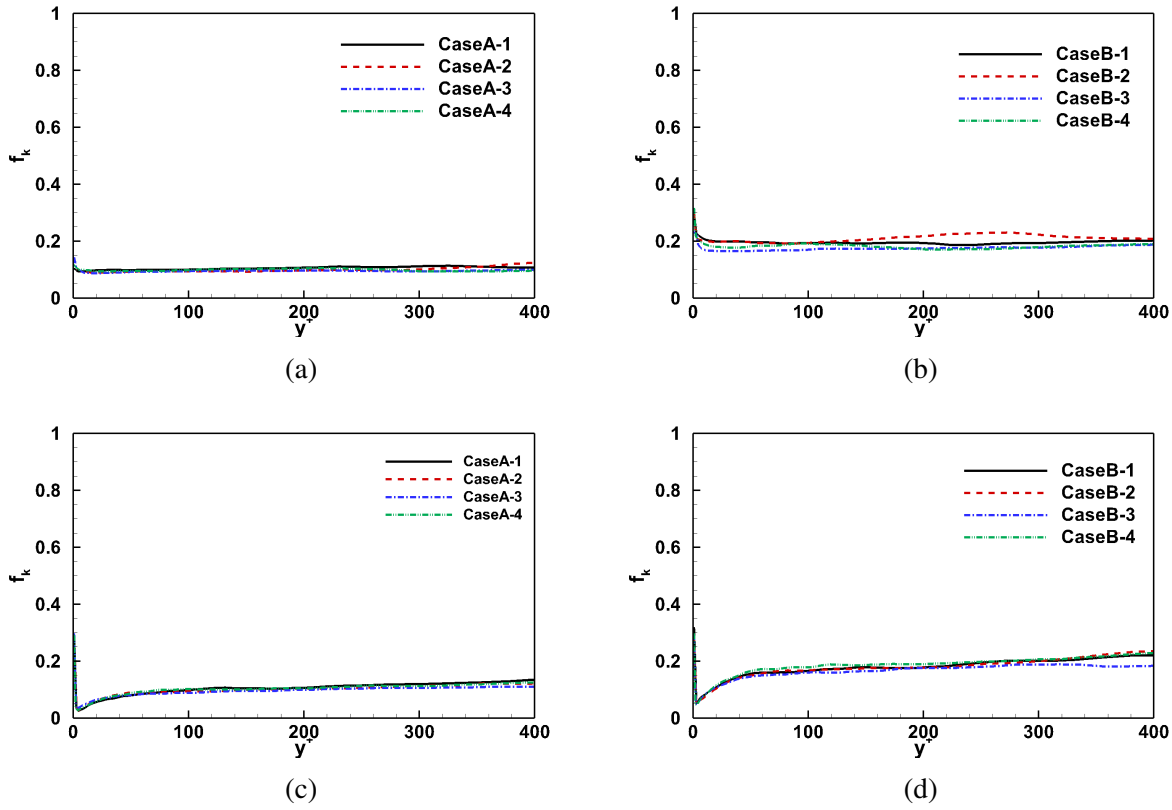

Figure 5.3: f_k consistency for (a) $f_k = 0.1$ at inlet, (b) $f_k = 0.2$ at inlet, (c) $f_k = 0.1$ at $Re_\theta = 1410$, (d) $f_k = 0.2$ at $Re_\theta = 1410$.

5.4.2 Integral quantities

According to Figure 5.4, evolution of the skin friction coefficient (c_f) and shape factor (H) are validated using the DNS data of Spalart (4) and Wu and Moin (5). Shape factor (H), representing the ratio of displacement to momentum thickness, manifests the nature of the flow. The fully developed turbulence is clearly visible as the shape factor settles to the constant value of 1.4, reported for fully-developed turbulent boundary layers (4; 5). The captured autogeneration of near-wall vortical structures, shown later, leads to recovering turbulent stresses and subsequent drag production.

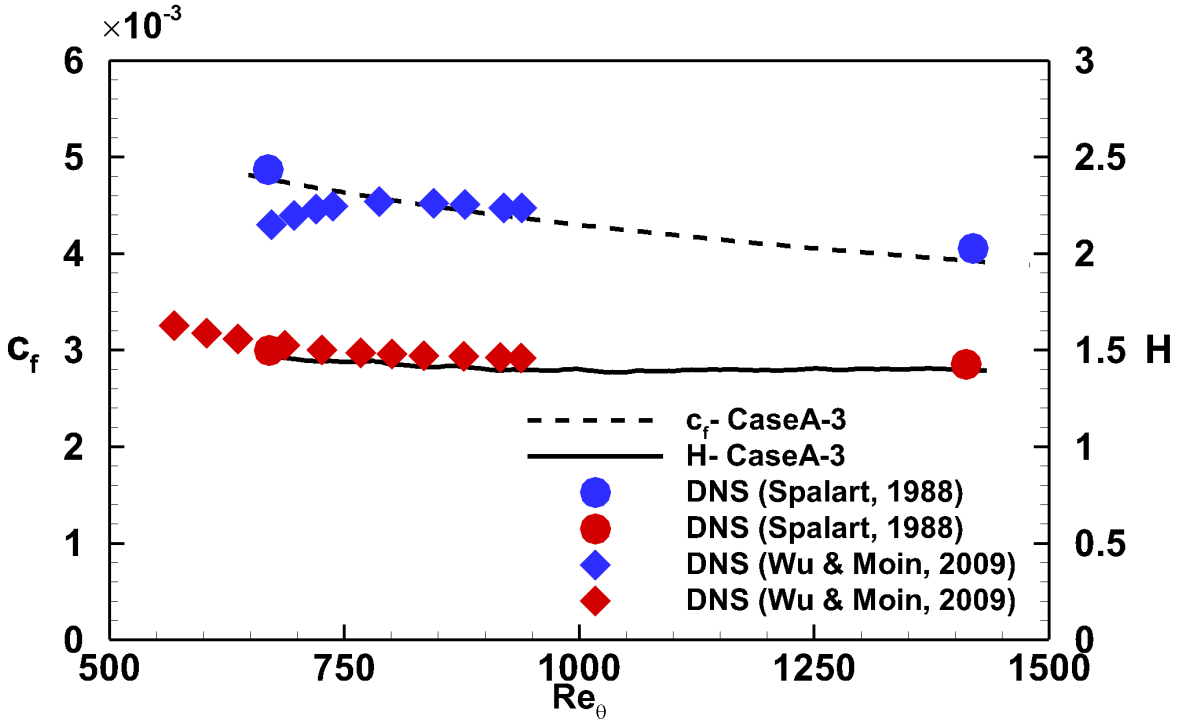

Figure 5.4: Stream-parallel evolution of friction coefficient and shape factor for CaseA-3 compared to the DNS data from [4] and [5].

5.4.3 One-point statistics

In this subsection, the one-point statistics up to the fourth-order central moment of velocity field fluctuations are examined. The results are normalized by the local friction velocity ($u_\tau \equiv \sqrt{\tau_w/\rho}$) and viscous length scale ($l_\nu \equiv \nu/u_\tau$). τ_w and ρ are the wall shear stress and fluid density, respectively.

5.4.3.1 Velocity field

In SRS computations, in order to avoid log-layer mismatch, either a robust subfilter modeling or a proper physical resolution is needed. Having adapted the well-established RANS reasoning into the subfilter closure(1), the log-law profile can be reproduced with coarser grid resolutions compared to other B-SRS (1). Figures 5.5a and 5.5b respectively show the grid convergence study for $f_k = 0.1$, and $f_k = 0.2$ for different cases listed in Table 5.1. As is evident, both sets of data

are in agreement with the DNS of Spalart (4) at $Re_\theta = 1410$. Although there is a little deviation in the logarithmic region for $f_k = 0.2$ due to a lower liberated unsteadiness.

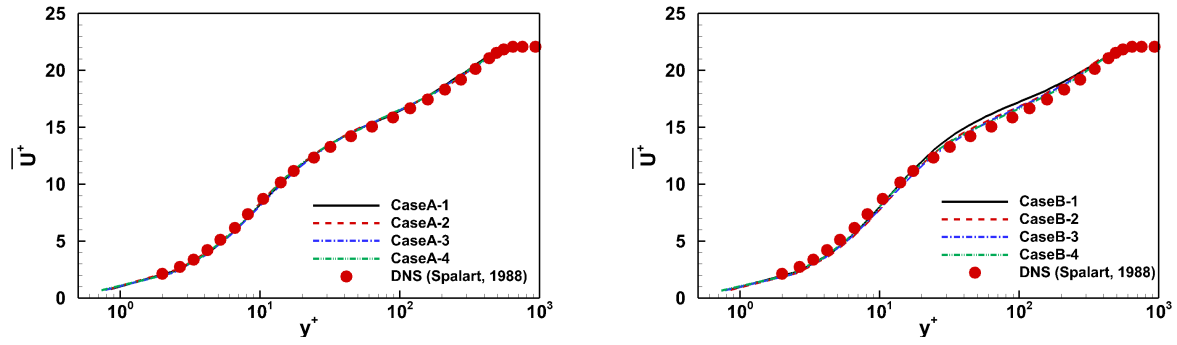

(a) (b)

Figure 5.5: Log-law profile at $Re_\theta = 1410$ as a function of grid resolution with (a) $f_k = 0.1$, (b) $f_k = 0.2$.

5.4.3.2 Stress profiles

Figures 5.6a and 5.6b respectively show the second order moments of velocity field as a function of both inner (y^+) and outer (y/δ) wall-normal coordinates at $Re_\theta = 1410$. All the second order turbulence statistics agree well with the DNS of Spalart (4). In Figure 5.6a, the peak of streamwise normal stress is located at $y^+ = 13$, which agrees well with DNS. In addition, for $y^+ < 4$, zero shear stress implies a zero velocity gradient. The anisotropy of the flow in the near wall region is clear from the stress profiles in the inner-wall coordinate (Figure 5.6a), while they all settle to the same value in the outer wall region (Figure 5.6b). PANS can capture the near-wall anisotropy, provided that an adequate level of unsteadiness is resolved (1). In Figure 5.6b, the shear stress profile shows an overshoot at $y/\delta = 0.07$ after which it asymptotes to zero in the outer wall region.

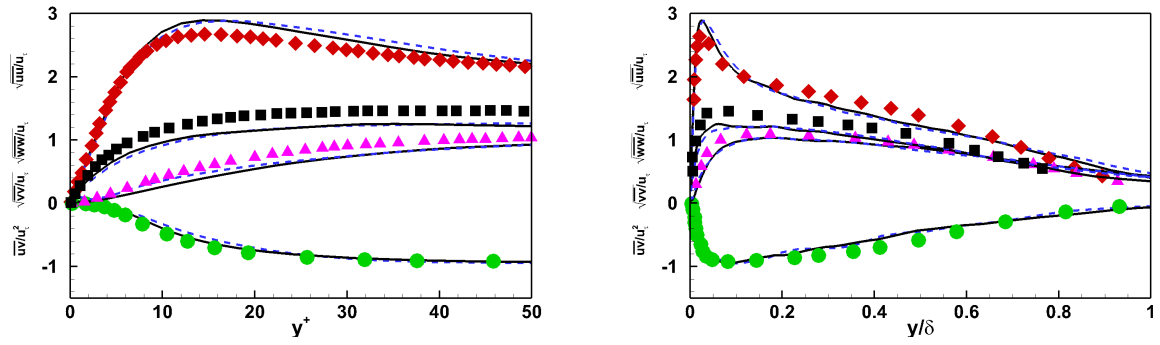

(a) (b)

Figure 5.6: Second moments of turbulence at $Re_\theta = 1410$ as a function of (a) inner wall coordinate (y^+); (b) outer coordinate (y/δ). Solid line and dashed line respectively correspond to CaseA-1 and CaseB-1. The DNS data is taken from [4]. Diamond, streamwise stress; square, spanwise stress; triangle, wall-normal stress; circle, shear stress.

5.4.3.3 Skewness and flatness

High-order statistics in terms of skewness (S) and flatness (F) of streamwise velocity fluctuations are defined as:

$$S(u') = \frac{\overline{u'^3}}{\overline{u'^2}^{3/2}} \quad ; \quad F(u') = \frac{\overline{u'^4}}{\overline{u'^2}^2}. \tag{5.27}$$

Figure 5.7 compares the skewness and flatness of streamwise velocity fluctuations with the experimental data of Barlow and Johnston (6) for $Re_\theta = 1140$. Quantitative analysis of sweep and ejection mechanisms is manifested in the skewness of streamwise fluctuation. According to Figure 5.7a, in PANS $y^+ \approx 19$ separates the events which are dominant in the second and fourth quadrant of the $u' - v'$ plane (50). The corresponding value is $y^+ = 14$ for the experiment of Barlow and Johnston (6). The maximum flatness associated with the intermittent near-wall behavior is also depicted in the flatness of streamwise fluctuations (Figure 5.7b).

5.4.4 Budgets of kinetic energy

Production (P_k) and viscous dissipation (ϵ_k) of turbulent kinetic energy are expressed as:

$$P_k = -\overline{u_i' u_j'} \frac{\partial U_i}{\partial x_i}; \quad \epsilon_k = \nu \overline{\frac{\partial u_i'}{\partial x_j} \frac{\partial u_i'}{\partial x_j}}. \tag{5.28}$$

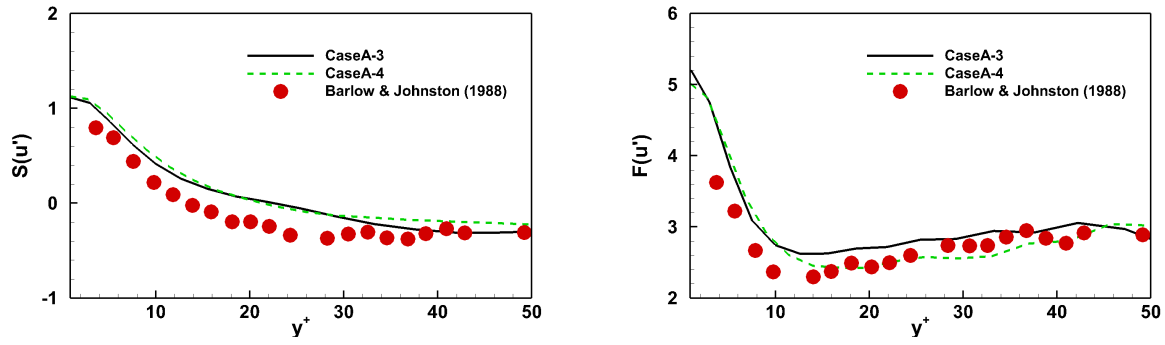

(a) (b)

Figure 5.7: (a) Skewness and (b) flatness of streamwise fluctuating velocity at $Re_\theta = 1140$. The experimental data is adapted from [6].

Figure 5.8 shows the turbulent kinetic energy budgets, normalized by ${u_\tau}^4/\nu$, for the near-wall

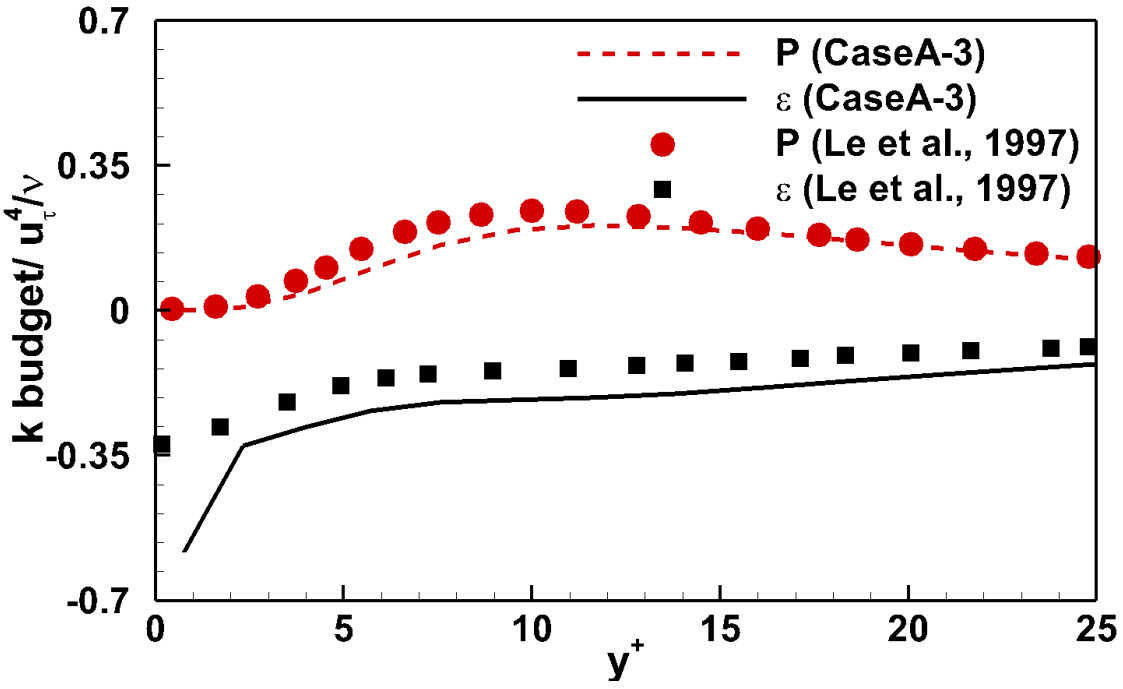

Figure 5.8: Turbulent kinetic energy budget compared to DNS of [7].

region. Being dimensionless based on the local friction velocity (u_τ), the budget holds for every downstream station along the plate. According to Figure 5.8 the computed budgets of energy is in agreement with the DNS of Le *et al.* (7). Since the low-Reynolds-number effects are not included in the subfilter stress modeling, the observed discrepancy in the dissipation term compared to DNS is expected near the wall.

5.4.5 Two-point correlation

The spanwise two-point correlation of different velocity fluctuations is expressed as (106):

$$R_{u_i u_j}(\mathbf{z}, t) = \frac{\overline{u_i'(\mathbf{z}, t) u_j'(\mathbf{z} + \mathbf{dz}, t)}}{\sqrt{\overline{u_i'^2}\,\overline{u_j'^2}}}. \tag{5.29}$$

Although the subfilter scale modeling is based on the single-point physics, the fidelity of PANS

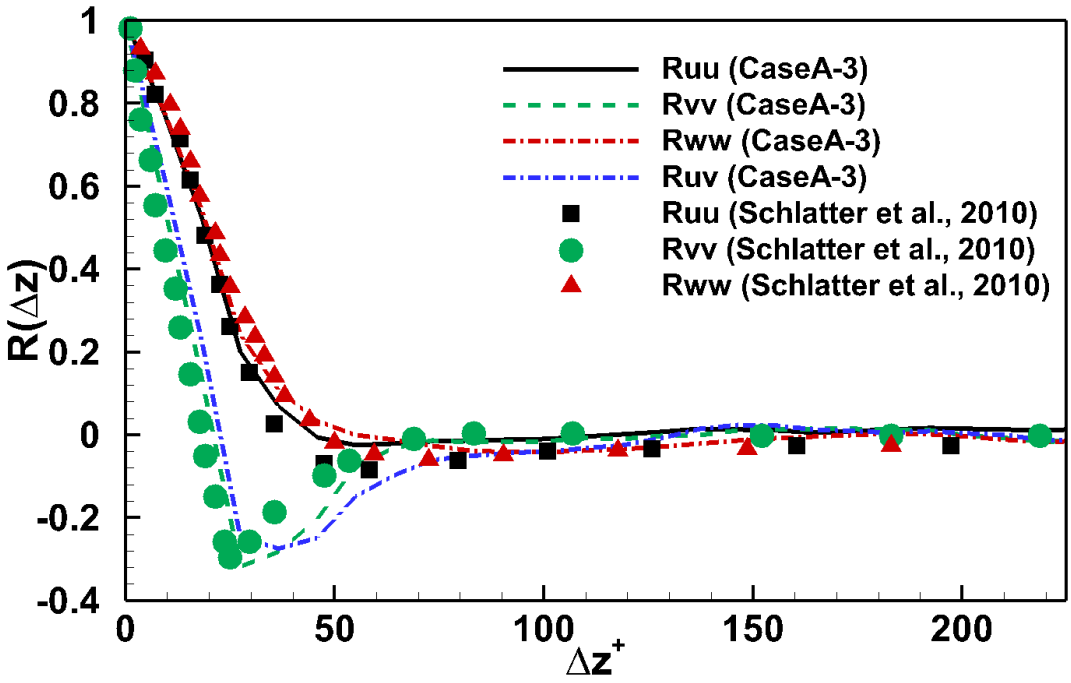

Figure 5.9: Spanwise two-point correlation of velocity field at $y^+ \approx 8$ for $Re_\theta = 1410$. Well-resolved LES data corresponds to $Re_\theta = 1430$ from [8].

in capturing multi-point physics originates from the fact that a proper level of unsteadiness is resolved. To gain insight into the boundary layer flow dynamics in the near-wall region, examination of multi-point physics of boundary layer is conducted. Multi-point physics in terms of spanwise two-point correlation of velocity field is shown in Figure 5.9. According to this figure, the two-point correlation of all components of fluctuating velocity field in the spanwise direction asymptotes to zero, emphasizing the fact that the flow statistics have not been affected by the spanwise periodicity. Cross-correlation of turbulent flux (R_{uv}) between streamwise and wall normal components have also been shown in Figure 5.9. Based on the definition, if the separation exceeds the size of the largest eddies in one direction, the value of two-point correlation asymptotes to zero as decorrelation of scales is achieved. The organization of structures can be implied from the two-point correlation plot (Figure 5.9). The minimum of spanwise two-point correlation of

Table 5.3: Organization of structures in the near-wall region of boundary layer.

Quantity	Feature	PANS	LES (8)
R_{uu}^{min}	Spacing	50	50
R_{vv}^{min}	diameter	25	25
R_{ww}^{min}	Vortex-pairing	50	50

streamwise component of velocity corresponds to the spanwise separation of high and low speed streaks ($\Delta z^+ = 50$). Furthermore, since negative correlation value shows that the two points are of different signs, we can interpret the minimum of R_{uu} as the distance between neighboring streaks in the spanwise direction. In the same figure, the spacing between counter-rotating streamwise vortices is approximated by the extrema of R_{ww} at $\Delta z^+ = 50$. The two-point correlation of the wall-normal turbulent velocity field, R_{vv}, shows a minimum at $\Delta z^+ \approx 25$, representing the diameter of streamwise vorticities at $y^+ = 8$. These values are in agreement with the counterpart well-resolved LES values reported by Schlatter *et al.* (8) (Table 5.3). A fast decay of spanwise correlation of the wall-normal velocity reveals the fact that the correlation length for that component

is very small compared to stream parallel and spanwise components of velocity. It is apparent that the zero crossing of normal velocity is earlier than the other components.

5.4.6 Turbulence structures

Figure 5.10 shows the scaled instantaneous streamwise velocity field ($U_x^* = U_x/U_\infty$) in PANS simulation of ZPGFPBL at $y^+ = 5$, depicting 'footprint' of coherent structures on the wall. The anisotropic near-wall structures are clear in the form of streamwise streaks. Alternating high and low momentum near-wall streaks are a source of Reynolds shear stress production. The high momentum regions correspond to legs of hairpin, surrounding low momentum regions in between.

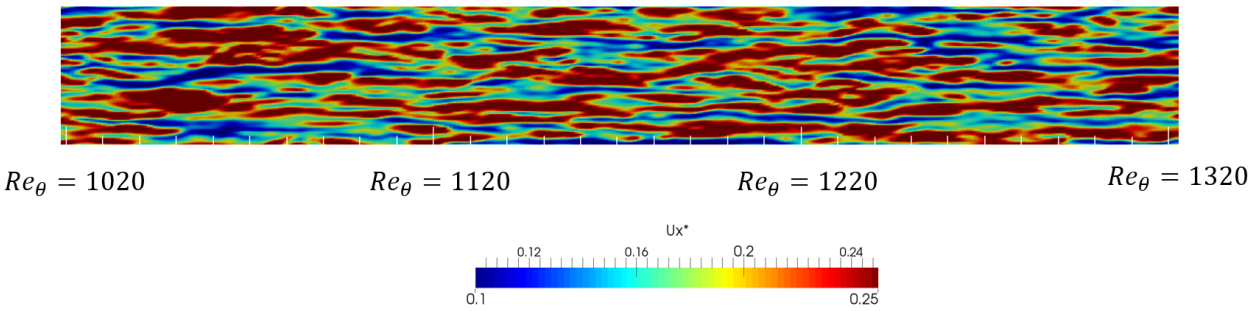

Figure 5.10: Alternating high and low-speed streaks on xz plane visualized by instantaneous U_x^* at $y^+ \approx 5$ for CaseA-3.

Capability of PANS in capturing the momentum transport mechanisms in the near-wall region is also investigated through visualization of near-wall coherent structures using the so-called Q criteria (107). Q is the second invariant of the velocity gradient tensor, expressed as $Q = -\frac{1}{2}(S_{ij}Sij - \Omega_{ij}\Omega_{ij})$. According to this criteria, the positive values of Q correspond to the spots at which the rotation rate dominates over the strain rate. Q iso-surfaces for CaseA-3 and CaseB-3 are shown in Figure 5.11. This figure shows that for the same Q magnitude ($Q = 70$), $f_k = 0.1$ resolves more near-wall turbulence structures compared to $f_k = 0.2$ as a result of survival of more unsteadiness. Although on the left side of Figure 5.11, it is clear that Case3-B still resolves large coherent structures in the form of hairpin vortices.

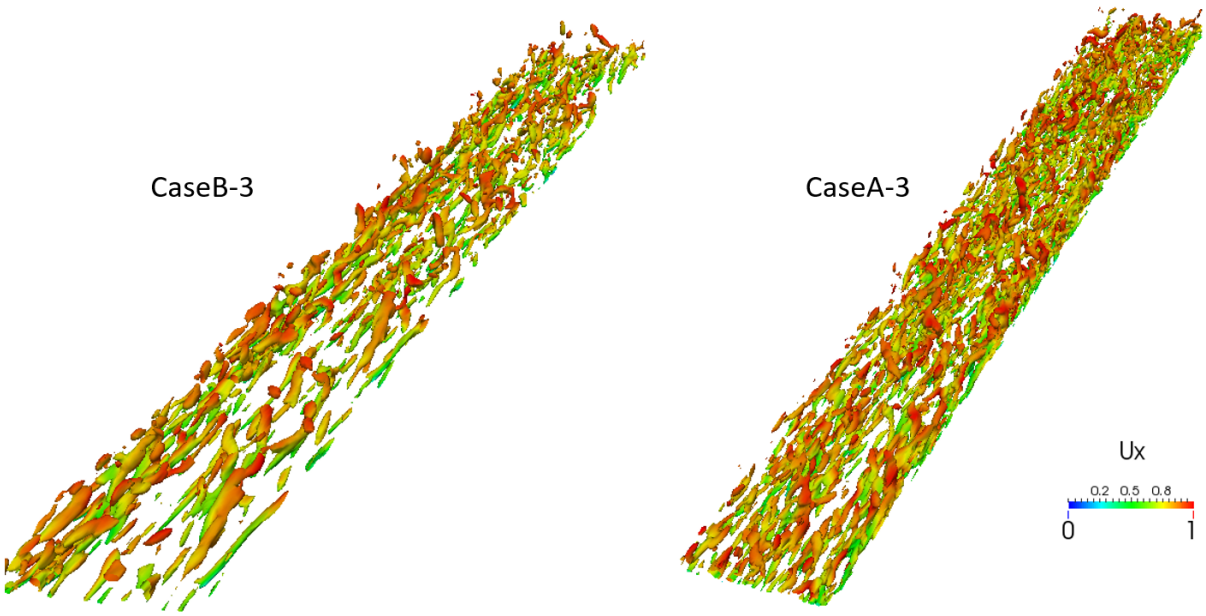

Figure 5.11: Iso-surfaces of second invariant of the velocity gradient tensor by $Q = 70$ colored by the instantaneous streamwise velocity.

6. SIMULATION OF LAMINAR-TO-TURBULENT K-TYPE TRANSITION

6.1 Introduction

Identification of transition point is of importance in the turbulence related engineering problems, e.g. heat transfer and shear stress. Application of transition from laminar-to-turbulent is twofold. Low drag in the laminar regime and delayed separation in the turbulent regime make each flow regime attractive in specific applications. Hence, the controlled transition has long been of critical importance to turbulence researchers. In wall-bounded shear flows, Tollmien-Schlichting (T-S) waves, identified as the most unstable modes of Orr-Sommerfeld equations, are the primary instability mechanism of transitioning from laminar-to-turbulent. This type of instability can be studied in either temporal or spatial approach. Scientists have been facing challenges in spatially transition simulations as to being computationally demanding. In this way, reproducing the underlying physics using affordable scale-resolving simulations deserves a critical attention.

Morkovin *et al.* (9) argues that transition in external flows is a product of progression of stages shown in Figure 6.1. Depending on the power of excitation, transition from the laminar to turbulent regimes falls into one of the two main categories: bypass transition and natural transition. In the former, the linear growth of disturbances is bypassed due to a strong excitation of the unstable modes. In the latter, however, the laminar to turbulent transition is a result of sequence of instabilities. In the natural transition, the receptivity mechanism e.g. periodic blowing/suction waves, is followed by primary instability, set in as two or three-dimensional T-S waves. Secondary instabilities and formation of Λ vortices are the results of large growth rate of disturbances (108). Concentrated shear layers, shown in the results section, develop tertiary instabilities which are responsible for the formation of turbulent spots in the post-transition region. Later, these spots will develop and merge into fully-developed turbulence. klebanoff and his colleagues (109; 110) were firsts who identified the 'tertiary' instabilities, responsible for the laminar breakdown and subsequent emergence of turbulent fluctuations. In a transition scenario, the interaction of disturbances

from different paths, shown in Figure 6.1, will add to the complexity of transitional flow physics and its analysis.

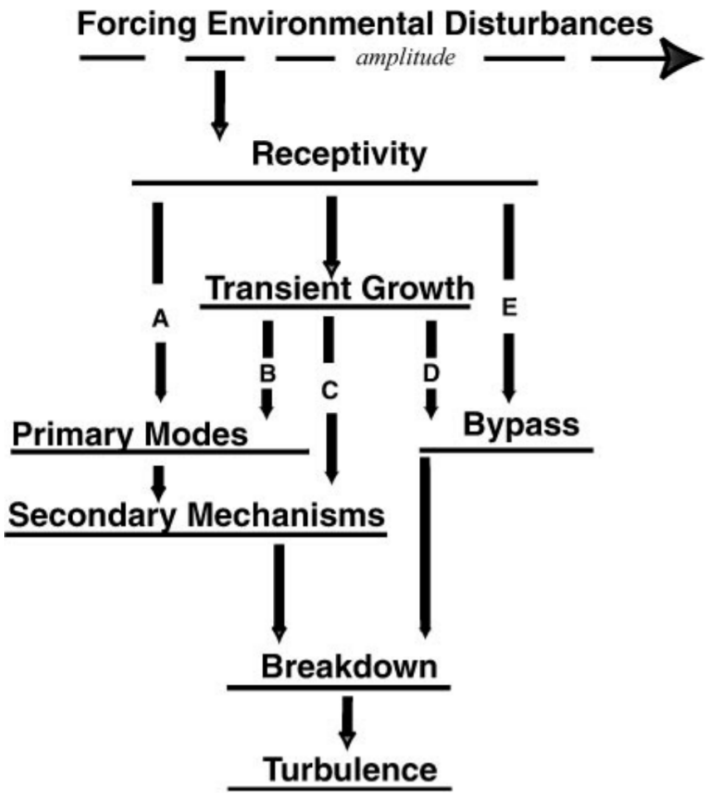

Figure 6.1: The Roadmaps from receptivity to turbulence for external flows [9].

The 'non-parallel effects' are the essence of studying natural transition from laminar-to-turbulent regime (111). Schubauer and Skramstad (68) were the first who argued that the temporal analysis is not able to account for the 'non-parallel effects' in the non-linear stage of instability development. In the study of transitional flows, linear-stability theory (112) is a powerful technique to analyze the evolution of modes within small amplitudes. While it fails as the growth rate of disturbances becomes finite and non-parallel effects come into play.

In the case of natural transition, the non-linear growth of instability is preceded by the linear growth of unstable modes fed by the passive mechanism. The first stage of transition can be

established either through superimposing unstable modes in the form of free-stream turbulence to the base flow or superimposing continuous unstable modes in the wall boundary. In either case, the continuous excitation is the key to simulating the spatial transition analysis. While in the temporal analysis one-time excitation triggers the transition to turbulence in time.

In this work, the natural transition setup is based on the numerical experimentation of Rist and Fasel (70) for studying the convective type of instability. The continuous excitation via periodic blowing/suction boundary condition from the wall is a technique proposed by Rist and Fasel (70) to reproduce the unstable modes as in the experiment of Kachanov and Levchenko (69). Their pioneer work introduces a smart technique to feed pure uncontaminated T-S waves through a localized periodic blowing/suction strip on the wall. In the results section, DNS of Sayadi *et al.* (10) serves as the reference work against which the results are validated.

The spatial growth of T-S waves by virtue of a series of instabilities, from primary to secondary and tertiary, is calculated from the momentum equations, along with partial modeling of the physics in the subgrid scales. PANS has already shown fidelity in capturing underlying physics of spatially-evolving turbulent flows (Chapter 4). Although, this study is among the firsts which address the laminar-to-turbulent transition using the partially averaged Navier-Stokes (PANS) method.

This work targets the spatial amplification of small-amplitude two-dimensional linear TS waves in the downstream. It is well-established that the level of dissipation, in terms of numerical and viscous dissipation, is critical to allow for the receptivity due to blowing/suction. Specially, when it comes to bridging scale-resolving simulations (B-SRS), this criterion is more pronounced since the logic behind B-SRS is to lower the computational Reynolds number by increasing the effective viscosity.

In this chapter, details of the simulation is first described in section 6.2. Then, the results are discussed in terms of the modeling consistency, integral quantities, first and second order moments, and visualization of structures.

6.2 Simulation procedure

6.2.1 Computational setup

Controlling the level of dissipation, numerical or viscous, is the key to make the computation of natural transition to turbulence affordable yet accurate (71; 72). In order to generate the natural progression of laminar-to-turbulent transition, we define the Blasius base flow, along with meaningful infinitesimal turbulence quantities at the inlet to minimize the background turbulence. The inflow boundary layer thickness is defined based on the fact that the distance of inlet plane from the leading edge of the plate is $x_0 = 1(m)$. The boundary layer thickness for the laminar flow is expressed as (113):

$$\frac{\delta}{x} = \frac{5}{\sqrt{Re_x}}, \tag{6.1}$$

where, δ is the boundary layer thickness; Re_x is the Reynolds number; x is the distance from the leading edge. The free-stream velocity is set to $U_\infty = 0.2(m/s)$, and the kinematic viscosity is $\nu = 2 \times 10^{-5}(m/s^2)$. The inflow Reynolds number based on the streamwise distance from the leading edge is equal to $Re_{xin} = 10^5$. The flow field is initialized with the laminar flow such that the outflow boundary layer thickness equals $\delta_{out} = \delta_{in}\sqrt{x_{out}/x_{in}} = 0.049(m)$.

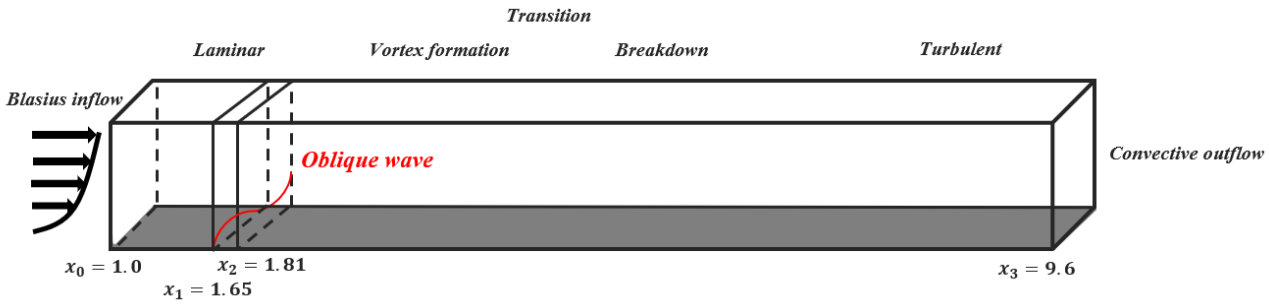

Figure 6.2: Sketch of the flow domain.

6.2.2 Boundary condition

Pure uncontaminated T-S waves are imposed on the base flow through a localized periodic zero-net-mass-flux blowing/suction boundary condition on the wall (111; 71). Zero net-mass flux is satisfied due to the fact that the temporal average of imposed wall-normal velocity along the blowing/suction strip is zero. The wall-normal velocity over the blowing/suction strip is expressed as the combination of the two-dimensional fundamental wave and three-dimensional oblique wave (71):

$$v = A_1 f(x) sin(\omega_1 t) + A_{1/2} f(x) g(z) cos(\omega_{1/2} t), \tag{6.2}$$

where A_1, $A_{1/2}$, ω_1, $\omega_{1/2}$ are the amplitudes and frequencies of the fundamental and subharmonic waves, respectively. Fundamental and subharmonic breakdowns have been respectively introduced by Klebanoff *et al.* (109) and Kachanov *et al.* (114). For the fundamental K-type transition, which is the subject of current research, the three-dimensional oblique wave has the same excitation frequency as the two-dimensional fundamental wave, i.e. $\omega_1 = \omega_{1/2}$. The non-dimensional frequency of excitation is chosen to be $F = \omega\nu/U_\infty^2 = 1.24 \times 10^{-4}$. The amplitudes are set to $A_1 = 0.0001$ and $A_{1/2} = 0.000015$. According to the neutral stability curve computed by Saric and Nayfeh (115), the prescribed frequency of the blowing/suction waves lies within the unstable range. It should be noted that the amplitudes are small enough to replicate the linear growth of disturbances and not to directly bypass to non-linear growth of superimposed waves in the streamwise direction. The spatial function of $f(x)$ is written in the form:

$$\begin{aligned} |f(x)| &= 15.1875\xi^5 - 35.4375\xi^4 + 20.25\xi^3, \\ \xi &= \begin{cases} \frac{x-x_1}{x_m-x_1}, & \text{for} \quad x_1 \le x \le x_m; \\ \frac{x_2-x}{x_2-x_m}, & \text{for} \quad x_m \le x \le x_2. \end{cases} \end{aligned} \tag{6.3}$$

where x_m represents the midpoint of strip. λ_x is the wavelength of the two-dimensional wave in the streamwise direction which is equal to the streamwise extension of strip, $\alpha = \frac{2\pi}{(1.81-1.65)}$. The

three-dimensional oblique wave is defined by the superimposition of streamwise and spanwise waves. The spanwise distribution of oblique wave is defined as:

$$g(z) = cos(\frac{2\pi z}{\lambda_z}), \tag{6.4}$$

where λ_z is the wavelength of the three-dimensional oblique wave in the spanwise direction. Assuming $\lambda_z = 0.15(m)$, the wave number in the spanwise direction will be $\beta = \frac{2\pi}{0.15}$. Consequently, the combination of waves makes an oblique wave in the plane of $\pi/4$ with respect to the z plane. The blowing/suction coordinates are mapped such that all the points lay between -1 and 1 in x and z directions:

$$X = \frac{x_{min} - x}{x_{min} - x_{max}} \quad ; \quad Z = \frac{z_{min} - z}{z_{min} - z_{max}}. \tag{6.5}$$

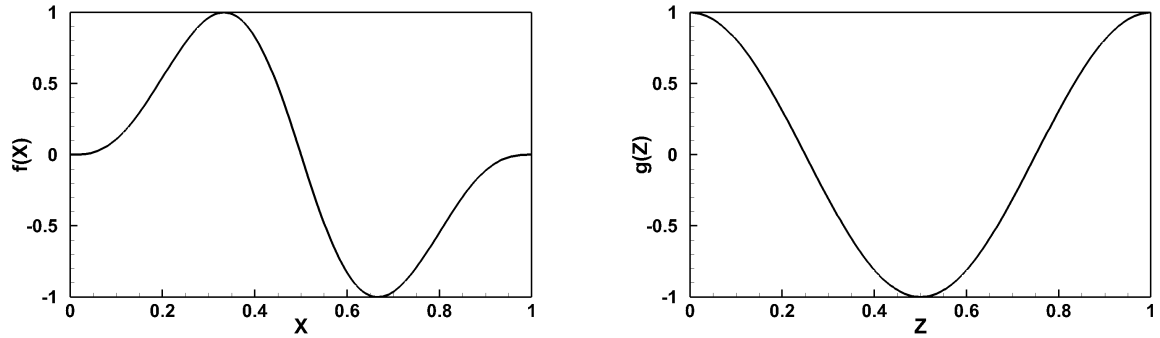

(a) (b)

Figure 6.3: Regulation functions for the blowing–suction: (a) f(x), (b) g(z).

6.2.3 Numerical scheme

The numerical diffusion is one of the main challenges in transitional flow computations. In this work, the Crank-Nicolson time integration scheme, along with the central-differencing method

for the spatial integration are employed. It is verified that the second-order temporal and spatial schemes suffice for the purpose of numerical integration, considering the fact that a well-structured mesh is used here. Solution of the system of algebraic discretized equations throughout the control volumes is carried out using the pisoFOAM solver, a built-in transient solver in OpenFOAM.

6.3 Results and discussion

In order to study the effect of degree of resolution on the transitional flow behavior, three different test cases, listed in (Table 6.1), are studied. It has been observed that inadequate spanwise grid resolution leads to relaminarization of the excited flow field in the downstream direction as the excessive numerical diffusion kills the T-S instability. In the next subsections, first we ensure that the desired degree of unsteadiness is resolved. Then, the results in terms of one-point statistics are discussed.

Table 6.1: Details of the test cases examined for the natural transition.

Simulation	L_x	L_y	L_z	N_x	N_y	N_z	N_{total}	f_k
PANS-Case1	9.6	1	0.3	1000	150	100	15×10^6	0.1
PANS-Case2	9.6	1	0.3	1000	150	70	10.5×10^6	0.1
PANS-Case3	9.6	1	0.3	1000	100	45	4.5×10^6	0.1
DNS (10)	9.6	0.92	0.6	4096	550	512	1.15×10^9	–

6.3.1 Internal consistency

In order to ensure that the resolved portion of the unsteadiness is consistent with the prescribed value of resolution control parameter f_k, the ratio of $k_{unresolved}/k_{total}$ is computed in the post-processing stage. According to Figure 6.4, a posteriori value is in adequate agreement with the prescribed f_k quantity. In fact, the recovered quantity reveals the fact that almost %90 of the flow unsteadiness is resolved in the PANS simulation. In the next part, it is shown that the resolved portion is able to effectively predict the underlying physics of external transitional flow over a zero-pressure gradient flat plate.

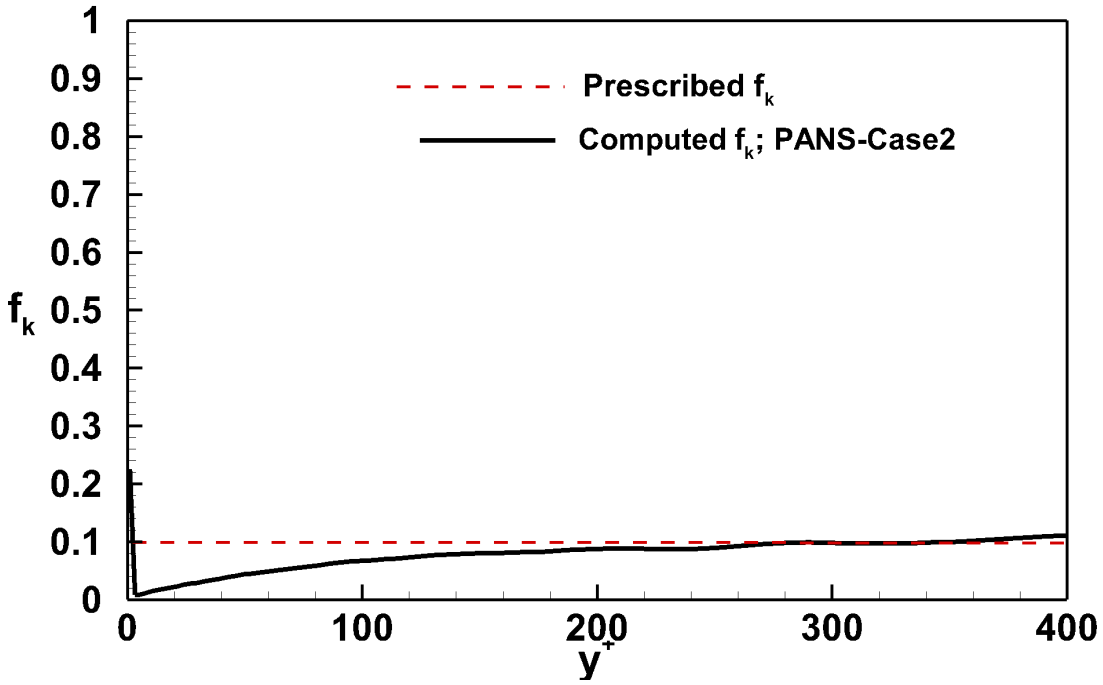

Figure 6.4: Internal consistency of the resolution control parameter at $Re = 6.8 \times 10^5$.

6.3.2 Integral quantities

The evolution of skin friction coefficient, $c_f = \tau_w / \frac{1}{2}\rho U^2$, along the plate for each case is shown in Figure 6.5. The transition point is the first key point where the flow departs from the laminar c_f curve at $Re_x \approx 3 \times 10^5$. The second main point is the overshoot in the c_f plot at $Re_x \approx 3.5 \times 10^5$, which is clearly observable (Figure 6.5). The overshoot of skin friction coefficient, being the signature of natural transition, is captured even with a finite active turbulent viscosity throughout the flow domain. Although Huai *et al.* (71) and Sayadi and Moin (72) have shown that a special treatment of the LES subgrid scale modeling is required for the unstable T-S wave to survive. This overshoot manifests the late transition, where the non-linear interaction with the emergence of secondary instability is dominant. After $Re_x \approx 5.5 \times 10^5$, the flow asymptotes to the fully-developed turbulent state. According to Figure 6.5, the agreement of PANS with the DNS of Sayadi *et al.*(10) and fully-turbulent curve (113) is noticeable in terms of the transition spot and

evolution of skin-friction coefficient along the flat plate. It should be kept in mind that the observed discrepancy in the friction coefficient between PANS and DNS can be due to different excitation frequencies.

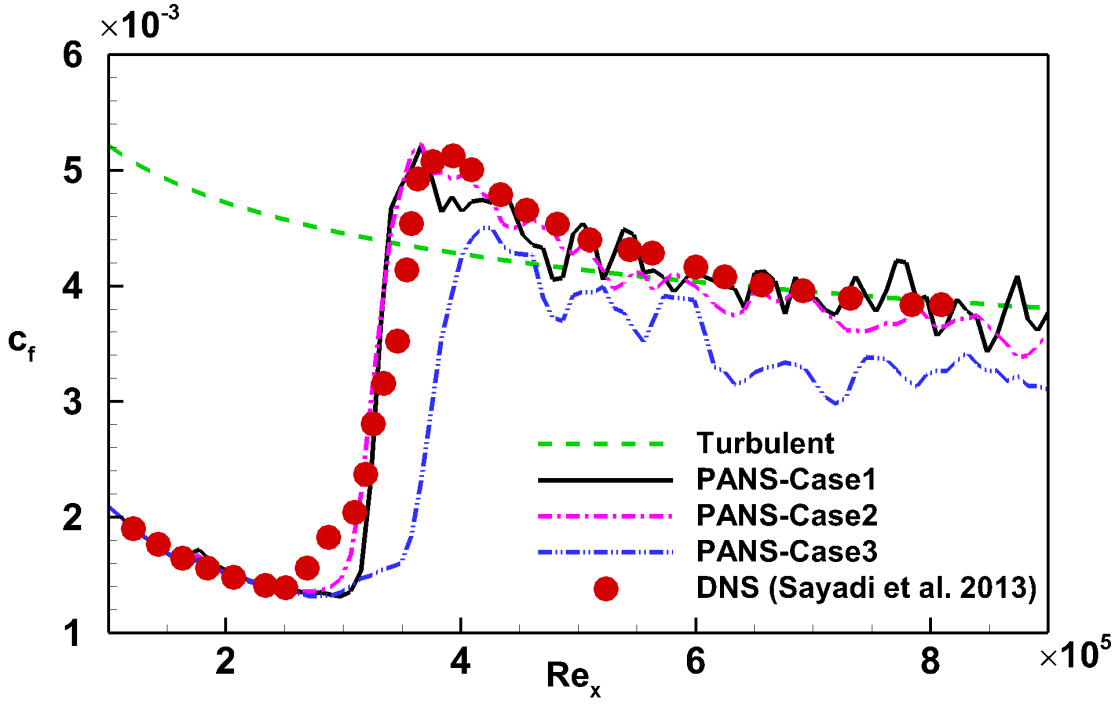

Figure 6.5: Evolution of skin friction as a function of Reynolds number.

Figure 6.6 depicts the evolution of shape factor H versus the momentum Reynolds number Re_θ. Shape factor is defined as the ratio of displacement thickness over the momentum thickness, $H = \delta^*/\theta$. According to this figure, shape factor settles to constant value of $H = 1.4$ at the fully-developed regime. It is worth mentioning that 1.4 is typical of fully-developed turbulence (4).

According to Figure 6.7, starting from $x = 2(m)$ corresponding to $Re_x \approx 3 \times 10^5$, the contour of du'/dy reveals shear-layer bulges associated with the divergence from the laminar curve on c_f plot. The vortical role-up initiation elucidates the shear layer between sweep and ejection mecha-

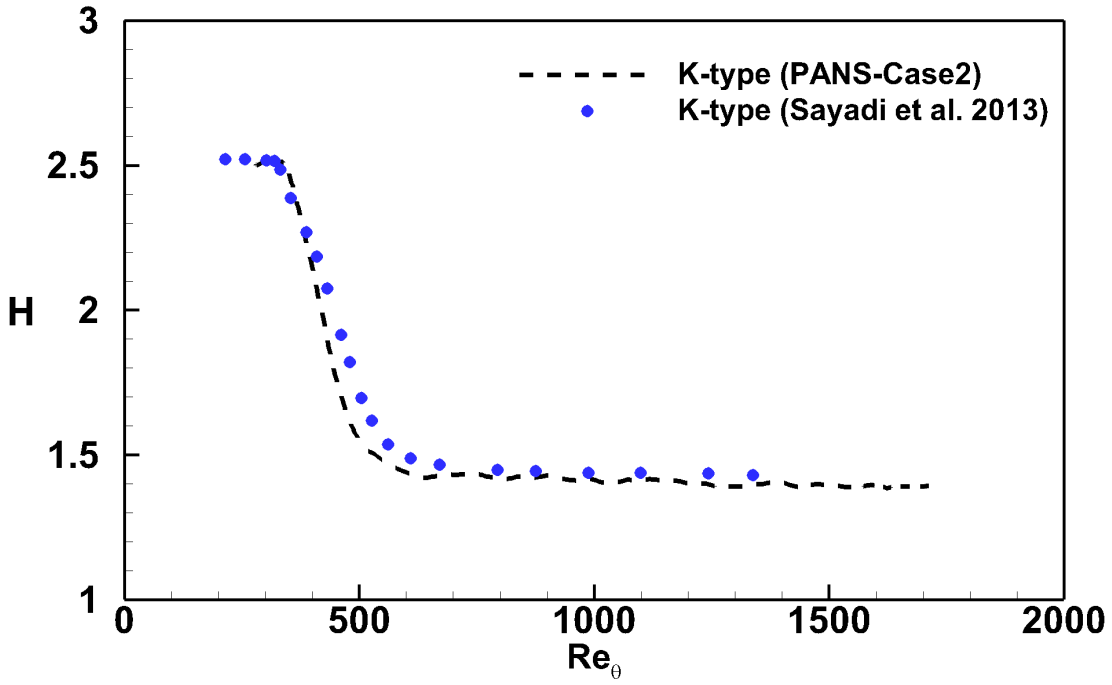

Figure 6.6: Evolution of shape factor as a function of momentum thickness Reynolds number.

nisms. Figure 6.8 shows the iso-surfaces of the second invariant of the velocity gradient tensor for $Q = 0.04(1/s^2)$. It clearly visualizes the evolution of vortical structures from the two-dimensional waves in the laminar regime to spanwise undulation and breakdown to turbulence.

In the nonlinear secondary instability region, extra modes with fractions of subharmonic frequency start forming. These interactions give rise to laminar breakdown at $Re_x \approx 4 \times 10^5$, where large vortical structures emerge.

6.3.3 One-point statistics

6.3.3.1 Mean velocity field

Figure 6.9a and 6.9b display how the streamwise velocity profiles evolve in downstream for PANS-Case2 and DNS computations, respectively. In particular, Figure 6.10 compares the difference between corresponding profiles point-by-point. Although some discrepancy is observable,

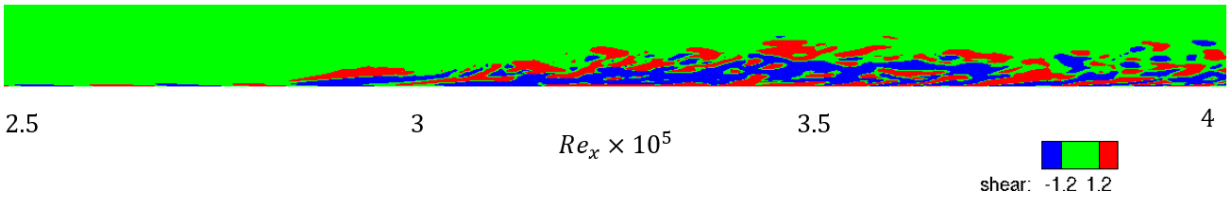

Figure 6.7: Vertical shear du'/dy at $8T_f$ (s).

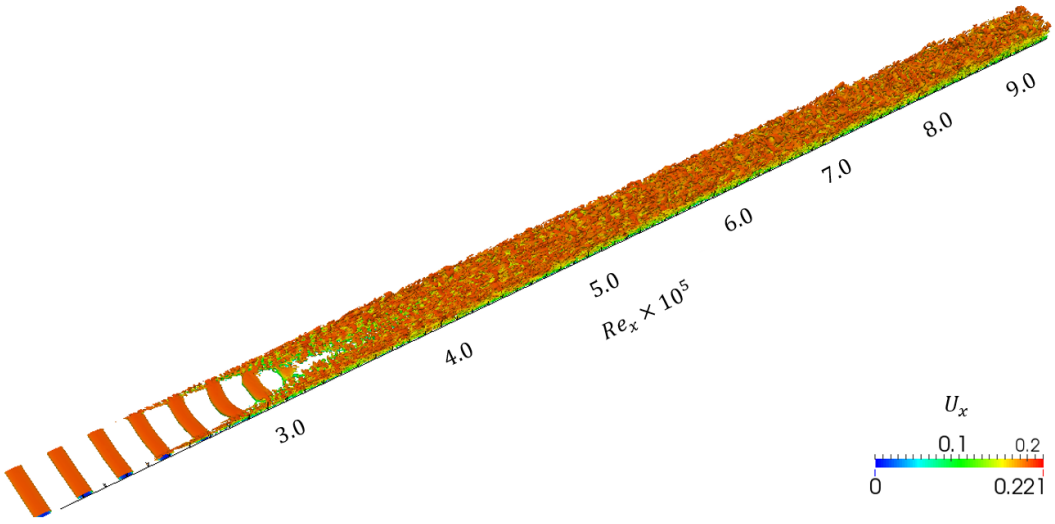

Figure 6.8: Iso-surfaces of the second invariant of the velocity gradient tensor.

both PANS and DNS experience the same path from laminar to turbulent regimes. The discrepancy between PANS and DNS velocity profiles emanates from two main reasons: (i) different excitation frequencies, and (ii) different effective viscosities. Figure 6.10h delineates the fact that as $Re_x = 7 \times 10^5$ is approached, the total agreement between PANS and DNS improves.

6.3.3.2 Stress profiles

Figure 6.11 shows different components of the second-order moments corresponding to PANS-Case 2 in Table 6.1, where the results are benchmarked against the DNS of Sayadi *et al.* (10). In this figure, from top to bottom, the streamwise normal stress, spanwise normal stress, wall-normal

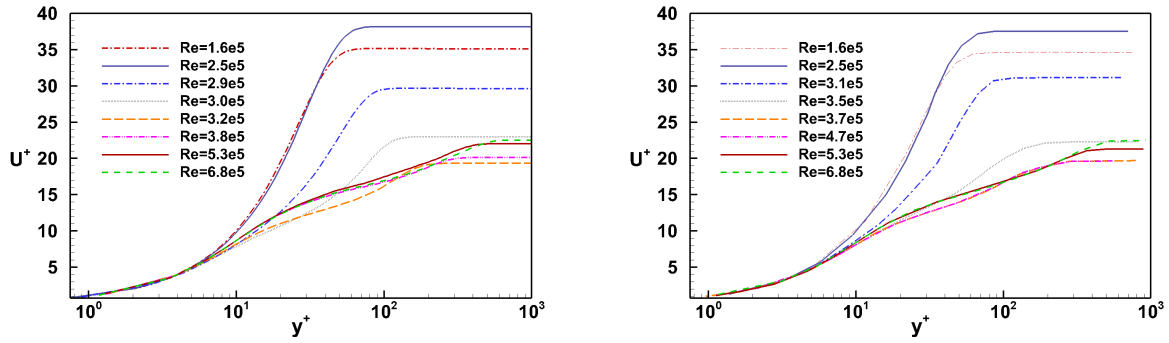

Figure 6.9: Evolution of the mean streamwise velocity profile in the stream parallel direction (a) PANS, (b) DNS taken from [10]

stress, shear stress are displayed, respectively. The agreement of stress profiles between PANS and DNS confirms that PANS has settled to the fully-developed turbulence at $Re_x = 6.8 \times 10^5$.

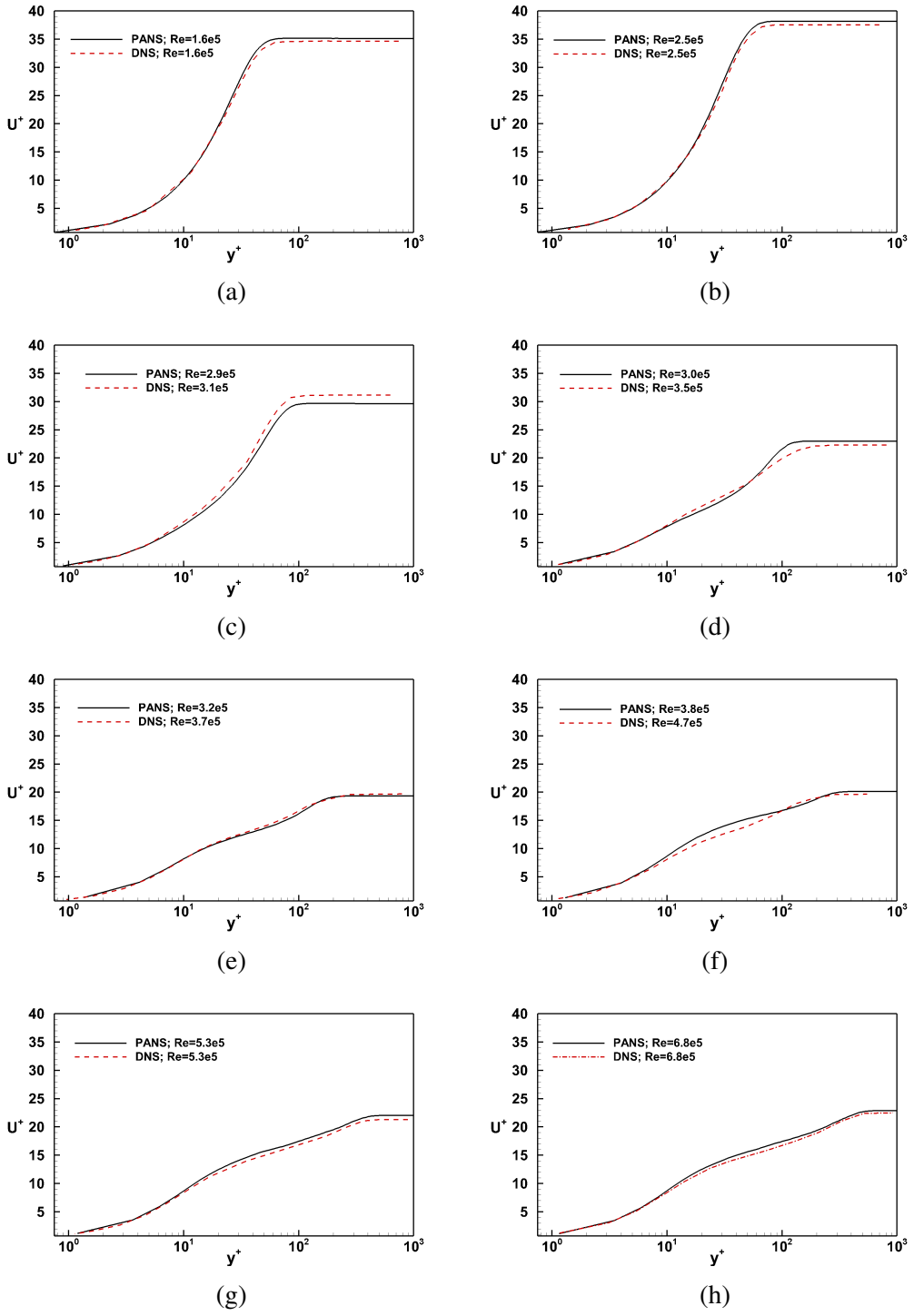

Figure 6.10: Comparative study of the streamwise velocities for PANS and DNS along the plate at: (a) $Re_{x_{PANS}} = 1.6 \times 10^5$, (b) $Re_{x_{PANS}} = 2.5 \times 10^5$, (c) $Re_{x_{PANS}} = 2.9 \times 10^5$, (d) $Re_{x_{PANS}} = 3.0 \times 10^5$, (e) $Re_{x_{PANS}} = 3.2 \times 10^5$, (f) $Re_{x_{PANS}} = 3.8 \times 10^5$, (g) $Re_{x_{PANS}} = 5.3 \times 10^5$, (h) $Re_{x_{PANS}} = 6.8 \times 10^5$.

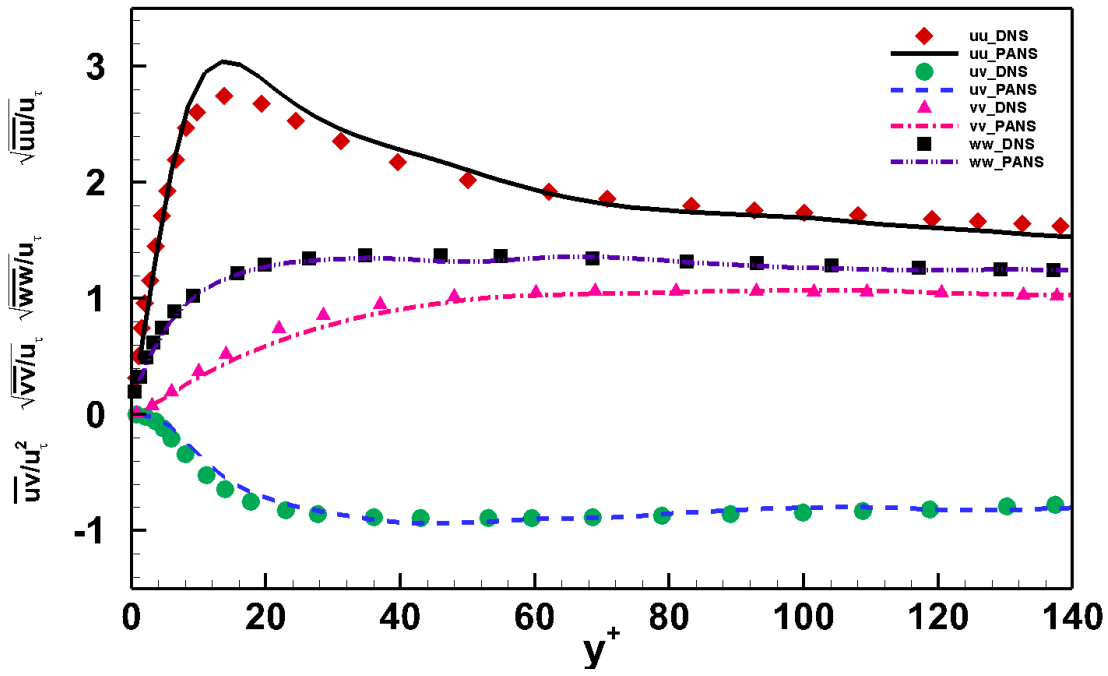

Figure 6.11: Wall-normal distribution of second order moments at $Re_x = 6.8 \times 10^5$.

7. CONCLUSION

The B-SRS approach of choice in this thesis is the Partially-Averaged Navier-Stokes (PANS) model. According to this methodology, non-universal large-scale structures are calculated from the partially averaged Navier-Stokes equations and unresolved scales are modeled by the modified PANS $k-\omega$ two-equation closures. This dissertation makes a contribution to incorporating physics into the subfilter closures and meaningful perturbed inflow condition for turbulence evolution equations. Capability of the developed subfilter closure is assessed for temporal analysis of fully-developed turbulence and spatial analysis of turbulent and transitional flows. Important steps toward commercializing PANS have been taken as a result of these advancements. This section summarizes the main conclusions of each of the three studies.

(i) In the first study, we derive turbulent transport models for two-equation closures in the context of scale resolving simulations (SRS) of turbulence. Toward this end, along the lines of RANS methodology, we develop the equilibrium boundary layer analysis of filtered flow fields. The analysis leads to a closure model for turbulent-transport Prandtl numbers $\sigma_{\omega u}$ and, ultimately, to σ_{ku}, in terms of resolution control parameters - f_k,f_ω.

Employing the new turbulent transport closure models, PANS simulations of turbulent channel flow are performed at different Reynolds numbers. It is first demonstrated that PANS computations do yield the prescribed eddy-viscosity reduction. Further, the computations exhibit the required balance between production and dissipation. Then the PANS results are compared against established DNS and experimental data. The mean flow profile, Reynolds stress magnitude and anisotropy are well captured by the PANS computations. Analyses of the energy spectra and two-point correlation further confirm the fidelity of PANS methodology. It is also shown that unsteady flow structures such as hair-pin packets are simulated adequately. This work is among the first bridging scale-resolving simulations which has achieved such maturity as to capturing dynamics of coherent structures within the wall-

bounded fully turbulent flows.

The development in this work focuses on constant f_k resolution. Works are currently underway to extend the model for spatially varying f_k. This will enable PANS simulation to go from RANS ($f_k = 1$) at the wall to high degree of resolution ($f_k < 1$) in the interior of the flow. The analysis and simulations presented in this work represent an important step forward toward using two-equation closures for scale resolving simulations of practical turbulent flows.

(ii) The second study develops a perturbed inflow condition for turbulence properties, consistent with the resolved field, in bridging scale-resolving simulations. Toward this end, we employ PANS as a robust bridging scale-resolving method. The definition of the inflow velocity field is based on the recycling/rescaling method. In PANS, in order for a computation to asymptote to the desirable equilibrium state, functionality of PANS must be ensured. Through the internal consistency studies, it is shown that the meaningful prescription of subfilter turbulence quantities are prerequisite for a B-SRS to function. Since PANS adapts second moment closure, the dynamical behavior of the PANS simulation is described by evolution equations for filtered velocity, along with two subfilter turbulence quantities.

A cost-effective PANS simulation of incompressible turbulent boundary layer over a smooth flat plate with the momentum thickness Reynolds number $650 \leq Re_\theta \leq 1434$ is studied. The results are compared with the established data in literature. In depth analysis of one-point statistics in terms of the integral quantities, mean flow profile, Reynolds stress profile, skewness and flatness, budget of kinetic energy show adequate agreements with DNS. Furthermore, the two-point correlation and visualization of structures yield reasonably accurate information as to the organization of coherent structures in the near-wall region.

By ensuring the functionality of scale-resolving simulations, the developed perturbed inflow condition can be regarded as an important step toward increasing the reliability of scale-resolving simulations in practical engineering problems.

(iii) The third work targets the underlying physics recovery of natural transition using a viable computational cost. We leverage the PANS capability in resolving the transitional behavior of the external flow using an affordable computational cost. It has been shown that wall-resolved PANS is capable of predicting the transition point effectively. The overshoot of skin friction coefficient, being the signature of natural transition, is captured even with a finite active turbulent viscosity in the pre-transition region. It has been demonstrated that PANS can be regarded as a predictive approach for external transitional flows.

Although this work establishes the foundation of PANS in transition problems, in the future attempts, employment of wall-modelled PANS (WM-PANS) in transitional flows will be addressed, where the spatial variation of flow physics will be included in the subgrid scale modeling using spatial variable f_k function.

Future work

Despite a rich body of literature on PANS, there are some areas which have yet to be addressed, in future efforts:

(i) To employ machine learning methods for data-driven turbulence modeling to account for the anisotropy due to the near-wall effects.

(ii) To develop closure modeling for f_ε in low-Reynolds-number flows with $f_\varepsilon < 1$.

(iii) To advance capability of PANS to compressible and high-speed turbulent flows.

(iv) To leverage the variable-resolution PANS (VR-PANS) for transitional flows through minimizing the eddy viscosity in the pre-transition region and alleviating the computational demands of fully-developed turbulence.

REFERENCES

[1] P. Tazraei and S. S. Girimaji, "Scale-resolving simulations of turbulence: Equilibrium boundary layer analysis leading to near-wall closure modeling," *Physical Review Fluids*, vol. 4, no. 10, p. 104607, 2019.

[2] S. Hoyas and J. Jiménez, "Reynolds number effects on the Reynolds-stress budgets in turbulent channels," *Physics of Fluids (1994-present)*, vol. 20, no. 10, p. 101511, 2008.

[3] J. A. Sillero, J. Jiménez, and R. D. Moser, "Two-point statistics for turbulent boundary layers and channels at Reynolds numbers up to $\delta^+ \approx 2000$," *Physics of Fluids*, vol. 26, no. 10, p. 105109, 2014.

[4] P. R. Spalart, "Direct simulation of a turbulent boundary layer up to $Re_\theta = 1410$," *Journal of fluid mechanics*, vol. 187, pp. 61–98, 1988.

[5] X. Wu and P. Moin, "Direct numerical simulation of turbulence in a nominally zero-pressure-gradient flat-plate boundary layer," *Journal of Fluid Mechanics*, vol. 630, pp. 5–41, 2009.

[6] R. S. Barlow and J. P. Johnston, "Structure of a turbulent boundary layer on a concave surface," *Journal of Fluid Mechanics*, vol. 191, pp. 137–176, 1988.

[7] H. Le, P. Moin, and J. Kim, "Direct numerical simulation of turbulent flow over a backward-facing step," *Journal of fluid mechanics*, vol. 330, pp. 349–374, 1997.

[8] P. Schlatter, Q. Li, G. Brethouwer, A. V. Johansson, and D. S. Henningson, "Simulations of spatially evolving turbulent boundary layers up to $Re_\theta = 4300$," *International Journal of Heat and Fluid Flow*, vol. 31, no. 3, pp. 251–261, 2010.

[9] M. V. Morkovin, E. Reshotko, and T. Herbert, "Transition in open flow systems—a reassessment," in *Bull. Am. Phys. Soc., 39. 1882*, 1994.

[10] T. Sayadi, C. W. Hamman, and P. Moin, "Direct numerical simulation of complete H-type and K-type transitions with implications for the dynamics of turbulent boundary layers," *Journal of Fluid Mechanics*, vol. 724, pp. 480–509, 2013.

[11] B. E. Launder, G. J. Reece, and W. Rodi, "Progress in the development of a Reynolds-stress turbulence closure," *Journal of fluid mechanics*, vol. 68, no. 3, pp. 537–566, 1975.

[12] M. Germano, "Fundamentals of large eddy simulation," in *Advanced Turbulent Flow Computations*, pp. 81–130, Springer, 2000.

[13] P. Moin and K. Mahesh, "Direct numerical simulation: a tool in turbulence research," *Annual review of fluid mechanics*, vol. 30, no. 1, pp. 539–578, 1998.

[14] F. Menter and M. Kuntz, "Adaptation of eddy-viscosity turbulence models to unsteady separated flow behind vehicles," in *The aerodynamics of heavy vehicles: trucks, buses, and trains*, pp. 339–352, Springer, 2004.

[15] P. R. Spalart, S. Deck, M. L. Shur, K. D. Squires, M. K. Strelets, and A. Travin, "A new version of detached-eddy simulation, resistant to ambiguous grid densities," *Theoretical and computational fluid dynamics*, vol. 20, no. 3, p. 181, 2006.

[16] M. L. Shur, P. R. Spalart, M. K. Strelets, and A. K. Travin, "A hybrid RANS-LES approach with delayed-DES and wall-modelled LES capabilities," *International Journal of Heat and Fluid Flow*, vol. 29, no. 6, pp. 1638–1649, 2008.

[17] S. S. Girimaji and K. S. Abdol-Hamid, "Partially averaged Navier–Stokes model for turbulence: implementation and validation," *AIAA paper*, vol. 502, p. 2005, 2005.

[18] B. Chaouat and R. Schiestel, "A new partially integrated transport model for subgrid-scale stresses and dissipation rate for turbulent developing flows," *Physics of Fluids (1994-present)*, vol. 17, no. 6, p. 065106, 2005.

[19] P. Sagaut, *Multiscale and multiresolution approaches in turbulence: LES, DES and hybrid RANS/LES methods: applications and guidelines*. World Scientific, 2013.

[20] C. Speziale, "Turbulence modeling for time-dependent RANS and VLES: a review," *AIAA journal*, vol. 36, no. 2, pp. 173–184, 1998.

[21] S. S. Girimaji, "Partially-Averaged Navier-Stokes Model for turbulence: A Reynolds-Averaged Navier-Stokes to direct numerical simulation bridging method," *Journal of Applied Mechanics*, vol. 73, pp. 413–421, 2006.

[22] S. S. Girimaji, E. Jeong, and R. Srinivasan, "Partially averaged Navier-Stokes method for turbulence: Fixed point analysis and comparison with unsteady partially averaged Navier-Stokes," *Journal of Applied Mechanics*, vol. 73, no. 3, pp. 422–429, 2006.

[23] D. A. Reyes, J. M. Cooper, and S. S. Girimaji, "Characterizing velocity fluctuations in partially resolved turbulence simulations," *Physics of Fluids*, vol. 26, no. 8, p. 085106, 2014.

[24] P. Razi, *Partially-averaged Navier-Stokes (PANS) Method for Turbulence Simulations: Near-wall Modeling and Smooth-surface Separation Computations*. PhD thesis, Texas A&M University, 2016.

[25] P. Razi, P. Tazraei, and S. Girimaji, "Partially-averaged Navier–Stokes (PANS) simulations of flow separation over smooth curved surfaces," *International Journal of Heat and Fluid Flow*, vol. 66, pp. 157–171, 2017.

[26] S. Lakshmipathy and S. S. Girimaji, "Partially-averaged Navier–Stokes (PANS) method for turbulence simulations: flow past a circular cylinder," *Journal of Fluids Engineering*, vol. 132, no. 12, p. 121202, 2010.

[27] E. Jeong and S. S. Girimaji, "Partially averaged Navier–Stokes (PANS) method for turbulence simulations—Flow past a square cylinder," *Journal of Fluids Engineering*, vol. 132, no. 12, p. 121203, 2010.

[28] D. Higuera Caubilla, P. Razi, S. K. Sekhar, N. N. Mansour, and S. Girimaji, "PANS Simulations of Turbulent Separated Flow over a Wall-mounted Hump," in *22nd AIAA Computational Fluid Dynamics Conference*, p. 2463, 2015.

[29] P. Razi and S. S. Girimaji, "Simulation of Smooth Surface Separation Using the Partially-averaged Navier-Stokes Method," in *Progress in Hybrid RANS-LES Modelling*, pp. 411–420, Springer, 2015.

[30] S. Krajnović, G. Minelli, and B. Basara, "Partially-averaged Navier–Stokes simulations of two bluff body flows," *Applied mathematics and computation*, vol. 272, pp. 692–706, 2016.

[31] S. Krajnović, R. Lárusson, and B. Basara, "Superiority of PANS compared to LES in predicting a rudimentary landing gear flow with affordable meshes," *International Journal of*

Heat and Fluid Flow, vol. 37, pp. 109–122, 2012.

[32] R. Lárusson, *Aerodynamic Flow Simulation of a Rudimentary Landing Gear Using PANS and LES*. Master's thesis, Chalmers University of Technology, 2011.

[33] R. E. Bensow and M. van den Boogaard, "Using a PANS Simulation Approach for the Transient Flow around the Japan Bulk Carrier," *Journal of Ship Research*, vol. 63, no. 2, pp. 123–129, 2019.

[34] M. Mirzaei, S. Krajnović, and B. Basara, "Partially-Averaged Navier–Stokes simulations of flows around two different Ahmed bodies," *Computers & Fluids*, vol. 117, pp. 273–286, 2015.

[35] X. Han, S. Krajnović, and B. Basara, "Study of active flow control for a simplified vehicle model using the PANS method," *International journal of heat and fluid flow*, vol. 42, pp. 139–150, 2013.

[36] S. Krajnovic, G. Minelli, and B. Basara, "Partially-averaged Navier-Stokes simulations of flows around generic vehicle at yaw," tech. rep., SAE Technical Paper, 2016.

[37] D. R. Chapman, "Computational aerodynamics development and outlook," *AIAA journal*, vol. 17, no. 12, pp. 1293–1313, 1979.

[38] X. I. Yang and S. T. Bose, "A physical basis of the slip-wall model for wall-modeled large-eddy simulations," in *10th International Symposium on Turbulence and Shear Flow Phenomena (TSFP10)*, 2017.

[39] U. Piomelli and E. Balaras, "Wall-layer models for large-eddy simulations," *Annual review of fluid mechanics*, vol. 34, no. 1, pp. 349–374, 2002.

[40] S. Kawai and J. Larsson, "Wall-modeling in large eddy simulation: Length scales, grid resolution, and accuracy," *Physics of Fluids*, vol. 24, no. 1, p. 015105, 2012.

[41] S. T. Bose and G. I. Park, "Wall-modeled large-eddy simulation for complex turbulent flows," *Annual Review of Fluid Mechanics*, vol. 50, pp. 535–561, 2018.

[42] M. Wang and P. Moin, "Dynamic wall modeling for large-eddy simulation of complex turbulent flows," *Physics of Fluids*, vol. 14, no. 7, pp. 2043–2051, 2002.

[43] J. Kim, P. Moin, and R. Moser, "Turbulence statistics in fully developed channel flow at low Reynolds number," *Journal of fluid mechanics*, vol. 177, pp. 133–166, 1987.

[44] R. D. Moser, J. Kim, and N. N. Mansour, "Direct numerical simulation of turbulent channel flow up to Re_τ= 590," *Physics of fluids*, vol. 11, no. 4, pp. 943–945, 1999.

[45] S. Hoyas and J. Jiménez, "Scaling of the velocity fluctuations in turbulent channels up to Re_τ= 2003," *Physics of fluids*, vol. 18, no. 1, p. 011702, 2006.

[46] T. Theodorsen, "Mechanisms of turbulence," in *Proceedings of the 2nd Midwestern Conference on Fluid Mechanics*, 1952.

[47] R. J. Adrian, C. D. Meinhart, and C. D. Tomkins, "Vortex organization in the outer region of the turbulent boundary layer," *Journal of Fluid Mechanics*, vol. 422, pp. 1–54, 2000.

[48] K. Christensen and R. J. Adrian, "Statistical evidence of hairpin vortex packets in wall turbulence," *Journal of Fluid Mechanics*, vol. 431, pp. 433–443, 2001.

[49] R. Adrian and Z. Liu, "Observation of vortex packets in direct numerical simulation of fully turbulent channel flow," *Journal of visualization*, vol. 5, no. 1, pp. 9–19, 2002.

[50] R. J. Adrian, "Hairpin vortex organization in wall turbulence," *Physics of Fluids*, vol. 19, no. 4, p. 041301, 2007.

[51] J. Jiménez and A. Lozano-Durán, "Coherent structures in wall-bounded turbulence," in *Progress in Wall Turbulence 2*, pp. 37–46, Springer, 2016.

[52] A. M. Akbarzadeh and I. Borazjani, "Large eddy simulations of a turbulent channel flow with a deforming wall undergoing high steepness traveling waves," *Physics of Fluids*, vol. 31, no. 12, p. 125107, 2019.

[53] A. Akbarzadeh and I. Borazjani, "Reducing flow separation of an inclined plate via travelling waves," *Journal of Fluid Mechanics*, vol. 880, pp. 831–863, 2019.

[54] A. Akbarzadeh and I. Borazjani, "A numerical study on controlling flow separation via surface morphing in the form of backward traveling waves," in *AIAA Aviation 2019 Forum*, p. 3589, 2019.

[55] H. Asadi, H. Asgharzadeh, and I. Borazjani, "On the scaling of propagation of periodically

generated vortex rings," *Journal of Fluid Mechanics*, vol. 853, pp. 150–170, 2018.

[56] H. Asadi, M. Taeibi-Rahni, A. M. Akbarzadeh, K. Javadi, and G. Ahmadi, "Investigation of Hydrodynamically Dominated Membrane Rupture, Using Smoothed Particle Hydrodynamics–Finite Element Method," *Fluids*, vol. 4, no. 3, p. 149, 2019.

[57] H. Asgharzadeh, H. Asadi, H. Meng, and I. Borazjani, "A non-dimensional parameter for classification of the flow in intracranial aneurysms. II. Patient-specific geometries," *Physics of Fluids*, vol. 31, no. 3, p. 031905, 2019.

[58] S. Y. Motlagh and S. Taghizadeh, "POD analysis of low Reynolds turbulent porous channel flow," *International Journal of Heat and Fluid Flow*, vol. 61, pp. 665–676, 2016.

[59] G. Khujadze and M. Oberlack, "DNS and scaling laws from new symmetry groups of ZPG turbulent boundary layer flow," *Theoretical and computational fluid dynamics*, vol. 18, no. 5, pp. 391–411, 2004.

[60] J. C. Klewicki, "Reynolds number dependence, scaling, and dynamics of turbulent boundary layers," *Journal of fluids engineering*, vol. 132, no. 9, p. 094001, 2010.

[61] I. Marusic, B. McKeon, P. Monkewitz, H. Nagib, A. Smits, and K. Sreenivasan, "Wall-bounded turbulent flows at high Reynolds numbers: recent advances and key issues," *Physics of Fluids*, vol. 22, no. 6, p. 065103, 2010.

[62] A. J. Smits, B. J. McKeon, and I. Marusic, "High–Reynolds number wall turbulence," *Annual Review of Fluid Mechanics*, vol. 43, 2011.

[63] M. P. Simens, J. Jiménez, S. Hoyas, and Y. Mizuno, "A high-resolution code for turbulent boundary layers," *Journal of Computational Physics*, vol. 228, no. 11, pp. 4218–4231, 2009.

[64] T. Mukha and M. Liefvendahl, "The generation of turbulent inflow boundary conditions using precursor channel flow simulations," *Computers & Fluids*, vol. 156, pp. 21–33, 2017.

[65] P. Schlatter, R. Örlü, Q. Li, G. Brethouwer, J. H. Fransson, A. V. Johansson, P. H. Alfredsson, and D. S. Henningson, "Turbulent boundary layers up to $Re_\theta = 2500$ studied through simulation and experiment," *Physics of fluids*, vol. 21, no. 5, p. 051702, 2009.

[66] T. S. Lund, X. Wu, and K. D. Squires, "Generation of turbulent inflow data for spatially-

developing boundary layer simulations," *Journal of computational physics*, vol. 140, no. 2, pp. 233–258, 1998.

[67] P. Schlatter and R. Örlü, "Turbulent boundary layers at moderate Reynolds numbers: inflow length and tripping effects," *Journal of Fluid Mechanics*, vol. 710, pp. 5–34, 2012.

[68] G. B. Schubauer and H. K. Skramstad, "Laminar boundary-layer oscillations and stability of laminar flow," *Journal of the Aeronautical Sciences*, vol. 14, no. 2, pp. 69–78, 1947.

[69] Y. S. Kachanov and V. Y. Levchenko, "The resonant interaction of disturbances at laminar-turbulent transition in a boundary layer," *Journal of Fluid Mechanics*, vol. 138, pp. 209–247, 1984.

[70] U. Rist and H. Fasel, "Direct numerical simulation of controlled transition in a flat-plate boundary layer," *Journal of Fluid Mechanics*, vol. 298, pp. 211–248, 1995.

[71] X. Huai, R. D. Joslin, and U. Piomelli, "Large-eddy simulation of transition to turbulence in boundary layers," *Theoretical and computational fluid dynamics*, vol. 9, no. 2, pp. 149–163, 1997.

[72] T. Sayadi and P. Moin, "Large eddy simulation of controlled transition to turbulence," *Physics of Fluids*, vol. 24, no. 11, p. 114103, 2012.

[73] A. Lozano-Durán, M. Hack, and P. Moin, "Modeling boundary-layer transition in direct and large-eddy simulations using parabolized stability equations," *Physical Review Fluids*, vol. 3, no. 2, p. 023901, 2018.

[74] M. Kim, J. Lim, S. Kim, S. Jee, J. Park, and D. Park, "Large-eddy simulation with parabolized stability equations for turbulent transition using OpenFOAM," *Computers & Fluids*, vol. 189, pp. 108–117, 2019.

[75] S. Jee, J. Joo, and R.-S. Lin, "Toward cost-effective boundary layer transition computations with large-eddy simulation," *Journal of Fluids Engineering*, vol. 140, no. 11, p. 111201, 2018.

[76] Z. Yin and P. A. Durbin, "An adaptive DES smodel that allows wall-resolved eddy simulation," *International Journal of Heat and Fluid Flow*, vol. 62, pp. 499–509, 2016.

[77] M. Germano, "Turbulence: the filtering approach," *Journal of Fluid Mechanics*, vol. 238, pp. 325–336, 1992.

[78] S. S. Girimaji, R. Srinivasan, and E. Jeong, "PANS turbulence model for seamless transition between RANS and LES: fixed-point analysis and preliminary results," in *ASME/JSME 2003 4th Joint Fluids Summer Engineering Conference*, pp. 1901–1909, American Society of Mechanical Engineers Digital Collection, 2003.

[79] S. Lakshmipathy and S. Girimaji, "Partially-averaged Navier-Stokes method for turbulent flows: $k-\omega$ model implementation," in *44th AIAA aerospace sciences meeting and exhibit*, p. 119, 2006.

[80] F. S. Pereira, L. Eça, G. Vaz, and S. S. Girimaji, "Challenges in scale-resolving simulations of turbulent wake flows with coherent structures," *Journal of Computational Physics*, vol. 363, pp. 98–115, 2018.

[81] S. S. Girimaji and S. Wallin, "Closure modeling in bridging regions of variable-resolution (vr) turbulence computations," *Journal of Turbulence*, vol. 14, no. 1, pp. 72–98, 2013.

[82] F. Pereira, G. Vaz, L. Eça, and S. Girimaji, "Simulation of the flow around a circular cylinder at $Re = 3900$ with Partially-Averaged Navier-Stokes equations," *International Journal of Heat and Fluid Flow*, vol. 69, pp. 234–246, 2018.

[83] P. Ranjan and A. Dewan, "Partially-averaged Navier Stokes simulation of turbulent heat transfer from a square cylinder," *International Journal of Heat and Mass Transfer*, vol. 89, pp. 251–266, 2015.

[84] B. Basara, S. Krajnovic, S. Girimaji, and Z. Pavlovic, "Near-wall formulation of the Partially-averaged Navier Stokes turbulence model," *AIAA journal*, vol. 49, no. 12, pp. 2627–2636, 2011.

[85] R. Schiestel and A. Dejoan, "Towards a new partially integrated transport model for coarse grid and unsteady turbulent flow simulations," *Theoretical and Computational Fluid Dynamics*, vol. 18, no. 6, pp. 443–468, 2005.

[86] B. Chaouat, "The state of the art of hybrid RANS/LES modeling for the simulation of tur-

bulent flows," *Flow, Turbulence and Combustion*, vol. 99, no. 2, pp. 279–327, 2017.

[87] B. Chaouat and R. Schiestel, "From single-scale turbulence models to multiple-scale and subgrid-scale models by fourier transform," *Theoretical and Computational Fluid Dynamics*, vol. 21, no. 3, pp. 201–229, 2007.

[88] D. C. Wilcox, *Turbulence modeling for CFD*, vol. 2. DCW industries La Canada, CA, 1998.

[89] K. A. Chauhan, H. M. Nagib, and P. A. Monkewitz, "Evidence on non-universality of Karman constant," in *Progress in Turbulence II*, pp. 159–163, Springer, 2007.

[90] H. Jasak, A. Jemcov, and Z. Tukovic, "OpenFOAM: A C++ library for complex physics simulations," in *International workshop on coupled methods in numerical dynamics*, vol. 1000, pp. 1–20, 2007.

[91] J. L. Lumley and G. R. Newman, "The return to isotropy of homogeneous turbulence," *Journal of Fluid Mechanics*, vol. 82, no. 1, pp. 161–178, 1977.

[92] W. H. Press, S. A. Teukolsky, W. T. Vetterling, and B. P. Flannery, "Numerical recipes in C++," *The art of scientific computing*, vol. 2, p. 1002, 1992.

[93] J. Jeong and F. Hussain, "On the identification of a vortex," *Journal of fluid mechanics*, vol. 285, pp. 69–94, 1995.

[94] T. Theodorsen, "The structure of turbulence," in *50 Jahre Grenzschichtforschung*, pp. 55–62, Springer, 1955.

[95] W. Willmarth and S. Lu, "Structure of the Reynolds stress near the wall," *Journal of Fluid Mechanics*, vol. 55, no. 1, pp. 65–92, 1972.

[96] L. Di Mare, M. Klein, W. Jones, and J. Janicka, "Synthetic turbulence inflow conditions for large-eddy simulation," *Physics of Fluids*, vol. 18, no. 2, p. 025107, 2006.

[97] Z.-T. Xie and I. P. Castro, "Efficient generation of inflow conditions for large eddy simulation of street-scale flows," *Flow, turbulence and combustion*, vol. 81, no. 3, pp. 449–470, 2008.

[98] J.-C. Golaz, J. D. Doyle, and S. Wang, "One-way nested large-eddy simulation over the askervein hill," *Journal of Advances in Modeling Earth Systems*, vol. 1, no. 3, 2009.

[99] H. Nakayama, T. Takemi, and H. Nagai, "Large-eddy simulation of urban boundary-layer flows by generating turbulent inflows from mesoscale meteorological simulations," *Atmospheric Science Letters*, vol. 13, no. 3, pp. 180–186, 2012.

[100] T. S. Lund and P. Moin, "Large-eddy simulation of a concave wall boundary layer," *International journal of heat and fluid flow*, vol. 17, no. 3, pp. 290–295, 1996.

[101] D. Spalding, "A single formula for the 'law of the wall'," *Journal of Applied Mechanics*, vol. 28, no. 3, pp. 455–458, 1961.

[102] E. De Villiers, *The potential of large eddy simulation for the modeling of wall bounded flows*. PhD thesis, Imperial College of Science, Technology and Medicine, London (UK), 2006.

[103] I. Orlanski, "A simple boundary condition for unbounded hyperbolic flows," *Journal of computational physics*, vol. 21, no. 3, pp. 251–269, 1976.

[104] L. L. Pauley, P. Moin, and W. C. Reynolds, *A numerical study of unsteady laminar boundary layer separation*. TF-34. Thermosciences Division, Stanford University, 1988.

[105] Y. Li, J.-I. Choi, Y. Choic, and J. Kim, "A simple and efficient outflow boundary condition for the incompressible Navier–Stokes equations," *Engineering Applications of Computational Fluid Mechanics*, vol. 11, no. 1, pp. 69–85, 2017.

[106] S. Rezaeiravesh and M. Liefvendahl, "Effect of grid resolution on large eddy simulation of wall-bounded turbulence," *Physics of Fluids*, vol. 30, no. 5, p. 055106, 2018.

[107] J. C. Hunt, A. A. Wray, and P. Moin, "Eddies, streams, and convergence zones in turbulent flows," in *Proc. 1988 Summer Program Cent. Turbul. Res., pp. 193-207. Stanford, California*, 1988.

[108] W. Saric and A. Thomas, "Experiments on the subharmonic route to turbulence in boundary layers," in *Turbulence and chaotic phenomena in fluids*, pp. 117–122, 1984.

[109] P. S. Klebanoff, K. Tidstrom, and L. Sargent, "The three-dimensional nature of boundary-layer instability," *Journal of Fluid Mechanics*, vol. 12, no. 1, pp. 1–34, 1962.

[110] P. Klebanoff and K. Tidstrom, *Evolution of amplified waves leading to transition in a bound-*

ary layer with zero pressure gradient, vol. 195. National Aeronautics and Space Administration, 1959.

[111] H. Fasel and U. Konzelmann, "Non-parallel stability of a flat-plate boundary layer using the complete navier-stokes equations," *Journal of Fluid Mechanics*, vol. 221, pp. 311–347, 1990.

[112] T. Herbert, "Boundary-layer transition-analysis and prediction revisited," in *29th Aerospace Sciences Meeting*, p. 737, 1991.

[113] F. M. White, *Fluid mechanics*. McGraw-Hill Education, 2015.

[114] Y. S. Kachanov, V. Kozlov, and V. Y. Levchenko, "Nonlinear development of a wave in a boundary layer," *Fluid dynamics*, vol. 12, no. 3, pp. 383–390, 1977.

[115] W. S. Saric and A. H. Nayfeh, "Nonparallel stability of boundary-layer flows," *The Physics of Fluids*, vol. 18, no. 8, pp. 945–950, 1975.